Micro-PIXE for quantitative mapping of metal concentration in O. glaberrima and O. sativa riceplants

Laboratory of Tandetron

Alassane Alassane

Proposal ID

397

Multi-elemental analysis of roots and leaves from Oryza glaberrima rice plants at vegetative stage of growth by combined PIGE, RBS, PIXE and GC-TDS methods

S. Fernandes[a,*], A. Traoré[b], O. Fleury[b], V. Havránek[a], J. Kučera[a], A. Ndao[b]
[a]Nuclear Physics Institute CAS, v.v.i., 250 68, Husinec - Řež, Czech Republic
[b]Institute for Applied Nuclear Technology, Cheikh Anta Diop University, Dakar, Senegal

This study aims at understanding the bioaccumulation and transport mechanisms of both micro- and macronutrients in the leaves and roots of African rice *Oryza glaberrima* Steud (OG) plants cultivated in Senegal during the wet season at the vegetative stage of growth to determine the translocation factors from roots to leaves and to evaluate the suitability of OG rice plants for phytoremediation. A comparative analysis of the elemental composition of roots and leaves of OG plants, provided information on the bioaccumulation of nutrients necessary for plant growth which can become detrimental if their toxicity level is reached. The elemental analysis of basic nutrients (C, H, O), macronutrients (N, P, K, Ca, Mg and S) and micronutrients (Cl, Fe, Cu, Mn, Ni and Zn) in the OG roots and leaves was made possible by several elemental analytical techniques (PIGE, RBS, PIXE and GC-TDS). All methods were validated by analysis of pure substances and certified reference materials. The high accumulation rate of Cu (5 x), Al (4 x) and Fe (~ 2 x) in the OG rice roots relative to the leaves indicates the existence of low translocation factors for these metals from root to leaves probably due to the existence of plant mechanisms to limit their transport and to preferentially accumulate Si (% mass: 5.2 ± 0.5) in the rice leaves. The high accumulation rates of Mn, Ni, Rb and Cr "heavy" metals in the OG leaves relative to the roots, shows that these can be partially removed from soil through phytoextraction processes by harvesting the shoot tissues.

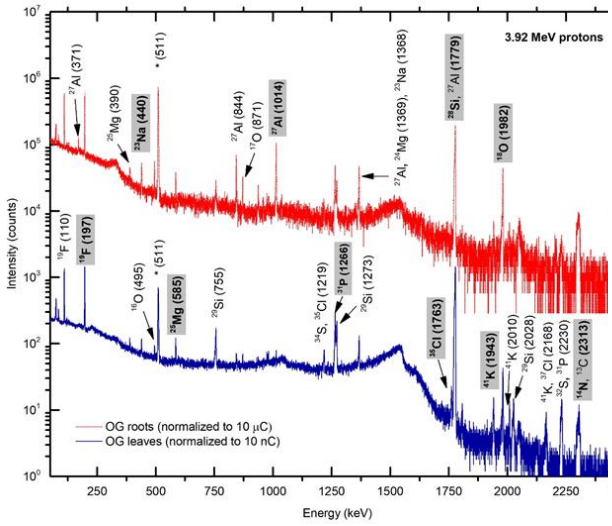

Figure 2 Normalized γ-ray spectrum for OG leaves and roots at 3.92 MeV protons. The γ-energy reference peak used for isotopic quantification is indicated inside grey boxes and highlighted in bold

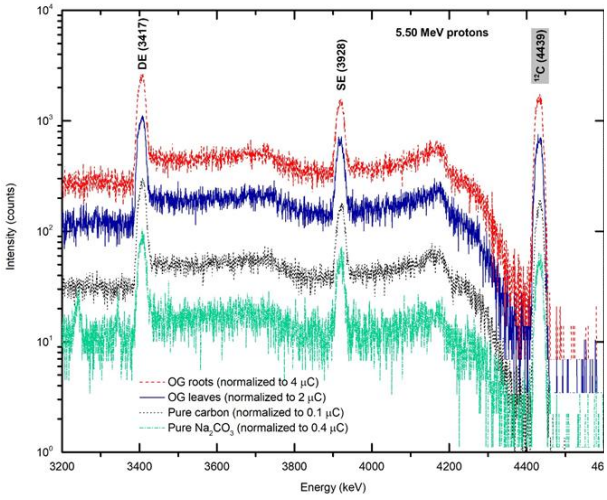

Figure 1 Detail of the normalized γ-ray spectrum of OG leaves and roots, and standard materials C and Na_2CO_3 at 5.5 MeV protons showing the reaction $^{12}C(p,p_1\gamma)^{12}C$ at 4439 keV and its single and double escape peaks.

The determination of the elemental composition of cultivated soil and OG rice stems and grains is necessary to obtain the translocation factors of nutrient and non-nutrient into different plant organs from soil to root and from leaves to grains for characterization of their transport into the plant cells. The analysis of the OG rice grains is needed to testify that all the potential toxic elements identified in this study, and other heavy metals such as As, Sb, Cd, Hg and Pb, known to be absorbed by the plant biomass, were not accumulated to toxic levels for human consumption to ensure food security in West Africa.

[1] S. Bado et al. NIM B 371 (2016) 407 - 412.

USANS investigation of Nitinol stents and massive samples before and after heat treatment

Neutron Physics Laboratory - Neutron diffraction

Massimo Rogante

Proposal ID

403

Final report regarding the CANAM_403 Proposal "Nanoscale investigation by USANS of Nitinol stents and massive samples before and after heat treatment"

M. Rogante, Rogante Engineering Office, Italy

The USANS measurements have been performed on both the Ni-Ti stents and the following massive samples:
A - Nitinol massive, untreated;
B - Nitinol massive, submitted to the treatment T1 (PIRAC Coating - 900°C; 1.5h; WQ). Thickness of the coating: TiN (0.1 microns) + Ti2Ni (0.6 microns);
C - Nitinol massive, submitted to the treatment T2 (PIRAC Coating - 900°C; 3h; WQ). Thickness of the coating: TiN (0.5 microns) + Ti2Ni (0.6 microns).
Parts of these samples have been investigated, with reference to a proper section. Three resolutions (high, medium and low) and a wavelength λ = 2.1Å have been adopted for these measurements. Data have been preliminarily treated, showing a quite low transmission. Some of the obtained scattering curves are shown in Fig. 1, indicating very small differences between the samples.

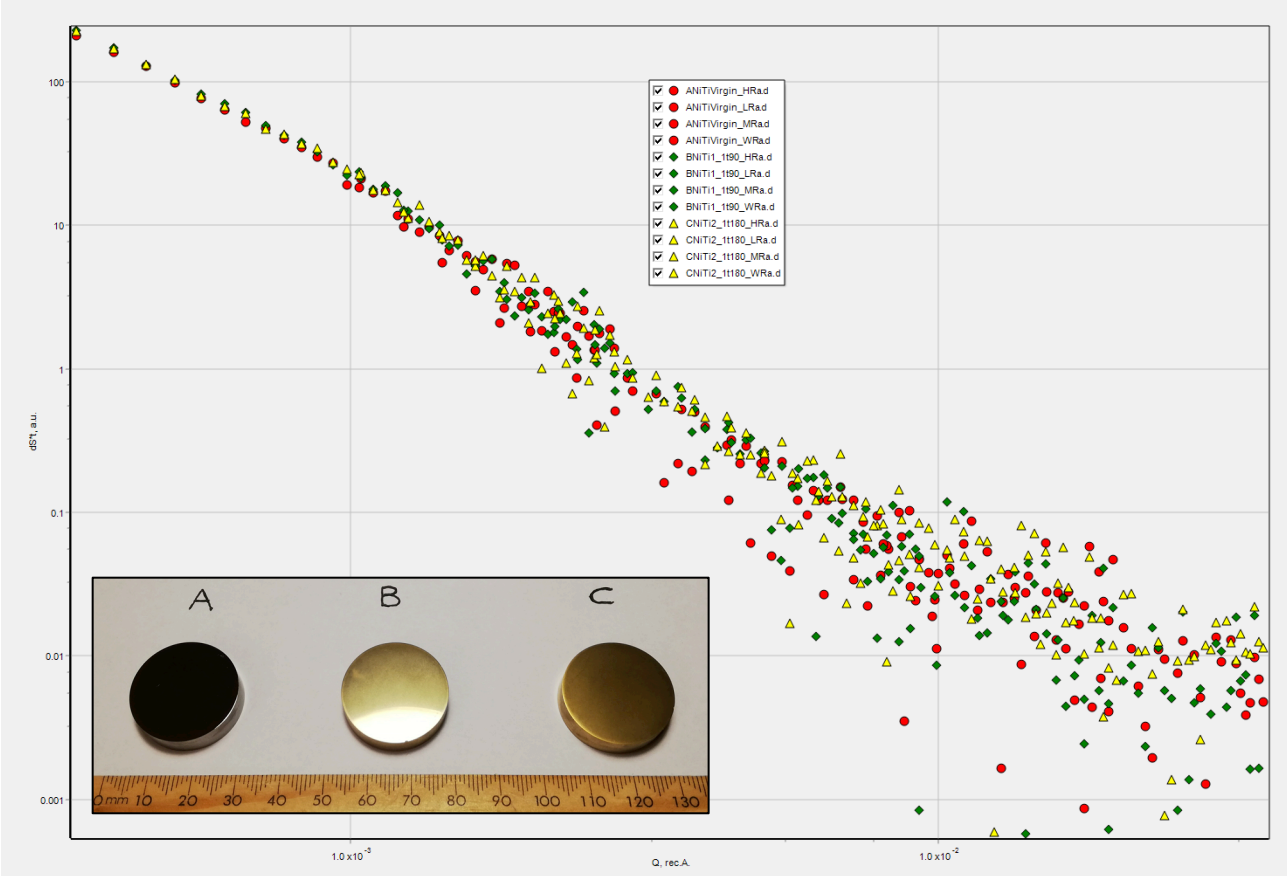

Fig. 1. USANS by NiTi alloy: sample A (red circles); sample B (green rhombus); sample C (yellow triangles).

Concerning the stents, one in particular is scattering, indicating the possible presence some large precipitates. A full data treatment is in progress. The final results, being part of a feasibility study related to the investigation of the considered materials by neutron techniques, will be added to those obtained by SEM/TEM analyses.

Target matrices for high-yield production of selected atomic and molecular ions

Laboratory of Tandetron

Mojmír Nmec

Proposal ID

404

Report regarding proposal: Target matrices for high-yield production of selected atomic and molecular ions

K. Fenclová, M. Bilous, T. Prášek, M. Němec, CTU in Prague – FNSPE, Czech Republic
J. Tecl, M. Klímová, J. Kučera, Nuclear Physics Institute, Řež, Czech Republic

Experiments on Tandetron were focused on fluoride matrices suitable for production of high-yield ion beams and with potential use in accelerator mass spectrometry. After screening of suitable materials, production of aluminium beam and ion forms created in the ion source were of major interest. Analysis was performed using low energy (LE) side of the ion beam line, where LE magnet and adjacent Faraday cup were used as mass spectrometer. Two fundamental materials were used - Na_3AlF_6 for production of fluoride molecular beams and Al_2O_3 as a reference oxide compound. Several crystallographic modifications of these compounds, defined by the way of preparation and subsequent heat treatment, were mixed with various compatible modifiers such as CaF_2, PbF_2, TiO_2, Cu, Ag, W powders in Cu and Ag target holders. In the ion source, two temperatures of Cs reservoir were used during target sputtering – 30 °C for the fluoride samples and 70 °C for the oxides. Selected peaks were additionally analysed using high energy (HE) part of the beam line to resolve possible isobaric interferences.

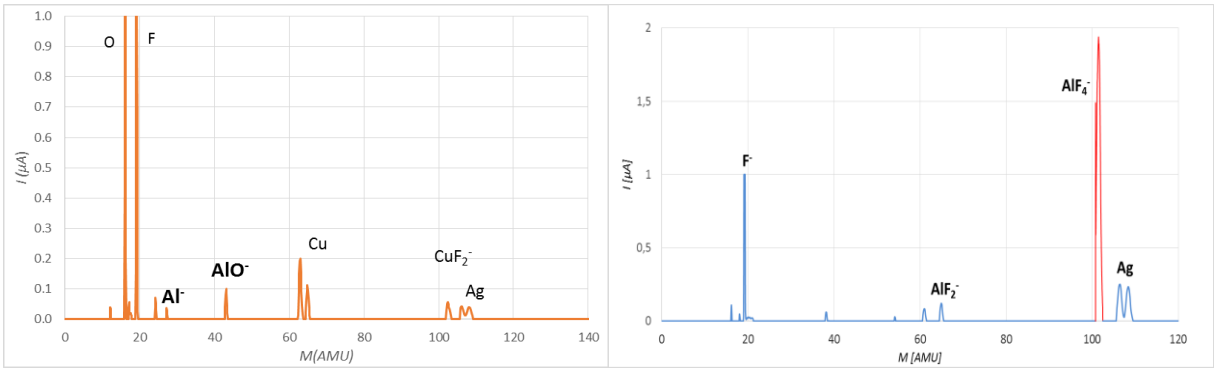

Fig. 1: LE mass spectra of (a) Al_2O_3 mixed with Ag powder in copper target holder at 70 °C of Cs reservoir *(F^- peak is a residuum from previous experiments with fluoride matrices)*, (b) Na_3AlF_6 mixed with PbF_2 in Ag target at 30 °C of Cs reservoir; both at 2 kV target voltage.

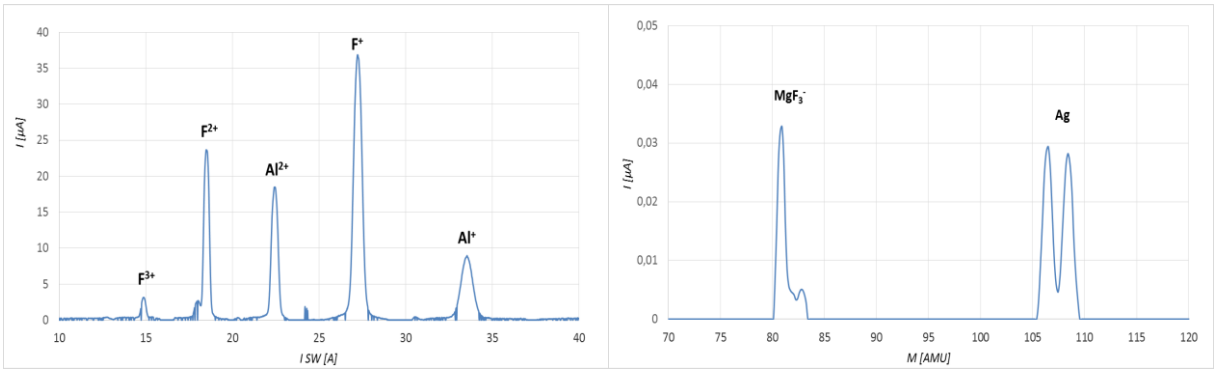

Fig. 2: (a) HE spectrum of Na_3AlF_6 + MgF_2 mixed with PbF_2 and Ag (1:1:1), (b) LE spectrum of MgF_2 in Ag target holder, both at 30°C of Cs reservoir and 2 kV target voltage.

The results show high potential of fluoride matrices for production of aluminium beams – when comparing standard Al^- with newly produced AlF_4^- beams, the latter provides approx. 10 – 40 times higher currents before entering the accelerator. In addition, no isobaric MgF_4^- was detected at both LE and HE side, indicating potential use of $^{26}AlF_4^-$ in AMS analyses and production of high intensity Al ion beam without isobaric contamination. Practically no significant influence of Al_2O_3 preparation procedure on Al^- or AlO^- ion beam intensity was found; in addition $Co(AlO_2)_2$ + Ag (1:2) provided interesting currents of high purity Co^- and Ag^- beams suitable for ion beam applications.

Characterization of Residual Stresses Distribution in Thick Welded Sheets for High-pressure Vessels

Neutron Physics Laboratory - Neutron diffraction

Karel Trojan

Proposal ID

405

Report regarding proposal "Characterization of RS Distribution in Thick Welded Sheets for High-pressure Vessels after LASER Welding"

K. Trojan[1*], Ch. Hervoches[2], A. Vlk[1], J. Čapek[1], N. Ganev[1]

[1]Department of Solid State Engineering, Faculty of Nuclear Sciences and Physical Engineering, Czech Technical University in Prague

[2] Nuclear Physics Institute, ASCR, v.v.i., Department of Neutron Physics, 25068 Řež, Czech Republic

*karel.trojan@fjfi.cvut.cz

It was found from the residual stresses (RSs) determined by neutron diffraction in three different sample orientations and in three different depths under the surface (see Fig. 1), that the greatest gradient of RSs is in the direction parallel to the weld (L – longitudinal direction) for both 8 and 10 mm thick plates. Moreover, the RSs in the longitudinal direction have a tensile character. On the other hand, the character of the RSs in the normal and transversal direction is more or less compressive.

The next step in this research is going to be determination of the RSs, using X-ray diffraction, in the same depths as in the case of the neutron diffraction. Comparison of results of these two methods will be made.

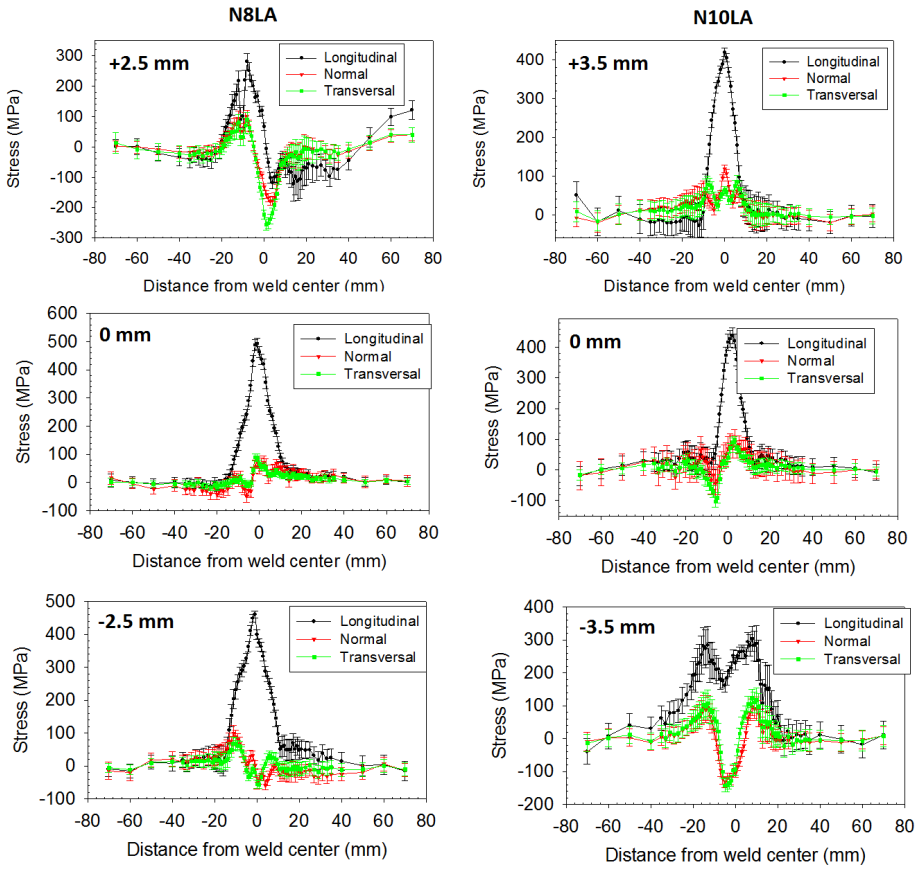

Figure 1: RSs for laser welded samples along three measured lines obtained by neutron diffraction.

Acknowledgement

Measurements were carried out at the CANAM infrastructure of the NPI CAS Řež supported through MEYS project No. LM2015056. This work was supported by the project TH02010664 of the Technology Agency of the Czech Republic and the Grant Agency of the Czech Technical University in Prague, grant No. SGS16/245/OHK4/3T/14.

RBS/ERDA measurements of X-B-C coatings

Laboratory of Tandetron

Petr Vašina

Proposal ID

406

Charakterizace W(TA, Mo)-B-C vrstev metodou RBS

V **Tabulce 1** se nalézají výsledky uvedené v atomárních procentech. V prvním sloupci je nazev zkoumaného vzorku, v ostatních sloupcích jsou koncentrace jednotlivých prvků uvedené v atomárních procentech, v posledním sloupci se nalézá tloušťka v atomech na cm^2.

Sample	Concetration [at.%]							Substrate	Thickness [10^{15}at/cm^2]
	Mo	W	Ta	B	C	O	Ar		
WBC100	-	25	-	19	44	2	10	Si	16900
WBC103	-	24	-	19	45	2	10	Si	14000
WBC106	-	48	-	17	21	2	12	C	19500
WBC107	-	50	-	18	21	2	9	C	21800
WBC108	-	56	-	16	18	2	8	C	17300
WBC109	-	48	-	19	21	2	10	C	24100
WBC116	-	52	-	17	21	2	8	C	21500
WBC117	-	51	-	19	20	2	8	C	21700
WBC118	-	50	-	20	21	2	9	C	22900
WBC119	-	-	-	-	-	-	-	Si	-
WBC120	-	48	-	23	17	2	10	C	47000
WD13	-	49	-	18	22	2	9	C	21500
WD23	-	31	-	34	22	2	11	C	23100
WA2	-	50	-	10	25	3	12	Si	21100
WA8	-	39	-	20	26	3	12	Si	12000
WB5	-	57	-	10	20	3	10	Si	20000
WB15	-	38	-	20	27	3	12	Si	6500
18E	-	-	25	16	31	12	15	C	2150
9cF	-	-	55	12	18	5	10	c	7300
15E(10E)	-	-	38	14	23	12	13	C	2250
13cF	-	-	-	-	-	-	-	C	-
19cF	-	-	56	12	17	5	10	C	6100
15cG	-	-	18	17	40	15	10	C	2480
10cG	-	-	19	13	46	12	9	C	3000
19cG	-	-	21	17	42	14	8	C	2500
10cH	-	-	16	18	42	12	12	C	4480
19cH	-	-	15	21	38	13	13	C	1850
15cH	-	-	17	20	38	13	12	C	3800
Mobc22	50.5	-	-	24	24.5	>1	-		13000
Mobc36	54.5	-	-	25	19.5	>1	-		13400

Tabulka 1: Přehled složení vzorků v atomárních procentech.

Závěr

Metodou RBS byly zjišťovány koncentrace prvků W(TA, Mo), B, C ve vrstvách na různých substátech. Také byla stanovena míra kontaminace prvky Ar a O. Některé vrstvy byly značně poškozené (Tabulka 1 – žlutě) a nebylo možné stanovit složení vrstvy. Část vzorků měla jen slabě poškozenou vrstvu (Tabulka 1 – šedivě) a domníváme se, že složení vrstev je ve zmíněných atomárních procentech.

Cross-section measurements of the 16O(n,tot) reaction in the neutron energy range 20-35 MeV

Laboratory of Cyclotron and Fast Neutron Generators

Mitja Majerle

Proposal ID

279

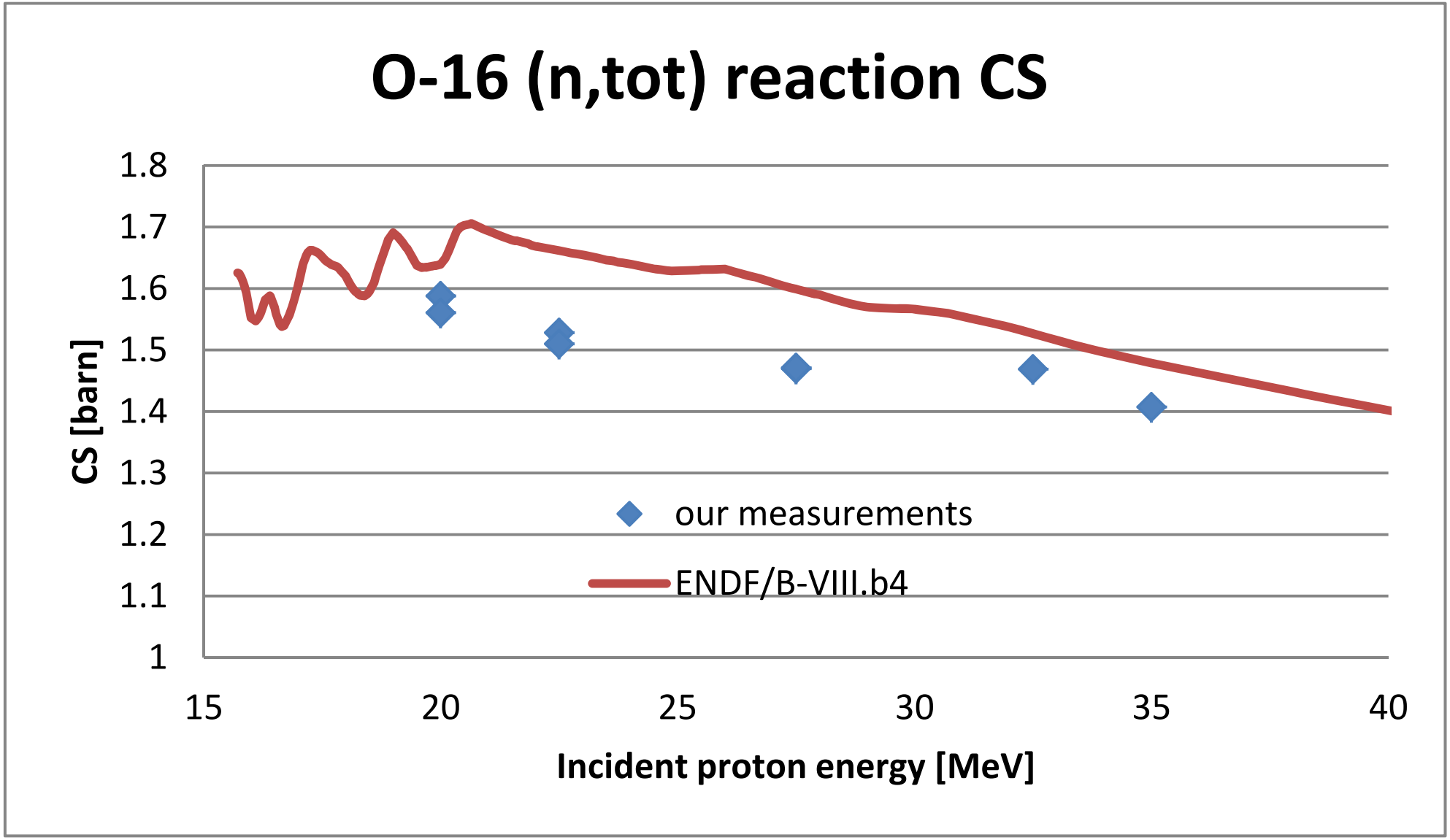
O-16 (n,tot) reaction CS
CS [barn]
1.8
1.7
1.6
1.5
1.4
1.3
1.2
1.1
1
15
20
25
30
35
40
Incident proton energy [MeV]
our measurements
ENDF/B-VIII.b4

Bright fluorescent nanodiamonds with controlled shape

Laboratory of Cyclotron and Fast Neutron Generators

Petr Cígler

Proposal ID

152

Report regarding project "Bright fluorescent nanodiamonds with controlled shape"

Proposer: Petr Cígler, Institute of Organic Chemistry and Biochemistry of the CAS
Registered co-proposer: Jan Štursa, Institute of Nuclear Physics of the CAS

In this project we focused on shaping of nanodiamond (ND) particles to become pseudospherical and on generation of fluorescence defects in these NDs. First, the NDs were chemically processed to round their crystalline interface. We used molten potassium nitrate which caused a controllable etching of crystal edges and vertexes. Using this material, we performed the irradiation experiments in cyclotron to generate vacancies according to the planed scheme, including control particles without etched surface. The resulting irradiated NDs were annealed to generate fluorescent NV centers. In this way we successfully produced both pseudospheric and angular fluorescent NDs. We evaluated their spectral properties and characterized them with various physico-chemical methods (such as zeta potential measurements, dynamic light scattering, transmission electron microscopy, Raman spectroscopy). Using the prepared fluorescent NDs we have performed 7 studies [1-7] which all have been published in high impact journals. We also wrote one chapter for *Methods in Pharmacology and Toxicology* series. Another manuscript has been recently submitted.

References dedicated to the project:

1) Petrakova V., Rehor I., Stursa J., Ledvina M., Nesladek M., Cigler P.: Charge-sensitive fluorescent nanosensors created from nanodiamonds. *Nanoscale*, **2015**, *7*, 12307-12311.
2) Slegerova J., Hajek M., Rehor I., Sedlak F., Stursa J., Hruby M. and Cigler P. Designing the nanobiointerface of fluorescent nanodiamonds: highly selective targeting of glioma cancer cells. *Nanoscale*, **2015**, *7*, 415-420.
3) Havlik J., Raabova H., Gulka M., Petrakova V., Krecmarova M., Masek V., Lousa P., Stursa J., Boyen H.-G., Nesladek M., Cigler P.: Benchtop Fluorination of Fluorescent Nanodiamonds on a Preparative Scale: Toward Unusually Hydrophilic Bright Particles. *Adv. Funct Mater.*, **2016**, *26*, 4134–4142.
4) Stursa J., Havlik J., Petrakova V., Gulka M., Ralis J., Zach V., Pulec Z., Stepan V., Zargaleh S. A., Ledvina M., Nesladek M., Treussart F., Cigler P.: Mass production of fluorescent nanodiamonds with a narrow emission intensity distribution. *Carbon*, **2016**, *96*, 812-818.
5) Petrakova V., Benson V., Buncek M., Fiserova A., Ledvina M., Stursa J., Cigler P. and Nesladek M.: Imaging of transfection and intracellular release of intact, non-labeled DNA using fluorescent nanodiamonds. *Nanoscale*, **2016**, *8*, 12002–12012.
6) Vavra J., Rehor I., Rendler T., Jani M., Bednar J., Baksh M. M., Zappe A., Wrachtrup J., Cigler P.: Supported lipid bilayers on fluorescent nanodiamonds: a structurally defined and versatile coating for bioapplications. *Adv. Funct. Mater.* **2018**, 1803406.
7) Havlik J., Petrakova V., Kucka J., Raabova H., Panek D., Stepan V., Zlamalova Cilova Z., Reineck P., Stursa J., Kucera J., Hruby M., Cigler P.: Extremely rapid isotropic irradiation of nanoparticles with ions generated in situ by a nuclear reaction. *Nature Comm.* **2018**, DOI: 10.1038/s41467-018-06789-8.

Book Chapter:
Neburkova J., Hajek M., Rehor I., Schimer J., Sedlak F., Stursa J., Hruby M., and Cigler P.: Targeting Glioma Cancer Cells with Fluorescent Nanodiamonds via Integrin Receptors. In *Methods in Pharmacology and Toxicology*, E. Patsenker (ed.). pp. 169-189, Humana Press, New York, NY 2018.

Elemental Composition of High Entropy Alloy Sample

Neutron Physics Laboratory - Nuclear analytical methods with neutrons

Kateina Dragounová

Proposal ID

282

Report on instrumental neutron activation analysis of HEA sample

A flat piece of a High Entropy Alloy (HEA) of approximately rectangular shape (3 x 8 mm, ~ 1 mm thick) was available for analysis. It was broken in a clamp with its jaws covered with phenol formaldehyde resin bonded paper (FR–2 material) to avoid contamination into six pieces with masses in the range of 45 – 137 mg. To make sure that no contamination occurred, the broken pieces were shortly boiled in 0.1 M HNO3 prepared from sub-boiled HNO3 diluted with deionized water, so that about 0.5 % of the original sample mass was dissolved. The cleaned samples were washed with ethylalkohol and air dried. The samples were heat sealed into pre-cleaned polyethylene (PE) disk shaped capsules made by sealing PE foils of 0.2 mm thickness with 25 mm and 20 mm diameter for irradiation with thermal and epithermal neutrons, respectively. For quality control purposes, 75 – 100 mg aliquots of NIST standard reference material (SRM) 1633b Constituent Elements in Coal Fly Ash were prepared for irradiation as the HEA samples.

Three modes of INAA based on irradiation in the experimental reactor LVR-15 of the Research Centre Řež were used with minor modifications. Short-time irradiation for 30 s with the whole reactor neutron spectrum (S-INAA) was carried out in an irradiation channel located at the outskirts of the active core behind a beryllium reflector, in which fluence rates of thermal, epithermal and fast neutrons were 3.2×1013, 1.1×1013, and 1.1×1013 cm-2 s-1, respectively. Short-time irradiation for 45 s with epithermal and fast neutrons (S-ENAA) was carried out in the same channel. Thermal neutrons were shielded off by placing the samples into a disk shaped Cd box with 1-mm thick walls. Both short-time irradiation modes were carried out using a pneumatic facility with transport time of 3.5 s. The samples, MES calibrators, blank PE capsules and quality control samples were irradiated individually together with neutron flux monitors (5-mg disks of 0.1% Au–Al foil, IRMM, Belgium, Nuclear reference material IRMM-530a, 0.1mm thickness) to check the neutron fluence rate stability in time. Long-time irradiation for 2 h with the whole reactor neutron spectrum (L-INAA) was performed in a channel located in the Be reflector, in which fluence rates of thermal, epithermal and fast neutrons were 3.6×1013, 8.4×1012, and 8.6×1012 cm-2 s-1, respectively. In this case, the samples, MES calibrators, blank PE capsules and quality control samples were stacked together to form a column that was inserted into an aluminium irradiation can. Iron monitors (50-mg disks) were inserted between each set of 5 samples and/or calibrators to determine the axial neutron flux gradient. The sample masses for S-INAA and S-ENAA were in the range of 45 – 88 mg, those for L-INAA spanned from 116 mg to 137 mg. Gamma-ray spectrometry measurements were performed using two coaxial HPGe detectors. Both HPGe detectors were interfaced to a Canberra Genie 2000 computer controlled gamma-spectrometry analyzer through a chain of associated linear electronics, which included a Canberra 599 Loss Free Counting module to correct the variable count-rate and dead time. Canberra Genie 2000 software was used for evaluation of gamma-ray spectra.

A proxy analysis using X-ray fluorescence analysis was also carried out to assay Pb, which cannot be determined by INAA. The analysis performed at two 0.25x0.25 mm spots yielded Pb concentrations of 1.075% and 1.200 %. The results obtained may be biased ± 20 % rel., because no matrix matched calibration material was available.

Conclusion

The INAA measurement provided the required elemental composition of the tested HEA sample. Concentration of Pb amounting ca 1.1 %wt. was determined from the X-ray fluorescence analysis. The obtained INAA results were presented, together with other characterizations of the sample, at the 18th International Conference on Texture of Materials (ICOTOM-18) in St. George, Utah, USA, and the related paper submitted to IOP Journal of Physics C.

Functional organic-inorganic nanostructures

Laboratory of Tandetron

Vladimir Cech

Proposal ID

410

Report on the project "Functional organic-inorganic nanostructures"

V. Cech, Inst. Mater. Chem., Brno Univ. Technol., Brno, Czech Republic
A. Romanenko, A. Mackova, Nucl. Physics Inst., Rez, Czech Republic

Hydrogenated amorphous carbon-silicon (a-CSi:H) films and hydrogenated amorphous carbon-silicon oxide (a-CSiO:H) films were deposited from pure tetravinylsilane (TVS) precursor or TVS mixed with argon or oxygen gases on silicon wafers or glassy carbons using plasma-enhance chemical vapor deposition (PECVD) in pulsed regime. The tough a-CSi:H films with lower hydrogen concentration (~ 24 at.%) and higher density (~ 2.0 g cm^{-3}) were deposited from TVS/Ar mixture at higher powers (> 25 W), see Fig. 1.

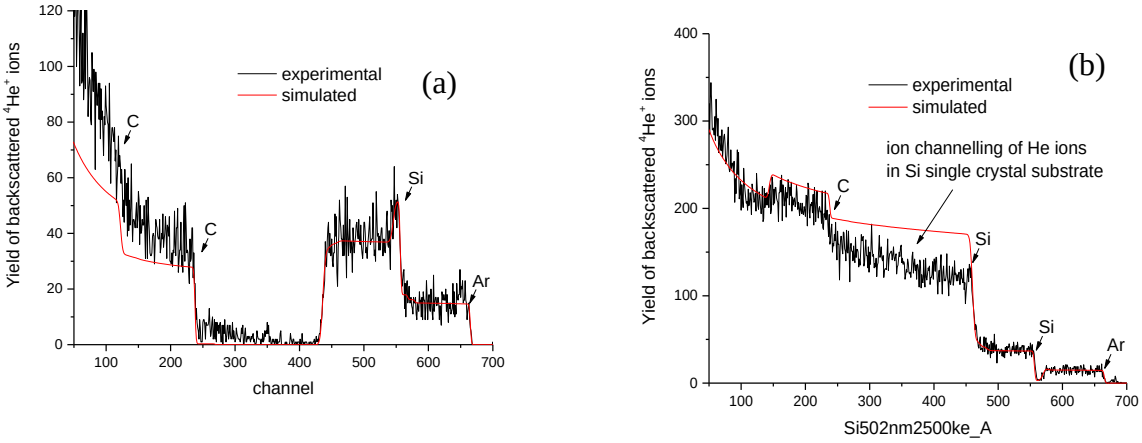

Fig. 1. RBS spectra of tough a-CSi:H films on (a) glassy carbon and (b) silicon wafer.

The RBS/ERDA analysis of polymer-like a-CSi:H films prepared from pure TVS allowed to show a higher hydrogen concentration (~ 58 at.%) and a lower density (~ 1.4 g cm^{-3}) of the material. While, a-CSiO:H films deposited from TVS/O_2 mixture were low hydrogenated materials (~ 7 at.%) with a density of 2.2 g cm^{-3}. The combination of the tough a-CSi:H material with the inorganic a-SiO:H material resulted in a bilayer structure, which was successfully analyzed (Fig. 2), and this type of organic-inorganic structures will continue to be developed and analyzed.

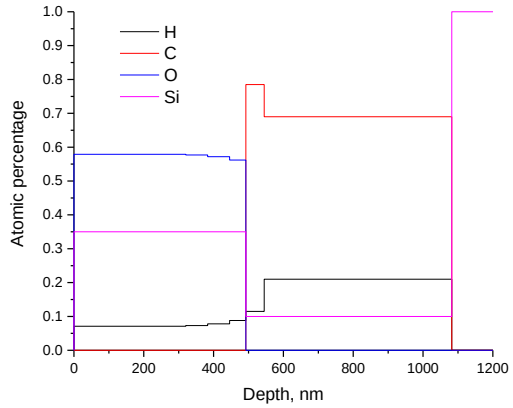

Fig. 2. Depth profile of element composition across the bilayer on silicon wafer.

Trace element fingerprints and chemical discrimination of neolithic stone industry source rocks

Neutron Physics Laboratory - Nuclear analytical methods with neutrons

Kristýna Trnová

Proposal ID

415

Report regarding proposal "Trace element fingerprints and chemical discrimination of neolithic stone industry source rocks"

K. Trnová, L. Veverka, P. Gadas, A. Přichystal, Masaryk University Brno, V. Strunga, Nucl. Physics Inst., Rez, Czech Republic

Partially or fully fabricated tools found in Holasky neolithic settlement with proven source in Želešice amphibolite body in Brno metabasite zone and Isera Mountains have been collected as well as other proven and potential source rocks have been collected. Powdered specimens of each have been prepared, irradiated and analyzed by INAA method.

Geochemical faetures have been studied using elemental ratio plots. The NAA results were also used for corrections and calibrations in XRF studies.

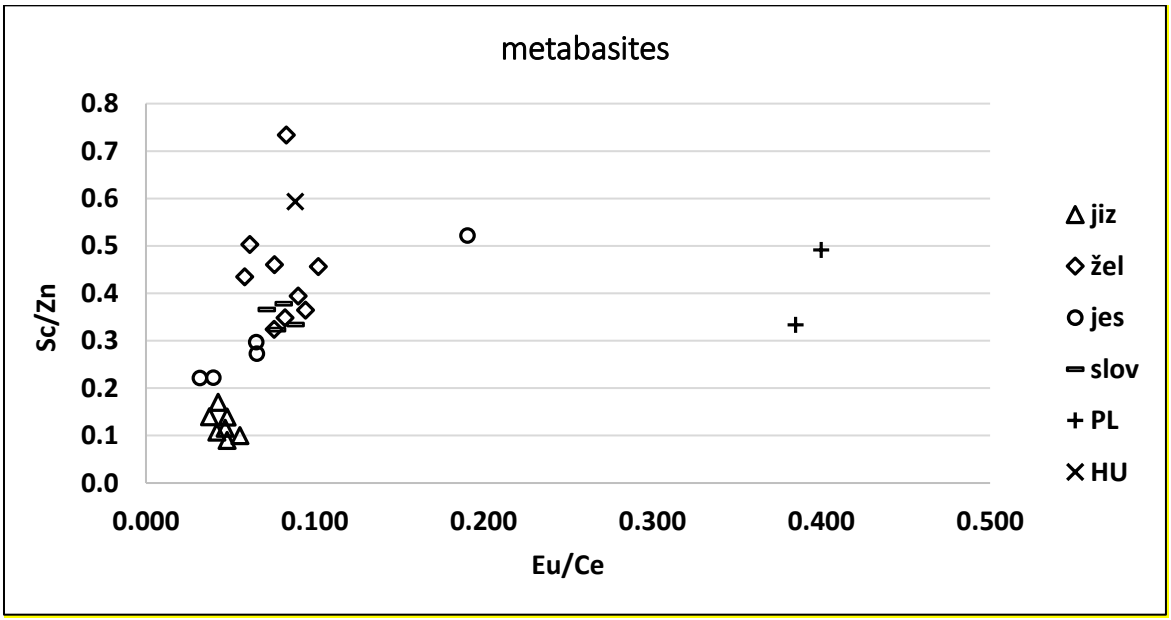

Fig. 1 An example of elemental ratios plot used for discrimination.

Statistical processing of data is performed for further advance in the study and scientific paper on the neutron activation analysis as a tool for discrimination studies of neolithic metabasite industry is in progress.
The results and improved XRF measurements are being used for two doctoral students participating as proposers of the project.

Early results have been presented at the seminar Radioanalytical Methods IAA 2019 on Juny 25th 2019, Faculty of Nuclear Sciences and Physical Engineering, Prague.

Reference

Robert J. Speakman, Nicole C. Little , Darrell Creel, Myles R. Miller , Javier G. Iñañez (2011) Sourcing ceramics with portable XRF spectrometers? A comparison with INAA using Mimbres pottery from the American Southwest. Journal of Archaeological Science, 38, 3483-3496.

197(m)Hg production via the 197Au(d,2n)197Hg reaction

Laboratory of Cyclotron and Fast Neutron Generators

Martin Walther

Proposal ID

293

Report regarding proposal "$^{197(m)}$Hg production via the ^{197}Au(d,2n) reaction"

M. Walther, Helmholtz-Zentrum Dresden-Rossendorf, Institute of Radiopharmaceutical Cancer Research, Germany

O. Lebeda, Nuclear Physics Institute of the CAS, Řež, Czech Republic

The significant larger cross-sections reported for ^{197}Au(d,2n)$^{197(m)}$Hg reaction [1] compared to the proton induced ^{197}Au(p,n)$^{197(m)}$Hg reaction could be unambiguously confirmed. With a deuteron beam energy of 16 MeV more than four times higher yields of the metastable no-carrier-added ^{197m}Hg radionuclide were accessible using comparable beam intensity. Thus it is shown clearly that the limiting factor of the low yield proton based reaction can be overcome using this alternative nuclear reaction. The additional advantage of the higher ratio of the preferable short-lived ^{197m}Hg radionuclide (ratio ^{197m}Hg/^{197}Hg: ~1.7/1) compared to the proton accessible product (~1/1) [2] also increases the attractiveness of this production route for potential theranostic application.

TABLE 1. Hg and Au isotopes after proton or deuteron irradiation of gold in the target solution and product solution after separation using LN resin

	E particle	t_{irr}	I_T	m_{Au}	A_{EOB} [MBq] in target solution				A_{EOB} [MBq] in product				yield
No		[min]	[µA]	[mg]	^{197}Hg	^{197m}Hg	^{196}Au	^{198}Au	^{197}Hg	^{197m}Hg	^{196}Au	^{198}Au	
1	10 MeV p	120	25	185	81	89	0.004	0.099	75	83	<0.001	<0.001	93%
2	12 MeV p	145	20	186	145	160	0.021	0.184	136	150	<0.001	0.002	94%
3	16 MeV d	120	11	186	272	462	7	156	248	420	<0.003	<0.003	91%
4	16 MeV d	150	10	186	332	574	9	193	315	545	<0.006	<0.003	95%

Beside the higher product yield during deuteron irradiation, also the significant formation of gold isotopes as undesired side products must be considered in the workup procedure. Therefore, according to the high requirements, a new resin based Hg/Au separation method was developed. So called LN resin (LaNthanides)[3,4], was successfully tested for this application. The obtained promising results in radionuclide production together with results of labeling - and biological experiments will be published as soon as possible in the current year in peer-reviewed international journals.

References

[1] F. Tárkányi, F. Ditrói, A. Hermanne, S. Takács, B. Király, H. Yamazaki, M. Baba, A. Mohammadi, A.V. Ignatyuk, Nucl. Instrum. Methods Phys. Res., Sect. B 269, pp. 1389–1400, 2011.

[2] M. Walther, S. Preusche, S. Bartel, G. Wunderlich, R. Freudenberg, J. Steinbach, H.-J. Pietzsch: Appl. Radiat. Isot. 97, pp. 177–181, 2015

[3] E. P. Horwitz, C. A. Bloomquist, Journal of Inorganic Nuclear Chemistry, 37, pp. 425–434 1975.

[4] D. McAlister, E. P. Horwitz, Solvent Extraction and Ion Exchange, 25, (6), pp. 757–769 2007.

Investigation of irradiation induced defects in new materials for nuclear reactors: Zr, Ti based al

Laboratory of Tandetron

Jakub Cizek

Proposal ID

423

Investigation of irradiation induced defects in new materials for nuclear reactors: Zr, Ti based al – Final report

Several alloys consisting of refractory metal elements Hf, Nb, Ta, Ti, Zr have been prepared by arc melt casting. The chemical composition and basic properties of samples studied are summarized in Table 1. The alloys were irradiated with 2.9 MeV protons at room temperature using a Tandetron accelerator. Annealing was performed in several steps with fluence gradually increasing from 10^{15} to 10^{16} cm^{-2}. The samples were investigated after each irradiation step in order to study the development of irradiation-induced defects with increasing fluence.

Table 1 *List of refractory metal alloys studied in the present work. The table shows the composition of each alloy; atom misfit parameter (δ) representing a measure of the magnitude of lattice distortions; configurational entropy of random solid solution (S^{SS}); results of tensile test with constant strain rate of 2×10^{-4} s^{-1}: yield strength (YS), ultimate tensile strength (UTS) and elongation-to-failure (A_{max}); Vickers hardness (HV) measured using load of 0.5 kg applied for 10 s; and the average cross-section for absorption of epithermal neutrons (σ).*

composition	δ (%)	S^{SS} (R)	YS (MPa)	UTS (MPa)	A_{max} (%)	HV (GPa)	σ (barn)
NbTaTi	1.05	1.10	620	683	18.5	2.42 ± 0.02	9.3
NbTaTiZr	4.83	1.39	1144	1205	6.4	3.64 ± 0.02	7.0
$Nb_{0.5}TaTiZr_{1.5}$	5.22	1.32	-	843	0	4.80 ±0.03	6.9
HfNbTaTiZr	4.98	1.61	1155	1212	12.3	3.48 ± 0.03	23.3

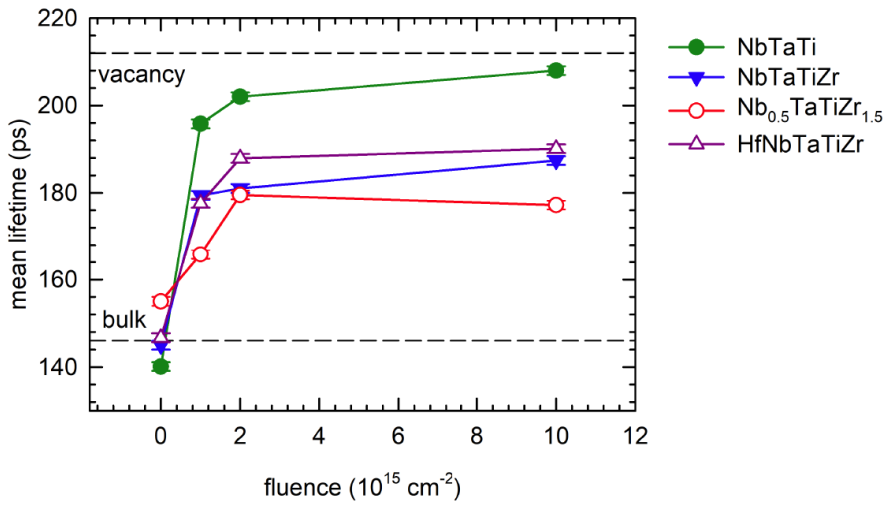

Figure 1 *The development of the mean positron lifetime of NbTaTi, NbTaTiZr, Nb0.5TaTiZr1.5 and HfNbTaTiZr alloy with the irradiation fluence.*

Fig. 1 shows the development of the mean positron lifetime with increasing irradiation fluence. The mean positron lifetime is a robust parameter which is only slightly affected by correlations between the fitting parameters. It is useful for observation of trends occurring during irradiation. The virgin samples exhibit single component LT spectra indicating that positrons are annihilated in single state. Virgin state of the alloys studied is characterized by the lifetime in the range 140-155 ps corresponding to the bulk lifetime, i.e. the lifetime of free positrons not trapped at defects. Hence, the concentration of defects in these alloys is very low and virtually all positrons are annihilated in the free state. Proton irradiation led to an increase of the mean positron lifetime due to formation of radiation-induced defects. The mean lifetime of all alloys increases with increasing fluence indicating that the concentration of irradiation-induced defects increases with increasing fluence. The most pronounced increase of the mean positron lifetime was observed for the NbTaTi alloy. For the highest fluence of 10^{16} cm^{-2} the mean lifetime approaches 210 ps corresponding to lifetime of positrons trapped in monovacancy testifying that majority of positrons is trapped in vacancies. The NbTaTiZr and HfNbTaTiZr alloys exhibit comparable increase of the mean positron lifetime but it is remarkably lower than that for the NbTaTi alloy. The lowest increase of the mean positron lifetime was observed in the $Nb_{0.5}TaTiZr_{1.5}$ alloy where the magnitude of lattice distortions is the highest among the alloys studied as reflected by the highest value of the misfit parameter δ, see Table 1.

Hence, the present investigations of refractory metal alloys irradiated by protons confirmed good radiation resistance of HEAs. It seems that good resistance against radiation damage is common property of 3d transition metal and refractory metal HEAs. Radiation resistance of HEAs is directly related to the effect of lattice distortions representing a typical feature of HEA structure.

Study of the fission process at higher neutron energies

Laboratory of Cyclotron and Fast Neutron Generators

David Hladík

Proposal ID

424

Final report regarding the proposal 'Study of the fission process at higher neutron energies'

Small samples of an ^{238}U were irradiated with quasi-monoenergetic neutrons from the cyclotron U-120M with p+^{7}Li and p+Be converter at several peak neutron energies in the range of 17-33 MeV and delayed neutrons (DN) were measured. BF_3 detectors were chosen for the measurement of time distribution of the DN.

New measurement process was developed and tested during several experiments. The goal was to minimize the effect of saturation of the detectors as well as measure even the shortest decay group below 0.5 s after the end of irradiation. This goal was successfully accomplished.

This result was presented at "Second French-Czech « Barrande » Nuclear Research Workshop" in France.

These results can serve as a proof of concept and the work will continue to acquire better precision. Subsequently, the simulation using General Fission Model (GEF) is in progress for further comparison of acquired data

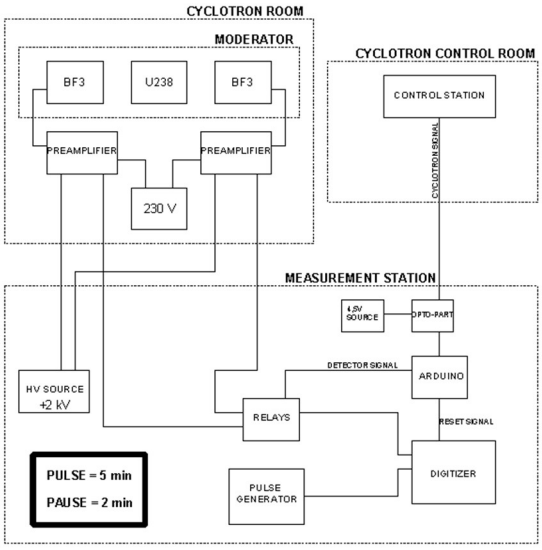

Figure 1. Block scheme of the measurement setting and process

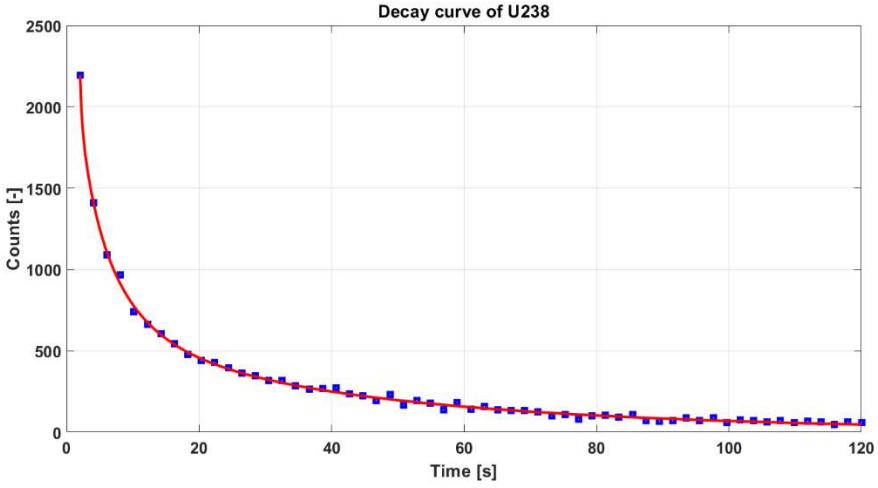

Figure 2. Decay curve obtained from an experiment using p+Be target, En=20 Mev, distance 1 m.

Systematic study on the strain free / independent lattice parameter D0 for multiphase materials subj

Neutron Physics Laboratory - Neutron diffraction

Samuel Pulvermacher

Proposal ID

425

Systematic study on the strain free / independent lattice parameter D_0 for multiphase materials

Samuel Pulvermacher (email: samuel.pulvermacher@kit.edu, Karlsruhe Institute of Technology)
Jan Šaroun (email: saroun@ujf.cas.cz, Ústav jaderné fyziky AV ČR, v. v. i.)
Jens Gibmeier (email: jens.gibmeier@kit.edu, Karlsruhe Institute of Technology)

Introduction:

Aim of the project is to develop a basic understanding on the effect of local phase-specific micro residual stresses on the determination of the strain independent lattice parameter D_0 and providing a basis for the reliable modelling of the surface effects for coarse multiphase materials and for materials states with chemical gradients in the near surface region. Corporately, a measuring and evaluation strategy for non-destructive analysis of near surface residual stress gradients for problematic material states will be developed. In the current research project fundamental investigations on the effect of phase-specific micro residual stresses on the reference value D_0 will be carried out. For this purpose, defined residual stress states will be applied for multiphase materials with variations in the phase contents. In the first approach various fine grained duplex steels will be studied, which clearly differ in the amount of the phase contents. Finally, based on the experimental results and the accompanying numerical simulations, recommendations for appropriate sample preparations for providing appropriate reference samples for multiphase materials will be provided.

Measurement setup:

In this first approach we focused on the investigation of duplex steel type X2CrNiMoN22-5-3 (1.4462) and X3CrNiMoN27-5-2 (1.4460), which hold a phase composition of about 50% ferrite and 50% austenite and 70/30 (for 1.4460) in the as received state.

In preparation of the beamtime defined uniaxial tensile tests were performed, so that total strains between 0 and 9% were realized. From this test series, small pins were sectioned using wire-cut EDM (electro discharge machining) for the loading states with 0, 2 and 9%. The sectioned pins had diameters of 2, 3, 4 and 5 mm to check if the remaining residual stress state is affected by the sample size. The respective orientation of the pin relative to the sample was noted in order to be able to take into account the loading axis and the potential texture influences. Each pin was measured in two directions, i.e. in axial and in radial = transverse direction.

Preliminary results

In both materials, 4 ferrite (α) and 5 austenite (γ) lattice planes were investigated. Peakshift due to sample misorientation were corrected using the program SIMRES. Figures 1 show an example of the phasespecific interplanar spacings for the duplex steel 1.4460 in longitudinal direction. The data allow for the comparison of lattice strain determined in specific sample orientations for pins of the same and varying sizes. The data indicate that the interplanar spacings are affected by micro-residual stresses that result from the uniaxial elasto-plastic deformation. However, rather large data scattering exist, which not least stem for the pin misorientation, which could only be corrected insufficiently. It is planned to re-measure the pins in a modified experimental setup to reduce misorientation effects and increase the stability of the results.
For this purpose, a new sample holder was designed and manufactured at KIT. In parallel, the Meredit experiment was rebuilt, i.e. the sample carousel was replaced by a linearly movable table to improve the sample alignment.

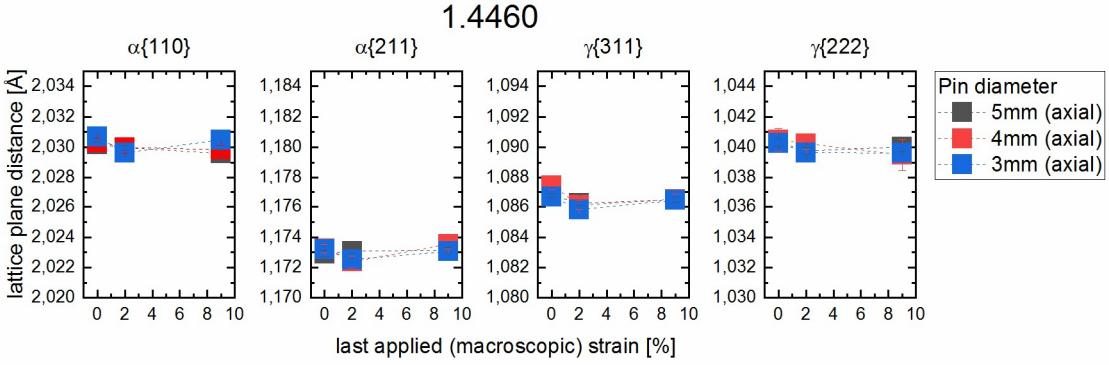

Figure 1: Examplary plot of the change of the phase-specific lattice plane distance with the degree of plastic deformation for the investigated duplex steel 1.4460

Interface properties of exchange-bias UO2-Fe3O4 nanostructures

Laboratory of Tandetron

Ladislav Havela

Proposal ID

170

Report: Crystal structure of the CaF_2-Based UO_2/Fe_3O_4 thin films

Exchange interaction through interface between a ferromagnet and an antiferromagnet may result in the magnetic exchange bias (EB) effect [1]. This property has become of a great technological value for applications in magnetic sensors based on spin-valves or tunnel junctions [2]. In this work, we studied crystal structure in bilayers of antiferromagnetic UO_2 (bulk Néel temperature 30.8 K) with ferrimagnetic Fe_3O_4, which are known to produce large exchange bias effect [3].

The samples were prepared by reactive sputter deposition from metallic targets on CaF_2 (100) substrates. A set of the samples with different Fe_3O_4 thicknesses (60-300 Å) were produced while the thickness of the UO_2 layer in the samples was kept constant (~300 Å). UO_2 was deposited at 850 K, using a partial oxygen pressure of 1.2×10^{-6} mbar (Ar pressure of 6×10^{-3} mbar). Fe_3O_4 was deposited on the top of UO_2 at the same partial oxygen pressure but at room temperature, in order to avoid interdiffusion. In-situ control of stoichiometry of each deposited layer was carried out using XPS (see inset in Fig. 1 for the XPS spectrum of Fe-2p in magnetite). A Mg cap was deposited for protection on top of each sample. Due to the matching lattice parameters of UO_2 and CaF_2 the films grew epitaxially in the [100] direction. The structures were further characterized by means of the Rutherford Backscattering Spectroscopy (RBS), which showed no intermixing at the interface (within the depth resolution 1 nm). Very pronounced ion channeling characteristics proved high crystallinity (low defect concentration) of the UO_2 layer, which is actually better than that of the (100) CaF_2 substrate. The spectra obtained showed well-separated signals from UO_2 and magnetite (Fig. 1). A channeling was observed also for the Fe_3O_4 layer, but considerably more defects/disorder was found, which could be perhaps related to a combined twinning [3] effect and monoclinic distortion below Verwey transition (120 K), as the samples had been subjected to thermal cycling during the prior magnetic study.

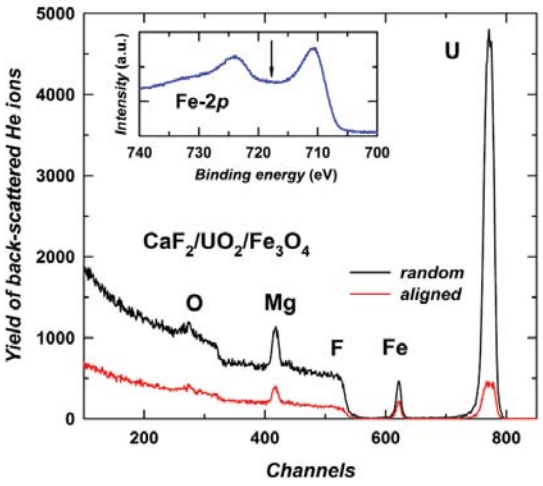

Yield of back-scattered He ions for the incident beam along the [100] crystallographic direction of the UO_2 crystal (aligned) and at a random orientation (random) for the UO_2/Fe_3O_4 sample deposited on a CaF_2 substrate and capped with Mg. Inset: Fe-2*p* XPS spectrum of magnetite. Arrow indicates a position of a Fe^{3+} satellite line (absent) characteristic of γ-Fe_2O_3.

The samples were prepared in the framework of the EARL project of the European Commission Joint Research Centre, ITU Karlsruhe. RBS measurements were carried out at the CANAM infrastructure of the NPI ASCR Rez supported through MŠMT project No. LM2011019.

1) W. H. Meiklejohn and C. P. Bean, "New magnetic anisotropy", Phys. Rev. B, 102 1413, (1956). 2) B. Dieny et al, Phys. Rev. B, 43 1297 (1991). 3) E. A. Tereshina et al, Appl. Phys. Lett., 105 122405 (2014).

Mesostructure of biocompatible interpenetrating composites on the base of bacterial cellulose

Neutron Physics Laboratory - Neutron diffraction

Iurii Chetverikov

Proposal ID

298

Report for proposal №298

Mesostructure of biocompatible interpenetrating composites on the base of bacterial cellulose

This proposal is aimed for the structural characterization of new interpenetrating polymeric networks (IPN) made on the base of nanogel films of bacterial cellulose (BC) and polyvinyltriazole (PVT) with/without Cu(II). The critical feature of composites based on BC is the presence of the structural peculiarities on different scale levels. Such peculiarities existed in human biological tissues, such as cartilages or muscle fibers and could be used for artificial producing of these materials. Ultra-small-angle neutron scattering (USANS) method can reveal the micron-scale structure of both BC and IPN on its base, that being no done before. It is essential not only for the fundamental analysis but also for the fabrication of functionalizing organic-inorganic composites on the base of BC with desired mechanical properties. The proposal is also aimed to study both the distribution of Cu(II) and the mesoscopic level of IPN. For this reason, the USANS approach will appropriate because this technique is not harmful to samples, give the possibilities to reveal structures in micro- and mesoscopic scale levels using the contrast variation by D_2O/H_2O or by varying the concentration of Cu(II) dopant. As opposed to the direct measurement techniques such as SEM or AFM, USANS gives a total picture of scattering on the contrasting inhomogeneities in broad range scale, which is primarily crucial for fractal objects with complex hierarchical structure.

The USANS measurements were carried out on the double-bent-crystal SANS diffractometer MAUD in a momentum transferred Q-range of $2\cdot10^{-4} \div 2\cdot10^{-2}$ Å^{-1} at Q-resolution $10^{-4} \div 10^{-3}$ Å^{-1}. It was investigated a series of 16 samples of IPN based on BC including PVT and Cu(II). Each sample will be measured in two positions: perpendicular or parallel to a growth surface of BC. Figure 1 shows the typical USANS dependences for composite hydrogels containing Cu(II) (scattering W4) and without copper (scattering W3).

The obtained data are under consideration. The profound analysis will allow estimating the fractal dimensions, ranges of self-similarity, sizes of aggregates, clusters, and particles forming them and will give the new information about the IPN formation processes.

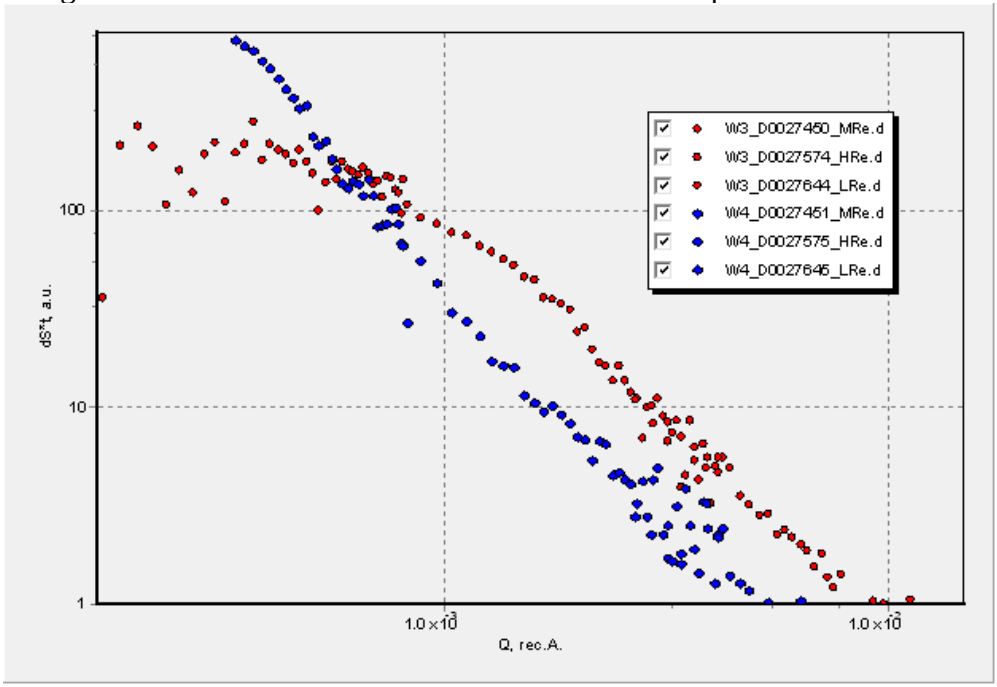

Figure 1. USANS for composite hydrogels containing 6 mass% of Cu(II) (scattering set W4—full blue symbols) and without copper (scattering set W3—full red symbols).

Calibration of TimePix detectors and low-energy proton radiography

Laboratory of Tandetron

Václav Olšanský

Proposal ID

426

Report regarding proposal "Calibration of TimePix detector and low-energy proton radiography"

V. Olšanský[1], C. Oancea[2], C. Granja[2], V. Havránek[1], A. Mackova[1], J. Jakůbek[2], Š. Polanský[2], P. Krist[1]

[1] *Nuclear Physics Institute Czech Acad. Sci., Řež, Czech Republic*

[2] *ADVACAM, Prague, Czech Republic*

The goal of these measurements was to perform proton radiography in the air and to characterize the proton and carbon micro-beams in vacuum. Several experimental setups were designed. Firstly, AdvaPix–TimePix3 and MiniPix–TimePix detectors with 300 µm thick Si sensors were calibrated in proton µ-beams and in a wide-area scanning beam. Afterwards, Al and Mylar targets (of various thicknesses from 5 to 30 µm) and more complex target stairs-like (thicknesses of 30, 25, 10, 5 and 0-air) of Al and Mylar, Fig. 1, were used to produce proton radiographies. All targets were placed close to the sensitive Si layer of detector, see Fig.1.

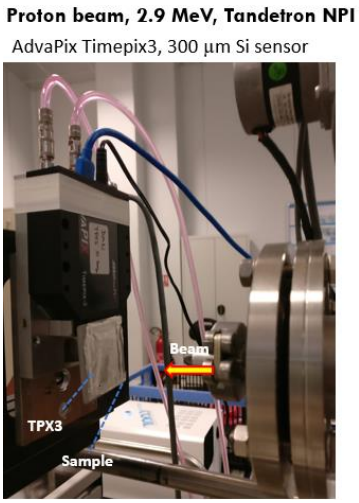

Figure 1 Experimental setup of a proton radiography using Advapix Timepi-3 detector.

The highly integrated signal electronics per-pixel provide fast and dark-current free single particle detection. The hybrid semiconductor pixel detector Timepix-3, Fig. 1, provides high-sensitivity and wide-dynamic range in terms of particle types, fluxes and spectral response. Timepix-3 detector visualizes the track of each individual particle and determines its time of interaction, spatial location and energy loss, see Fig. 2.

This experiment demonstrates the possibility of using low energy protons for radiography of very thin samples. Results have been visualized as images which show one of these distributions: cluster sizes, cluster energy and high. The reconstruction of proton radiography of Al stairs-like target can be seen in Fig. 3. Promising results were obtained based on the cluster area, Fig.3 b), and cluster energy, Fig. 3c). Further investigations of other targets are ongoing.

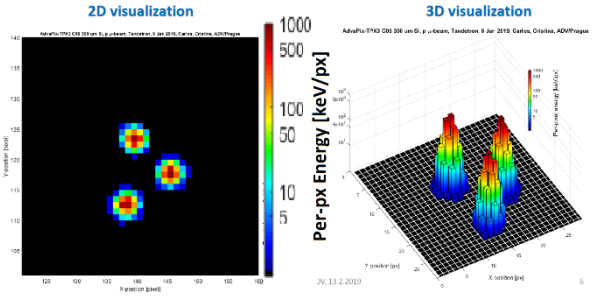

Figure 2 Position- and spectral-sensitive detection of single protons. a) 2D visualization and b) 3D visualization of per-pixel energy (displayed in color scale) of 3 events delivered in spot scanning beam mode [1].

<u>Vacuum measurements using ^{12}C scanning beams</u>

A Minipix Timepix detector was placed inside the vacuum chamber and the Time and spatial distribution of 10 MeV ^{12}C beam were studied. In Fig. 4 is sown the Time and spatial pattern of a scanning beam measured for 1 min. Other energies and scanning patterns were studied.

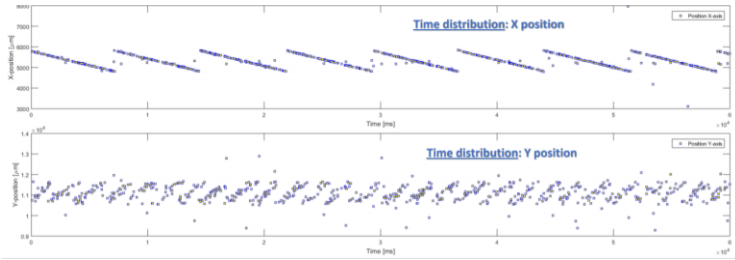

Figure 4 Time and spatial distribution of 10 MeV ^{12}C-ion beams.

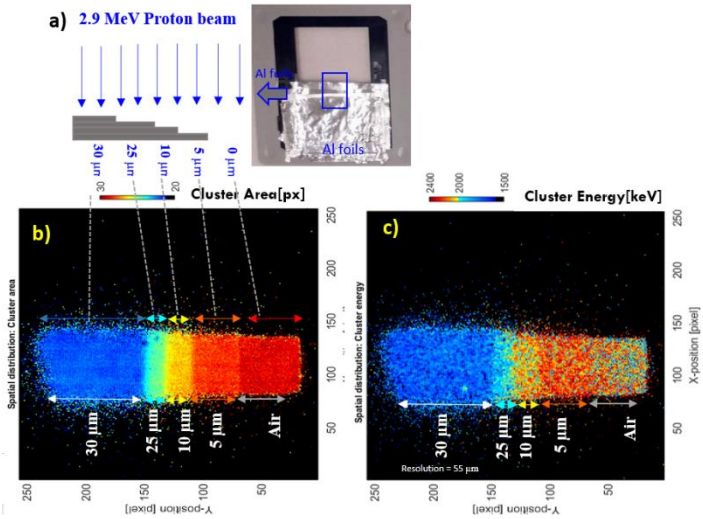

Figure 3 a) Al stair- like target, b) radiography reconstruction of the Al target using cluster area and c) reconstruction using the cluster energy.

Reference: C. Oancea, C. Granja, J. Jakubek, A. Mackova, V. Havranek, V. Olsansky *Charged particle imaging with Timepix a Timepix3 Pixel Detector*, 5th Annual LLU Workshop, USA 2019

In-situ V-SANS studies of WC grain growth in hard metals

Neutron Physics Laboratory - Neutron diffraction

Ahmet Bahadir Yildiz

Proposal ID

427

Experimental report

Proposal: In-situ V-SANS studies of WC grain growth in hard metals (ID: 427)

Ahmet Bahadir Yildiz, Peter Hedström: KTH Royal Institute of Technology, Stockholm

Beamline scientist: Vasyl Ryukhtin

The performance of a cemented carbide relies on the as-sintered composite microstructure consisting of the hard WC grains embedded in the ductile Co matrix. In order to tailor the properties of a cemented carbide, the understanding of the microstructure evolution concerning WC growth during the sintering has great importance. During our beamtime on the MAUD, we performed the first in-situ small angle scattering studies of cemented carbides. We studied WC grain growth as a function of the different type and amount of grain growth inhibitors, i.e. V and Ti, during the sintering at 1400 °C for 2 h using the high-temperature furnace. In order to eliminate the evaporation of Co, the furnace was filled by Ar. Due to the limited time, VSANS data were acquired only at high-resolution mode with 12 min intervals. However, this instrumental resolution was not sufficient to cover the desired Q-range to detect fine-grained WC especially at the beginning of the sintering.

Fig. 1 shows the VSANS curves of 0.15 wt.% Ti-doped sample. At the beginning of the sintering, VSANS curve consisted only of Porod-type scattering. On the other hand, due to the growth of WC, we observed a Guinier regime at the lower-Q region of VSANS curve after 2 h of sintering. Therefore, we would like to continue in-situ experiments with medium- and low-resolution modes to cover the entire size-range of WC grains. Furthermore, an oxide layer formation was observed on the sample surfaces (**Fig. 2**). We avoided such formation by trapping free O_2 inside the furnace using sacrificial Ti piece that, however, resulted in Co-layer formation (**Fig. 3**). We are currently working on possible solutions to avoid layer formation during the sintering.

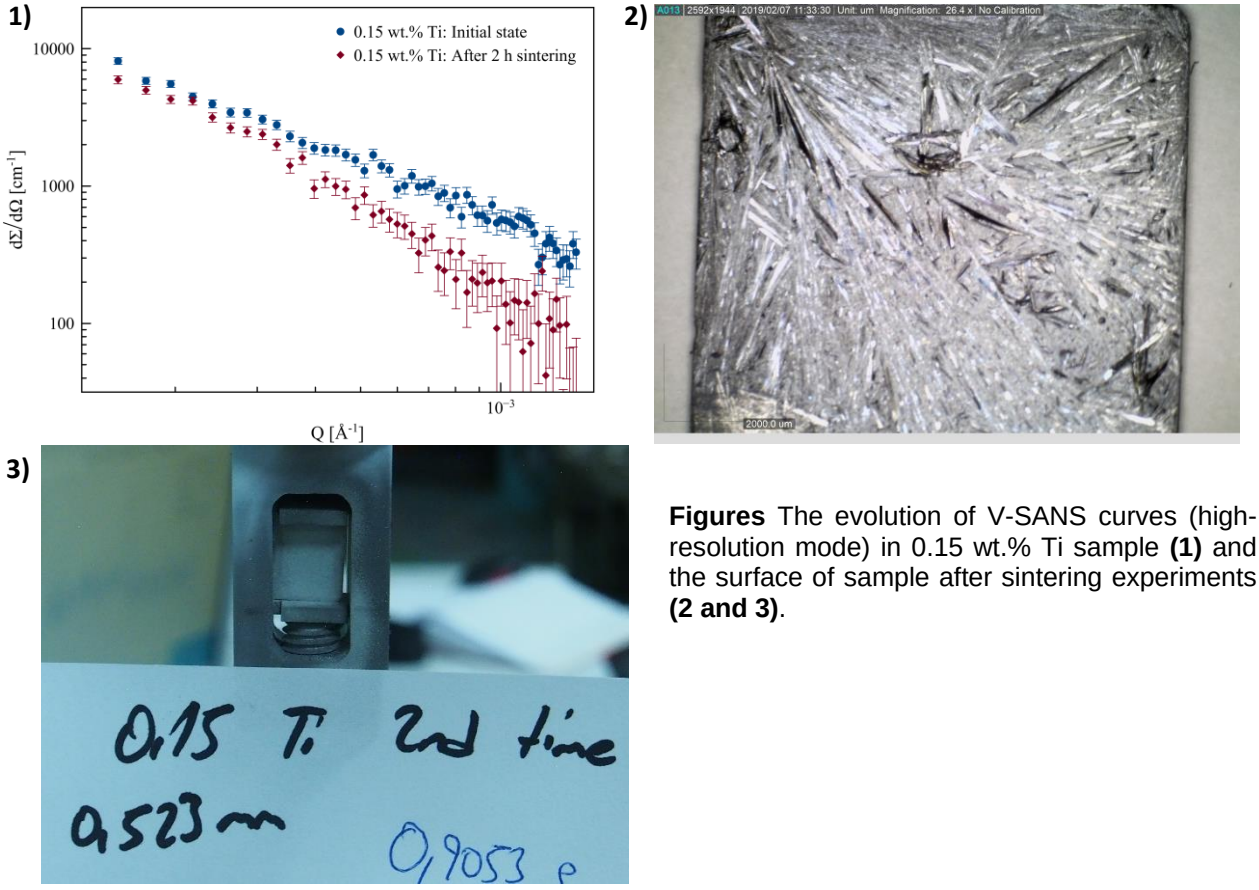

Figures The evolution of V-SANS curves (high-resolution mode) in 0.15 wt.% Ti sample **(1)** and the surface of sample after sintering experiments **(2 and 3)**.

Multielemental analysis of nutrients and pollutants in cultivated O. glaberrima and Sativa rices on

Neutron Physics Laboratory - Nuclear analytical methods with neutrons

Alassane Alassane

Proposal ID

428

Multi-elemental analysis of roots and leaves from Oryza glaberrima rice plants at vegetative stage of growth by combined PIGE, RBS, PIXE and GC-TDS methods

S. Fernandes[a,*], A. Traoré[b], O. Fleury[b], V. Havránek[a], J. Kučera[a], A. Ndao[b]
[a]Nuclear Physics Institute CAS, v.v.i., 250 68, Husinec - Řež, Czech Republic
[b]Institute for Applied Nuclear Technology, Cheikh Anta Diop University, Dakar, Senegal

This study aims at understanding the bioaccumulation and transport mechanisms of both micro- and macronutrients in the leaves and roots of African rice *Oryza glaberrima* Steud (OG) plants cultivated in Senegal during the wet season at the vegetative stage of growth to determine the translocation factors from roots to leaves and to evaluate the suitability of OG rice plants for phytoremediation. A comparative analysis of the elemental composition of roots and leaves of OG plants, provided information on the bioaccumulation of nutrients necessary for plant growth which can become detrimental if their toxicity level is reached. The elemental analysis of basic nutrients (C, H, O), macronutrients (N, P, K, Ca, Mg and S) and micronutrients (Cl, Fe, Cu, Mn, Ni and Zn) in the OG roots and leaves was made possible by several elemental analytical techniques (PIGE, RBS, PIXE and GC-TDS). All methods were validated by analysis of pure substances and certified reference materials. The high accumulation rate of Cu (5 x), Al (4 x) and Fe (~ 2 x) in the OG rice roots relative to the leaves indicates the existence of low translocation factors for these metals from root to leaves probably due to the existence of plant mechanisms to limit their transport and to preferentially accumulate Si (% mass: 5.2 ± 0.5) in the rice leaves. The high accumulation rates of Mn, Ni, Rb and Cr "heavy" metals in the OG leaves relative to the roots, shows that these can be partially removed from soil through phytoextraction processes by harvesting the shoot tissues.

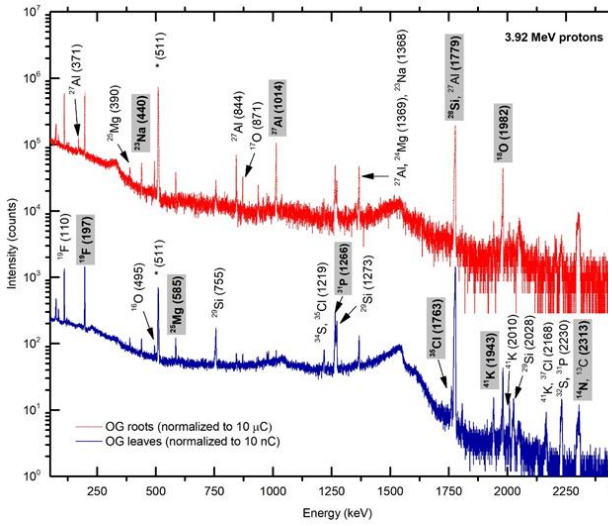

Figure 2 Normalized γ-ray spectrum for OG leaves and roots at 3.92 MeV protons. The γ-energy reference peak used for isotopic quantification is indicated inside grey boxes and highlighted in bold

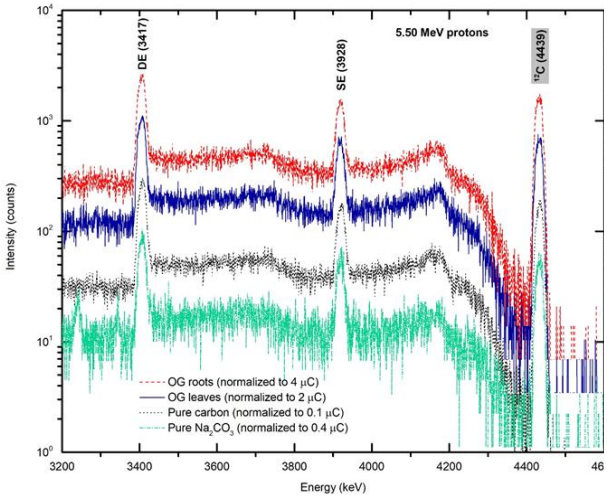

Figure 1 Detail of the normalized γ-ray spectrum of OG leaves and roots, and standard materials C and Na_2CO_3 at 5.5 MeV protons showing the reaction $^{12}C(p,p_1\gamma)^{12}C$ at 4439 keV and its single and double escape peaks.

The determination of the elemental composition of cultivated soil and OG rice stems and grains is necessary to obtain the translocation factors of nutrient and non-nutrient into different plant organs from soil to root and from leaves to grains for characterization of their transport into the plant cells. The analysis of the OG rice grains is needed to testify that all the potential toxic elements identified in this study, and other heavy metals such as As, Sb, Cd, Hg and Pb, known to be absorbed by the plant biomass, were not accumulated to toxic levels for human consumption to ensure food security in West Africa.

[1] S. Bado et al. NIM B 371 (2016) 407 - 412.

A structural study and ion irradiation of the silicon crystal layer

Laboratory of Tandetron

Romana Mikšová

Proposal ID

306

Report regarding proposal "A structural study and ion irradiation of the silicon crystal layer"

R. Mikšová, A. Macková, A. Jagerová, P. Malinský, Nucl. Physics Inst., Rez, Czech Republic
P. Slepička, V. Švorčík, Inst. Chem. Tech., Prague, Czech Republic

Our results from irradiation of Si-crystal layer on SiO_2/Si using 0.4 MeV Kr^+, Ag^+, Au^+ and 5.0 MeV Ag^{2+}, Au^{2+} at ion fluences of 0.5×10^{15}–5.0×10^{15} cm^{-2} show that the nuclear-energy loss is dominant for all ion species used in our experiment at the energy of 0.4 MeV and the highest is for Au^+ ions. This is clearly proved by RBS-C, where the completely disordered structure in the implanted layer is observed even at the lowest ion-implantation fluence used. The nuclear stopping leads to atomic displacement and the production of vacancies or large-scale defects and the subsequent amorphisation of the implanted layer as was observed in RBS-C measurement, where Si layers were completely amorphised under 0.4 MeV ion implantation performed at the ion fluence of $0.5\times10^{15}cm^{-2}$ (see Figure 1a). Since amorphisation occurs near the end of range damage. For 0.4 MeV ions the end is near Si/SiO_2 interface. It is shown in ref. [1] that the critical fluence for amorphisation is lower than 1.0×10^{14} cm^{-2} (at the room temperature), therefore lower as in our experiment.

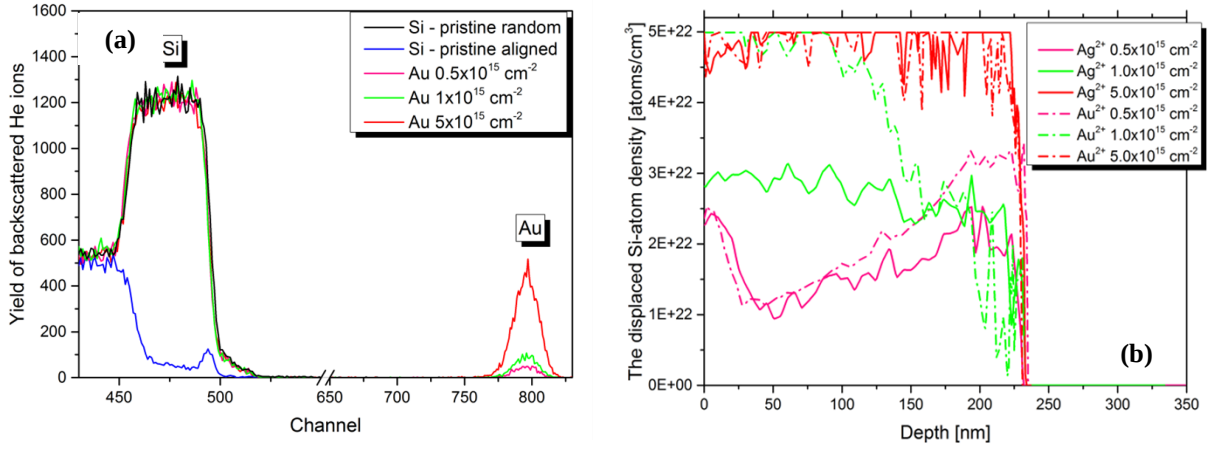

Figure 1. The RBS-C of random and aligned spectra of SOI irradiated by 0.4 MeV (a) and 5.0 MeV (b) Au^+ at ion fluencies of 0.5×10^{15}–5.0×10^{15} cm^{-2} compared to the aligned spectrum of the virgin SOI sample. The depth profile of the displaced Si-atom density in the Si layer implanted by 5.0 MeV Ag^+ and Au^+ ions at ion fluences of 0.5×10^{15}–5.0×10^{15} cm^{-2} (b).

In the case of the implantation of 5.0 MeV ions, the SRIM [2] code predicted more vacancies produced by Au^+ ions than by Ag^+ ions, which is in agreement with RBS-C results, exhibiting more progressive enhancement of Si-atom displacement density with increasing ion fluence for Au^+ ions (see Figure 1b). In the case of 5.0 MeV Ag^+ and Au^+ ions, the ratios S_e/S_n were 3.23 and 1.44 and the projected range of ions is behind SiO_2/Si interface, in the Si bulk respectively. All these effects were also observed in RBS-C for the ion fluences above 1×10^{15} cm^{-2}. For the lowest ion fluence used, the dynamic annealing is decreasing number of vacancies, which is not included in SRIM simulation as well as the surface damage accumulation is not predicted by SRIM. It can be concluded that 5.0-MeV ions modify the structure causing the changing of axial channels during He^+ ion channelling. RBS-C identified the relative number of disordered Si atoms, which was successfully used for the angular-scan simulation in FLUX code [3] for various ion-irradiation fluencies.

AFM found out that 5.0 MeV-ion implantation caused mainly surface smoothening and the average roughness is a descending function of the ion-implantation fluence. This effect can be connected to the progressive surface modification confirmed by RBS analysis, where the silicon-structure degradation may be reflected in smoothening caused by the predominant diffusion mechanism induced by ion implantation. The FTIR analysis confirmed Si crystalline layer modification mainly done by Si-Si bond rupture or modification depending on the prevailing nuclear or electronic stopping, respectively.

The results have been send for publication in Applied Surface Science and Surface Interface Analysis.

[1] L. Pelaz, L.A. Marqués, J. Barbolla, Appl. Phys. Rev. **96** (2004) 5947–5977.

[2] J. F. Ziegler et al., *SRIM: The stopping and range of ions in matter*, Version SRIM-2013. Available at: http://www.srim.org/.

[3] P.J.M. Smulders, D.O. Boerma, Nucl. Instrum. Methods Phys. Res. B 29 (1987) 471–489.

Radiation Hardness of Si Pixel Chips and Components for ALICE Inner Tracker System Upgrade Project

Laboratory of Cyclotron and Fast Neutron Generators

Filip Krizek

Proposal ID

313

Report regarding the proposal: Radiation Hardness of Silicon Pixel Chips and Components for the ALICE Inner Tracking System Upgrade Project

Filip Křížek, Nuclear Physics Institute of CAS

The ALPIDE chips are monolithic active pixel sensors which are going to be used in the upgraded Inner Tracking System (ITS) detector of the ALICE experiment at CERN. In 2017, we continued with the tests of their radiation hardness and we studied the chip performance as a function of the accumulated total ionization dose (TID) and reverse substrate bias. The corresponding measurements were carried out on 19.1., 1.3., 2.3., 10.4., 3.5., 4.5., 15.6., 24.7., 28.8., 18.9., 11.10., and 6.11. Figure 1 shows an example of the obtained dependence of the chip sensitivity threshold as a function of the accumulated TID. At present the sensor accumulated a TID of 1.6 Mrad and is still fully operational. The chips irradiated at Rez were then further characterized at the test beams at the CERN PS. Results from this activity were published in the diploma thesis of Artem Isakov [1] and were presented on regular meetings of the ITS upgrade characterization group (10.5., 4.10., 25.10.). In the test performed on 14.6., we irradiated chips on the inner barrel stave and found that they follow the expected behavior. Further tests of radiation hardness were performed also with a field programmable gate array (FPGA) and the corresponding firmware design which are going to be used in the ITS readout unit (RU). On 22.–24.5. and 19.–20.6. we irradiated a RU prototype based on the Xilinx Kintex-7 325T FPGA. The goal of the test was to investigate various soft error mitigation firmware designs. Results from this activity were presented by Krysztof Sielkiewicz at the NSREC-2017 conference [2]. The final version of the RU based on Xilinx XCKU060 FPGA was tested during 4.–6.12. These measurements provide an important data for the Production Readiness Review of the ITS RU project which will take place in spring 2018.

References

[1] A. Isakov, *Investigation of silicon pixel sensors for the ALICE Inner Tracking System upgrade project*, diploma thesis, Tomsk Polytechnic University, 2017.

[2] K. Sielkiewicz et al., *Experimental Methods and Results for the Evaluation of Triple Modulator Redundancy SEU Mitigation Techniques with the Kintex-7 FPGA*, IEEE NSREC-2017 conference.

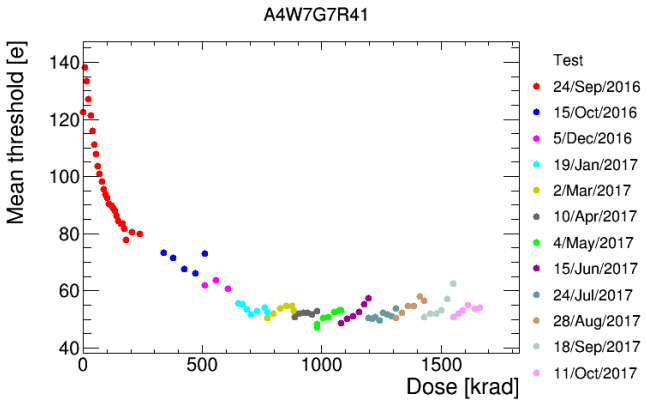

Figure 1: ALPIDE sensor sensitivity threshold as a function of the accumulated total ionization dose. The threshold is measured in electron charges. The sensor was irradiated with a beam of 30 MeV protons. The legend quotes the dates of irradiation campaigns.

Ion modification of GaN crystalline structures

Laboratory of Tandetron

Romana Mikšová

Proposal ID

317

Report regarding proposal "Ion modification of GaN crystalline structures."

A. Macková, A. Jagerová, P. Malinský, Nuclear Physics Institute of the Czech Academy of Sciences, v. v. i., Rez, Czech Republic
Z. Sofer, D. Sedmidubský, K. Klímová, Department of Inorganic Chemistry, Institute of Chemical Technology, Prague, Czech Republic
R. Böttger, S. Akhmadaliev, Institute of Ion Beam Physics and Materials Research, Helmholtz Zentrum Dresden-Rossendorf, Dresden, Germany

In our results, we have carried out a study of a GaN epitaxial layer (of c-plane and a-plane) implanted with Gd, Kr and Au ions at energy of 400 keV and and 5 MeV Au ions using implantation fluences ranging from 5×10^{14} cm^{-2} to 5×10^{15} cm^{-2}. The damage accumulation in the buried layer is much more pronounced in c-plane (0001) GaN than in a-plane (11–20) GaN for both ion species used. More pronounced differences in damage accumulation between a-plane and c-plane GaN are observed in the fluence range 0.5×10^{14}–1×10^{15} cm^{-2} for Gd implanted GaN and 1×10^{15}–5×10^{15} cm^{-2} in the Kr implanted GaN.

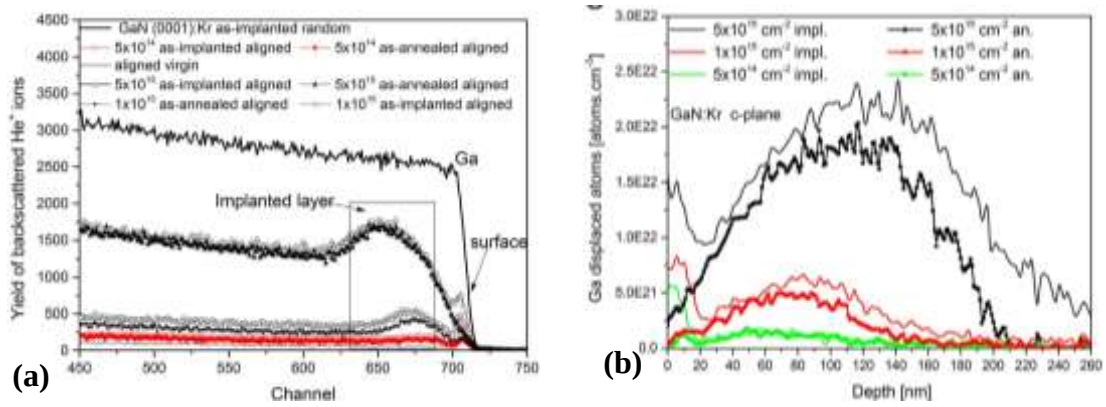

Figure 1. The RBS-channelling aligned spectra for as-implanted and as-annealed samples implanted with Kr ion in c-plane GaN (a) . The density–depth profile of displacement Ga atoms in GaN as-implanted with Kr ions: as-implanted and as-annealed c-plane GaN b).

Lower surface disorder is evident in Kr-implanted GaN than in Gd-implanted GaN for the same implantation fluence. Annealing has caused a progressive decline in the disorder preferably in the surface layer and also in the bulk implanted the latter one mainly for c-plane GaN for both ion species.

Gallium nitride implanted with 400-keV Au ions shows the bimodal depth profiles at a fluence of 5×10^{15} cm^{-2} in as-implanted samples. More damage accumulation was observed in the buried layer in the case of c-plane GaN than in a-plane for 400-keV ion implantation energy, in case the nuclear stopping prevails (Figure 2). In case of 5-MeV Au ions modified surface GaN, where electronic stopping prevails the surface damage is significantly lower comparing to 400-keV Au implantation and the long range defect.

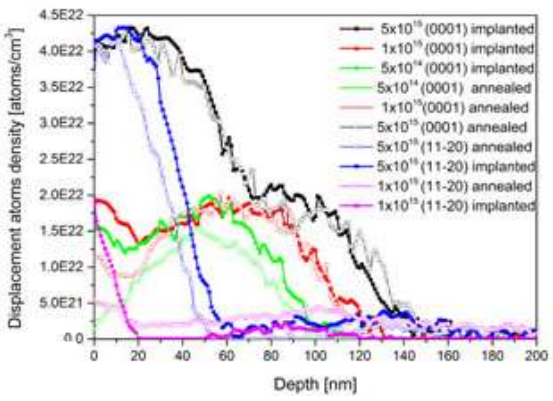

Figure 2. The density-depth profile of displacement atoms in gallium nitride as-implanted with Au at ion-implantation energy of 400 keV in as-implanted and as-annealed c-plane and a-plane GaN.

The results were published in Surface and Coatings Technology, Surface and Interface Analysis, Thin Solids Films and Nuclear Instruments and Methods in Physics Research B.

Excitation functions of the of proton- and deuteron-induced reactions on Zn-64, As-75, Y-89, Mo-100

Laboratory of Cyclotron and Fast Neutron Generators

Ondrej Lebeda

Proposal ID

64

Excitation functions of the of proton- and deuteron-induced reactions on ^{64}Zn, ^{75}As, ^{89}Y, ^{100}Mo

Ondřej Lebeda, Vlasta Zdychová, Jaroslav Červenák and Jan Štursa

Nuclear Physics Institute, Řež, Czech Republic
Czech Technical University, Prague

Detailed measurement of the deuteron-induced excitation functions on ^{89}Y in the energy range of 3.9–19.5 MeV was performed resulting in new excitation function for formation of ^{88}Zr, ^{89m}Zr, ^{89}Zr, ^{88}Y, ^{90m}Y and ^{87m}Sr (Fig. 1). The data were compared with previously published results and prediction of the TALYS code. Parallel use of titanium and aluminium beam monitors revealed systematic difference between the recommended cross-sections of both monitoring reactions and provided new cross-section data for formation of ^{24}Na, ^{27}Mg, ^{43}Sc, ^{44m}Sc, ^{44}Sc, ^{46}Sc, ^{47}Sc and ^{48}Sc (Fig. 1). Results were published in a peer-reviewed journal [1] and included in the EXFOR data base.

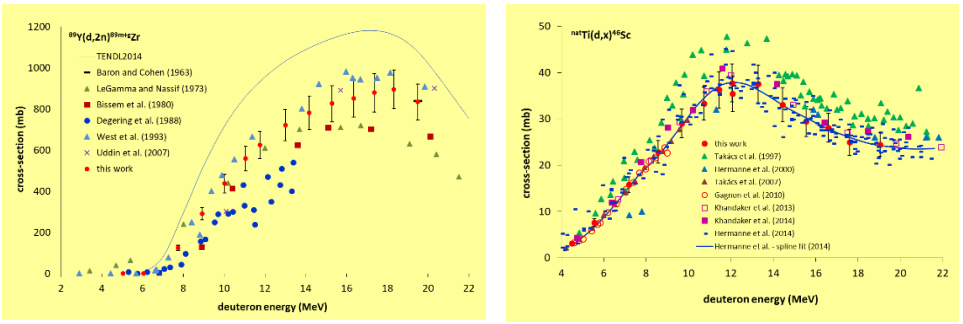

Fig. 1 Excitation function of the ^{89}Y(d,2n)$^{89m+g}$Zr for the formation of medically relevant ^{89}Zr amd excitation function of the ^{nat}Ti(d,x)^{46}Sc suitable for the beam monitoring

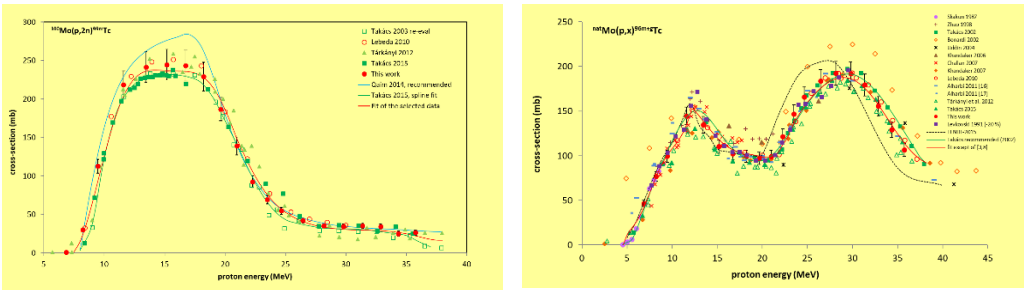

Fig. 2 Selected cross-sections for the ^{100}Mo(p,2n) nuclear reaction and fit of the recommended values; cross-sections for the beam monitoring reaction ^{nat}Mo(p,x)$^{96m+g}$Tc and their fitting resulting in the recommended data

Due to the lack of thin foils of precise thickness made out of highly enriched metals, we decided to re-measure excitation functions of protons on natural molybdenum, as the elemental cross-sections may be in the case of the nuclear reactions on ^{100}Mo converted into isotopic cross-sections. The extensive experiment allowed us then to provide another set of data important not only for the production of medically relevant ^{99m}Tc and ^{99}Mo, but also for the ^{nat}Mo(p,x)$^{96m+g}$Tc reaction relevant for both beam monitoring and TLA, as well as data for production of ^{95m}Tc, a suitable long-lived technetium tracer. Altogether, almost 30 excitation functions were obtained covering the proton beam energy range of 7–36 MeV, some of them were provided for the first time (^{97m}Tc, ^{88g}Nb, ^{88m}Nb and ^{89m}Nb) [2]. Results are included in the EXFOR data base.

Due to the problems with the target preparation, we have resigned on the measurement of the proton-induced excitation functions on ^{64}Zn. The sputtered targets made out of ^{75}As were not suitable for the proton beam activation, the bombardment resulted in their significant damage that didn't allow for obtaining reliable data.

The rich experimental material collected during the experiments was then included in an extensive works performed within the IAEA CRP project.

[1] Lebeda, O. – Štursa, J. – Ráliš, J. Experimental cross-sections of deuteron-induced reaction on ^{89}Y up to 20 MeV; comparison of ^{nat}Ti(d,x)^{48}V and ^{27}Al(d,x)^{24}Na monitor reactions. *Nuclear Instruments and Methods in Physics Research B*, 2015, vol. 360, pp. 118–128.
doi: 10.1016/j.nimb.2015.08.036

[2] Červenák, J. – Lebeda, O. Experimental cross-sections for proton-induced reaction on ^{nat}Mo. *Nuclear Instruments and Methods in Physics Research B*, 2016, vol. 380, pp. 32–49.
doi: 10.1016/j.nimb.2016.05.006

Carrier Lifetime Control in Bipolar 4H-SiC High Voltage Devices

Laboratory of Tandetron

Pavel Hazdra

Proposal ID

320

Carrier Lifetime Control in Bipolar 4H-SiC High Voltage Devices

P. Hazdra[1], S. Popelka[1] and A. Schöner[2]

[1] Czech Technical University in Prague, Czech Republic [2] Ascatron AB, Kista, Sweden

The effect of local lifetime control by proton irradiation on the static and dynamic parameters of 4H-SiC high voltage bipolar power devices was investigated. Recombination centers acting as lifetime killers were introduced locally by proton irradiation into 10 kV SiC PiN diode chips fabricated on lightly doped (< 10^{15} cm^{-3}) *n*-type 4H-SiC epilayers. Devices were irradiated from the anode side with 800 keV or 1000 keV protons to fluences from 5x10^{9} to 1x10^{11} cm^{-2} using the 3 MeV tandetron facility in NPI CAS Rez. The irradiation energy was chosen in order to place the damage peak beyond the anode junction. Diode static and dynamic parameters were characterized prior to and after proton irradiation. Radiation defects were characterized by capacitance deep level transient spectroscopy (DLTS) and C-V profiling. The excess carrier dynamics were measured by the OCVD and analyzed using the calibrated device simulator ATLAS from Silvaco, Inc.. Recombination models accounting for the effect of introduced deep levels were set according to experimental results obtained by C-V and DLTS.

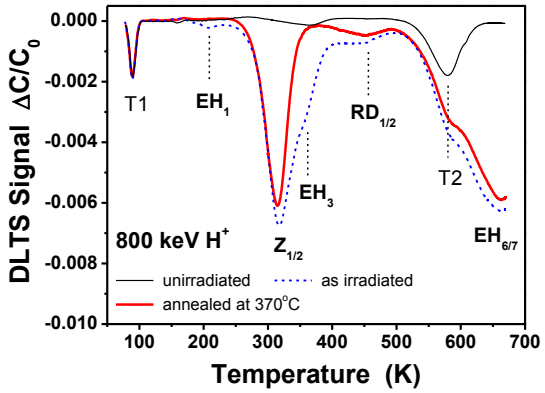

Fig. 1. DLTS spectra of *n*-base of the 4H-SiC PiN diode measured before (black thin) and after (short-dashed) irradiation with 800 keV protons to a fluence of 5x10^{9} cm^{-2} and after annealing at 370°C (red thick).

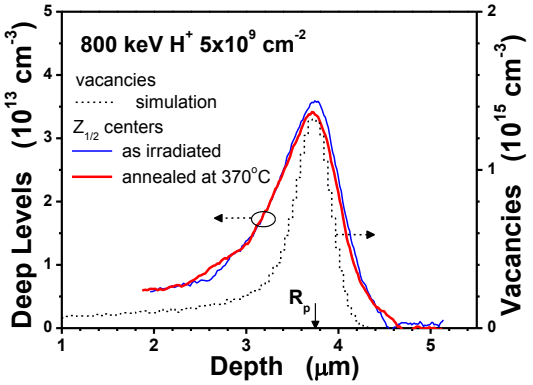

Fig. 2. Profile of the $Z_{1/2}$ centre in the *n*-base of the 4H-SiC PiN diode irradiated with 800 keV protons together with the simulated profile of primary vacancies (short-dashed).

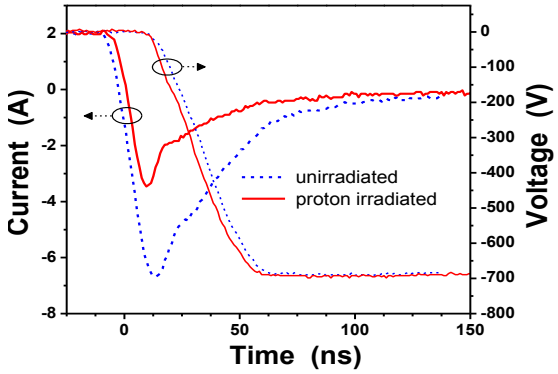

Fig. 3. Measured reverse recovery of an unirradiated SiC PiN diode and a diode irradiated with 800 keV protons to a fluence of 1x10^{11} cm^{-2} (room temperature).

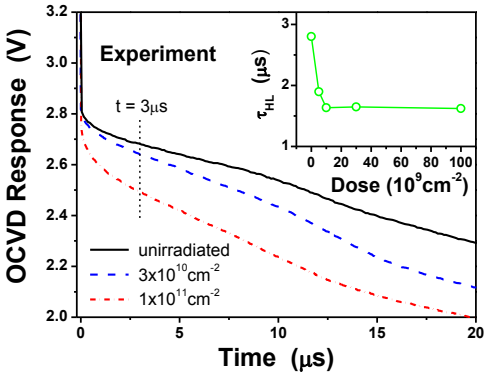

Fig. 4. Measured OCVD responses of 4H-SiC PiN diodes irradiated with different fluences of 800 keV protons. The values of high-level lifetime τ_{HL} (extracted at t= 3μs) for different irradiation fluences are shown in the inset.

Results show that proton implantation followed by low temperature annealing can be used for controllable local lifetime reduction in SiC devices. The dominant recombination centre is the $Z_{1/2}$ defect (Fig.1), whose distribution can be set by irradiation energy and fluence (Fig.2). The local lifetime reduction, which improves diode recovery (Fig.3), can be monitored by OCVD response (Fig.4) and simulated using the SRH model accounting for the $Z_{1/2}$ defect. Preliminary results were presented at the International Conference on Silicon Carbide and Related Materials 2017, Washington, USA, 17-22 September 2017 [1].

Reference

[1] P. Hazdra, S. Popelka, A. Schöner, Local Lifetime Control in 4H-SiC by Proton Irradiation, Mater. Sci. Forum 2018 (Proc. of ICSCRM 2018, Washington, 2017) to be published.

Reactions of organometallic complexes relevant for the ion beam cancer therapy

Laboratory of Cyclotron and Fast Neutron Generators

Marie Davidkova

Proposal ID

321

Reactions of organometallic complexes relevant for the ion beam cancer therapy

Dan Reimitz, Dept. of Nuclear Chemistry, Faculty of Nuclear Sciences and Physical Engineering, Czech Technical University in Prague
Marie Davídková, Dept. of Radiation Dosimetry, Nuclear Physics Institute of the CAS
Oto Mestek, Dept. of Analytical Chemistry, University of Chemical Technology, Prague
Jiří Pinkas, Jaroslav Kočišek, J. Heyrovský Institute of Physical Chemistry of the CAS

Experimental study explored combined effect of RAPTA C (Ru(η^6-p-cymene)Cl_2(1,3,5-triaza-7-phosphatricyclo-[3.3.1.1]decanephosphine)) or CDDP (cis-diamminedichloridoplatinum(II)) and radiation on the DNA damage formation. DNA plasmids pBR322 have been irradiated by Co-60 gamma rays in presence of free and bound studied ligands. Changes of DNA plasmid conformation have been evaluated using agarose gel electrophoresis.

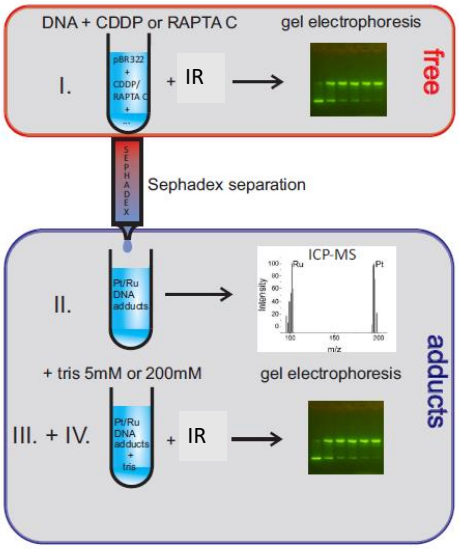

Figure 1: Scheme of the experiments performed in this study.

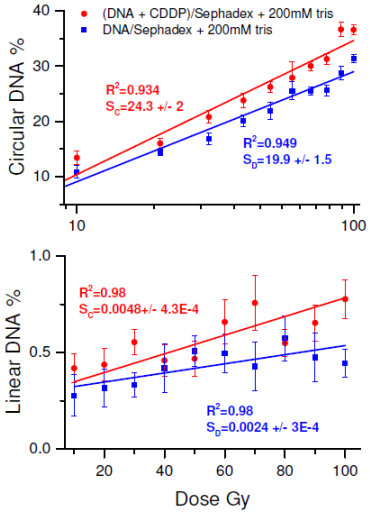

Figure 2: Radiation induced damage to DNA modified by CDDP at the level of ~6 Pt/plasmid in the presence of 200mM tris buffer.

When irradiating plasmid DNA in solution with free molecules by gamma rays, no combined effect was observed, indicating that the contribution to DNA damage caused by products of radiolysis of RAPTA C or CDDP is negligible in comparison to the damage caused by products of radiolysis of water. After binding to DNA, CDDP adducts with DNA strongly enhanced the damage in a good agreement with the results of other studies. RAPTA C adducts acted radio-protective at low doses of OH radical scavenger - tris(hydroxymethyl)aminomethane (tris) and showed no combined effects at higher tris levels. Radioprotectivity of RAPTA C is therefore primarily caused by enhanced resistance of RAPTA C modified DNA against the damage induced by radicals.

The same experiments have been performed also using 30 MeV proton beam at the U120M cyclotron. The goal of the study is to understand the effect of radiation quality on primary radiation damage to DNA and possible changes of radiomodifying properties of studied organometalic compounds. The results are currently under evaluation. Future studies using other types of organometalics, namely titanocenes, are planned in close future.

INTERNAL: Residual stresses in a direction perpendicular to the weld

Neutron Physics Laboratory - Neutron diffraction

David Canelo Yubero

Proposal ID

198

Report regarding CANAM proposal **"INTERNAL: Residual stresses in a direction perpendicular to the weld"**

Ľ. Mráz[1], Ch. Hervoches[2], M. Vrána[2], P. Mikula[2,a], J. Kotora[3]

[1]*Welding Research Institute – Industrial Institute SR, Bratislava, Slovak Republic*
[2]*Nuclear Physics Institute ASCR, v.v.i.,25068 Řež, Czech Republic*
[3]*SES Tlmače, Slovak Republic*

Circumferential weld of a tube made of 7 CrMoVTi10-10 creep resistant steel diameter of ∅ 38 mm and wall thickness of 6.3 mm has been prepared for this investigation. TIG process, medium alloyed filler material W Z CrMo2VTi (Union I P24) (typical content Cr = 2,2 %, W = 1,7 %) and argon as shielding gas have been used for welding. The heats input in the range of 8.0 to 13.0 kJ cm, preheat temperature 150 °C to 200 °C and interpass temperature max. 250 °C have been applied.

Fig. 1: Circumferential test weld of 7 CrMoVTi10-10 creep resistant steel

Neutron diffraction has been performed in order to identify residual stress distribution in the vicinity of the circumferential weld. Hoop, radial and axial residual strains have been measured for the as-welded specimen and after long term heat treatment at the temperature 450 °C for 48 hours.

Axial, radial and hoop stresses have been calculated in the vicinity of the test weld (Fig. 2). The results show a clear drop of all stress components after low temperature long term heat treatment.

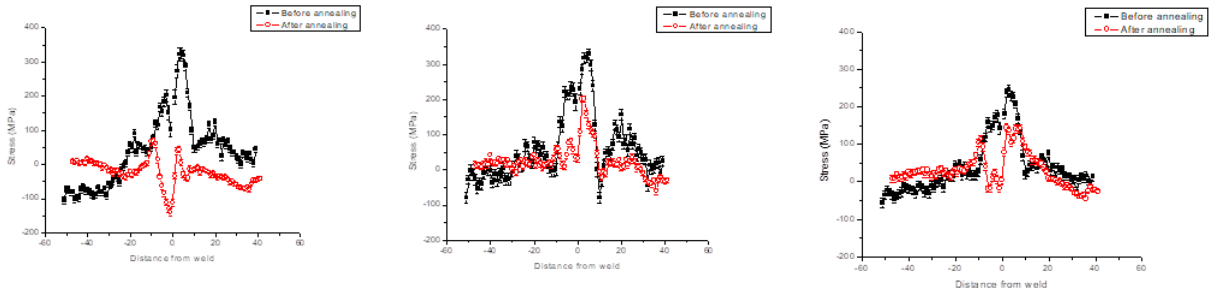

Axial Hoop Radial

Fig. 2: Residual stresses in the vicinity of the test weld in the Axial, Hoop, and Radial directions, before (in black) and after (in red) annealing at 450 °C for 48 hours.

Quantification of elements in nanocarbons by Neutron Activation Analysis (NAA).

Neutron Physics Laboratory - Nuclear analytical methods with neutrons

Filipa Fernandes

Proposal ID

328

SIGMA-ALDRICH®
sigma-aldrich.com
3050 Spruce Street, Saint Louis, MO 63103, USA
Website: www.sigmaaldrich.com
Email USA: techserv@sial.com
Outside USA: eurtechserv@sial.com

Certificate of Analysis

Product Name:
Carbon nanotube, single-walled - (7,6) chirality, carbon >90 %, ≥77% (carbon as SWNT), 0.7-1.1 nm diameter

Product Number:	**704121**
Batch Number:	**MKBT4053V**
Brand:	ALDRICH
CAS Number:	308068-56-6
Quality Release Date:	05 DEC 2014

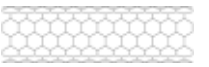

Test	Specification	Result
Purity T1% (Estimate of SWNT Content by Weight (TGA))	≥ 77.0 %	91.5 %
Residual Mass (TGA)	≤ 10.0 %	3.4 %
Carbon (TGA)	≥ 90.0 %	95.5 %
Chirality Distribution P2B (QC Parameter for control of chirality distribution at 1130-1140 nm (UV-vis-NIR Spectroscopy))		1.25
Quality Factor Q (D:G Ratio)Raman Spectroscopy	≥ 0.940	0.960
Note Please see Technical Bulletin AL-252 for explanation of quality parameters. Spectra available upon request.	Complete	Conforms

Ali Ataei, Manager
Quality Control
Milwaukee, WI US

Calibration of dosimeters and particle trackers for atmosphere and space radiation research

Laboratory of Cyclotron and Fast Neutron Generators

Carlos Granja

Proposal ID

331

Report for experimental proposal "**Calibration of dosimeters and particle trackers for atmosphere and space radiation research**"

C. Granja, *M. Sommer, M. Kakona, V. Stepan, I. Ambrozova,* et al., ODZ-UJF/CRREAT*

V. Zach, T. Matlocha, J. Stursa, et al., OU-UJF/CANAM

Summary: Measurements were carried out using proton beams from the UJF-CANAM Cyklotron on various types of radiation detectors selected for studies of radiation phenomena in the atmosphere in frame of the running OP3V project CRREAT. Performed tasks consisted of testing and calibration of detection response as well as intercomparison of different detector technologies (see Fig. top row) including passive devices such as TLDs and track detectors, and active devices such as single diode devices (LIULIN dosemeter, single pad diode CANDY) as well as position-sensitive imaging devices semiconductor pixel detectors. Timepix' resolving power and track visualization of single particles to a given radiation component (protons) of varying energy is shown (see Fig. middle row). Work included measurements on customized instrumentation for air-crew and space radiation dosimetry such as TEPC (Tissue Equivalent Proportional Counters – see Fig. bottom row). Data is presently under evaluation. Results will be subject of presentation/contribution at 1-2 conferences and 1-2 scientific journal articles.

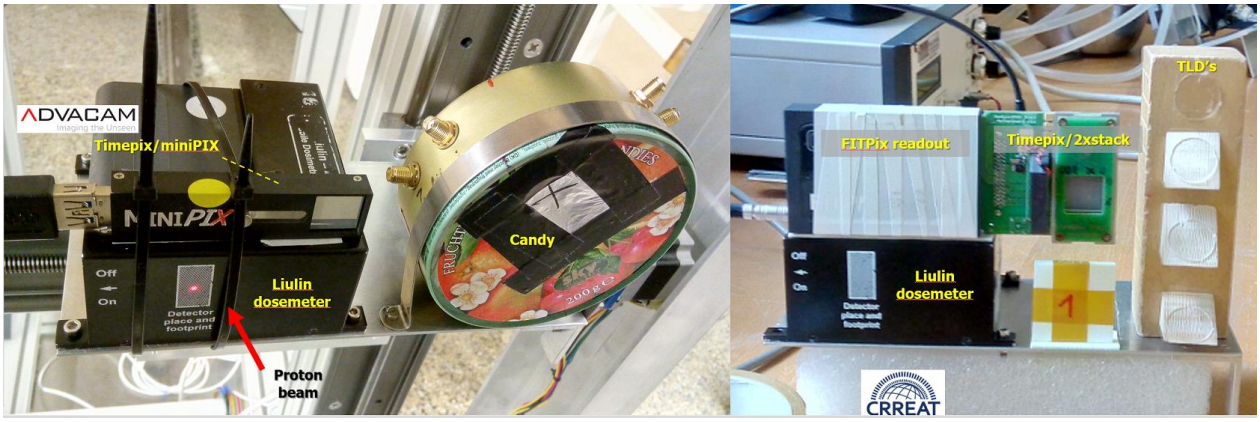

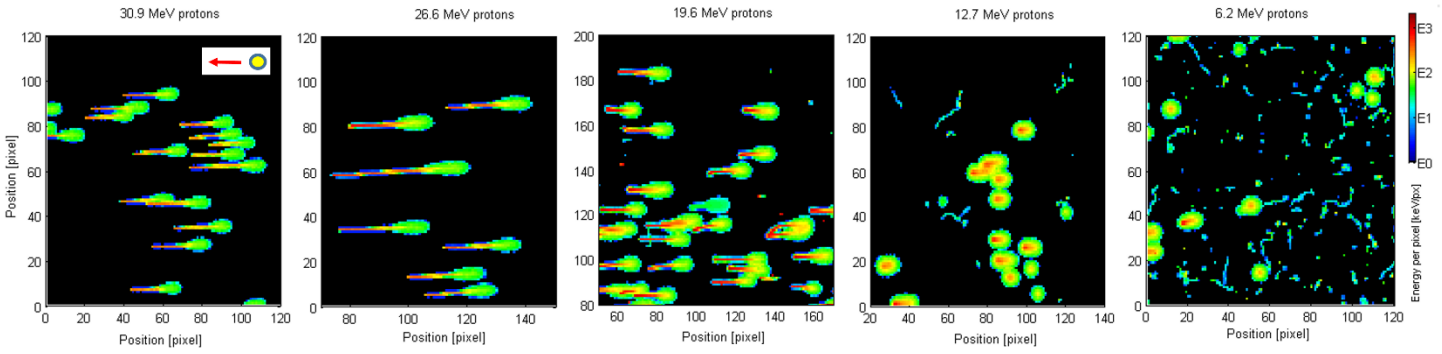

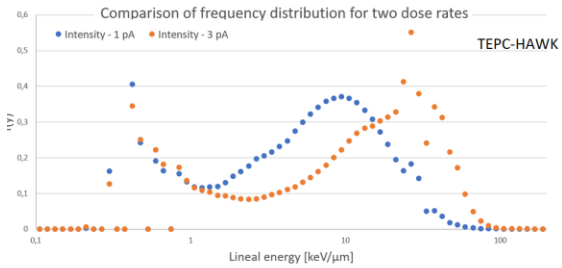

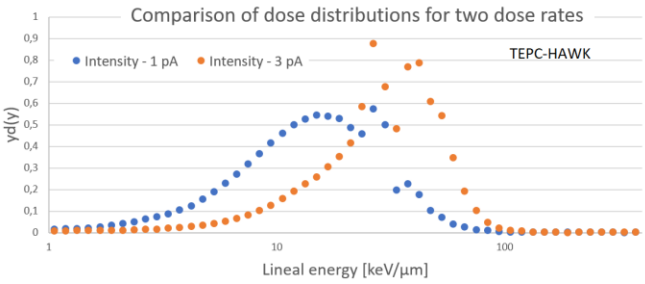

(*) Research performed in frame of the CRREAT project (Research Centre of Cosmic Rays and Radiation Events in the Atmosphere) supported by European Regional Development Fund-Project CZ.02.1.01/0.0/0.0/15_003/0000481.

Identification of microscopic uranium particles using fission tracks in solid detectors

Neutron Physics Laboratory - Nuclear analytical methods with neutrons

Jan Lorincik

Proposal ID

332

Report regarding proposal " **Identification of microscopic uranium particles using fission tracks in solid detectors"**

J. Lorinčík, K. Sihelská, K. Řezanková, F. Sus, Vl. Strunga, J. Kučera

The goals of this project were (A) the study of the number of fission tracks as a function of enrichment and size of U-particles, (B) the optimization of the fission track (FT) procedure for higher reproducibility, robustness, and accuracy.

A quantitative relation between the U-particle enrichment, size, and the number of FTs was used in the following form *[1]*: $N_T = N_{235} \cdot \sigma_f \cdot \varepsilon \cdot t \cdot \phi_{therm}$ … (1) , where N_T denotes the number of fission tracks; N_{235}, the number of ^{235}U atoms in a particle; σ_f, the fission cross section for ^{235}U [586 b]; ε, the registration efficiency (0,4); t, the irradiation time [120 s]; Φ_{therm}, the flux of thermal neutrons [3,2 x 10^{13} $cm^{-2}s^{-1}$]. Then, N_{235} can be obtained from $N_{235} = 3 \cdot (\rho_{U3O8} \cdot V_P)/M_{U3O8} \cdot N_A \cdot A_{235}/100$ … (2), where ρ_{U3O8} is U_3O_8 particle density [8,3 g/cm^3], V_P volume of the particle [cm^3], M_{U3O8} the molar mass of U_3O_8 [842,1 g/mol], N_A the Avogadro's constant, A_{235} the enrichment [%]. Constant 3 in eq. (2) corresponds to the number of U atoms in U_3O_8 molecule. Since SEM images can provide only areas of 2D projections (characterized by equivalent circle diameter – d_{ECD}) of 3D shapes of particles, the geometry models, e.g. sphere, cylinder, cube must be used for *Vp* estimation.

For experimental work, standard reference materials of U_3O_8 were used: CRM 129-A (NU), CRM 010 (1% ^{235}U enriched), CRM 030-A (3% ^{235}U enriched). Then FT sample assemblies (see more detail in reports of project CANAM:ID241) were prepared and irradiated in the reactor LVR-15 with irradiation parameters specified above. After etching of the Lexan detectors, optical images were made (see Fig. 1 a-c) and the FTs manually counted. The comparison of theoretical estimates and experimental data (lines vs. data points) is in Fig. 1 d.

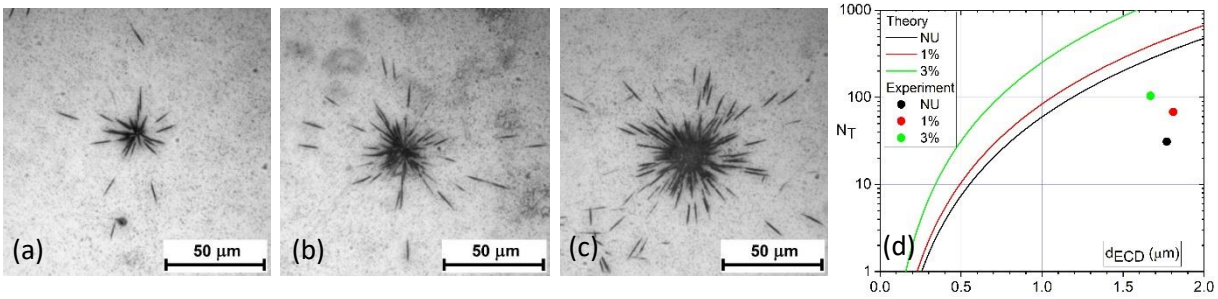

Figure 1.Optical images of FTs corresponding to U_3O_8 particles of NU (a),1 %U (b),and 3%U (c) [2]. Number of registered FTs in the images (a)-(c) for NU, 1%U, 3%U is 31, 68, 104, resp. (d) Comparison of experimental values (circle symbols) and theoretical estimates (full lines) based on equations (1) and (2) for spherical geometry model ($V_P = \pi/6 \cdot d_{ECD}^3$).

In parallel to the above study, large effort has been spent on improvement of the FT procedure. This goal has been achieved by (i) reconfiguration of the fiducial marks for better particle position precision, (ii) addition of sticky collodion for better particle adhesion, (iii) redesigning of the FT sample assembly for simpler and more reliable manipulation, (iv) employing new optical microscope with motorized stage for automated creation of compound photos of large areas of the Lexan detector, and (v) implementing efficient coordinate transformation algorithm for transfer of particle coordinates between instruments.

In summary, the dependence of the number of FTs on the particle enrichment and size has been investigated both theoretically and experimentally. There is a discrepancy between the theoretically predicted numbers of FTs and the counts of FTs obtained from the experiment. A combined effect of overestimated values of neutron fluences, material density, and FT registration efficiency could have been responsible for that. More experiments are needed to support that explanation and to provide more accurate data for theoretical predictions.

The main outcome of this project is substantial improvement of the FT procedure, which achieved the readiness level that allowed for the proficiency testing for nuclear safeguards.

[1] O. Stetzer, et al, . Nucl. Instr. Meth. Phys. Res. A525 (2004), pp. 582-592.
[2] S. Konegger-Kappel, et al https://www.iaea.org/sites/default/files/19/07/cn-267-book-of-abstracts.pdf, CN267-226, pp.228.

Residual stress measurement extension for contour cut method

Neutron Physics Laboratory - Neutron diffraction

Josef Hodek

Proposal ID

340

Final report 'Residual stress measurement extension for contour cut method'

J. Hodek, A. Prantl, COMTES FHT a.s., Dobrany, Czech Republic

Residual stress is hard to obtain for bulk objects. The contour method can determine residual stress distribution for bulk objects. The neutron diffraction measurement was done to obtain measurement that can be comparable to the contour method computation and the finite element method computation of the heat treatment. The sample is a cylinder of 316L material D30/60mm. The residual strains were measured along three radial lines (distant 120° from each other) in three directions (Radial, Hoop, Axial) using a 3x3mm slit, from ~3mm below the surface to maximal possible depth, with a step size of 3mm. The residual stress was computed from measured strains [1]. The computed stresses were compared for FEM computed stresses see Fig. 2-Fig. 10 (where FEM means computation in R - radial, H - hoop and A - axial direction and N means stress computed from neutron stress measurement in 1, 2, 3 measurement direction). The FEM model and contour method stresses were examined and analysed.

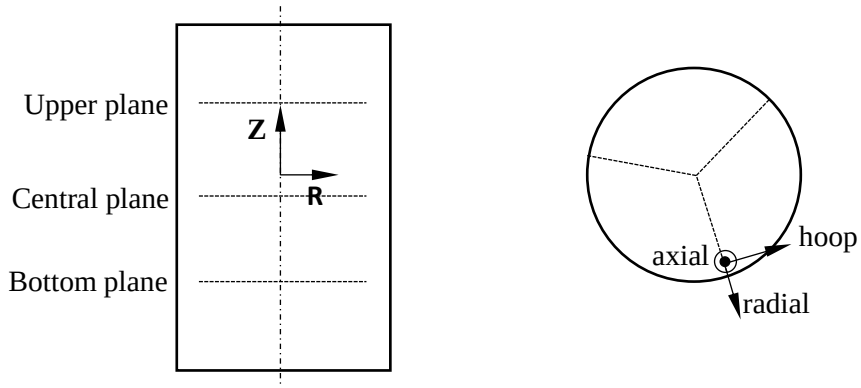

Fig. 1 Schematic of planes and directions of measurement and measured deformation directions

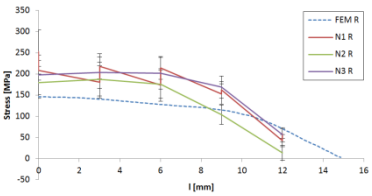

Fig. 2 Stress radial - central plane

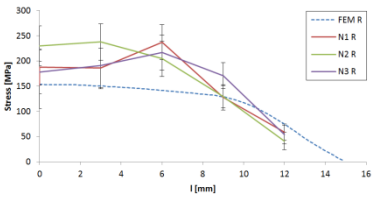

Fig. 3 Stress radial - bottom plane

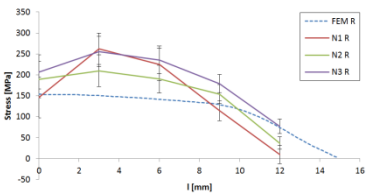

Fig. 4 Stress radial - upper plane

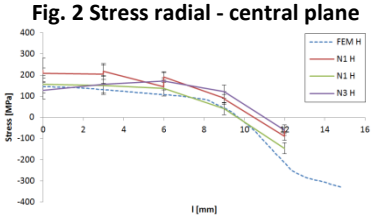

Fig. 5 Stress hoop - central plane

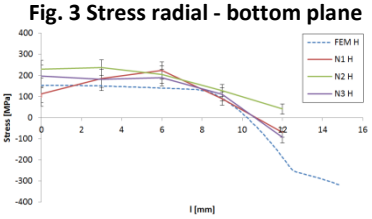

Fig. 6 Stress hoop - bottom plane

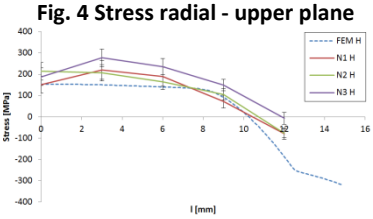

Fig. 7 Stress hoop - upper plane

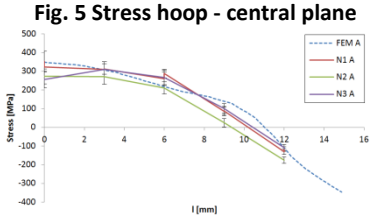

Fig. 8 Stress axial - central plane

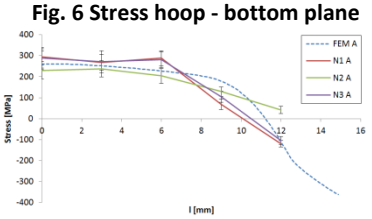

Fig. 9 Stress axial - bottom plane

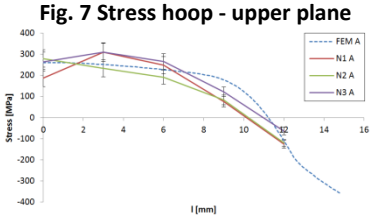

Fig. 10 Stress axial - upper plane

[1] HUTCHINGS, Michael T., et al. *Introduction to the characterization of residual stress by neutron diffraction*. CRC press, 2005.

Ex-situ & In-situ investigation of CP Titanium grade 2 prepared by CONFORM ECAP and rotary swaging

Neutron Physics Laboratory - Neutron diffraction

Gergely Németh

Proposal ID

347

Report regarding proposal "Ex-situ & In-situ investigation of CP Titanium grade 2 prepared by CONFORM ECAP and rotary swaging"

Gergely Németh, Charles University, Czech Republic

Neutron diffraction experiments were performed on commercially pure titanium grade 2 specimens in the following 9 conditions: without mechanical treatment (initial state), after 1x, 2x and 3x passes through CONFORM ECAP machine and these same conditions were applied on other samples before they underwent an additional mechanical treatment using the rotary swaging method. Finally, one sample was heat treated (HT). Samples were in the form of cylindrical rods with diameter 10 mm (only CONFORM ECAP samples) and 4,68 mm (rotary swaged samples).
101 and 002 reflections were measured for a few hours on each sample. The gauge volume was placed in the center of specimens. Residual strains were calculated from the position of diffraction peaks relative to the position of diffraction peaks of material in the initial state. FWHM were determined from diffraction peaks too. The results are on *fig.1 a, b, c, d*.

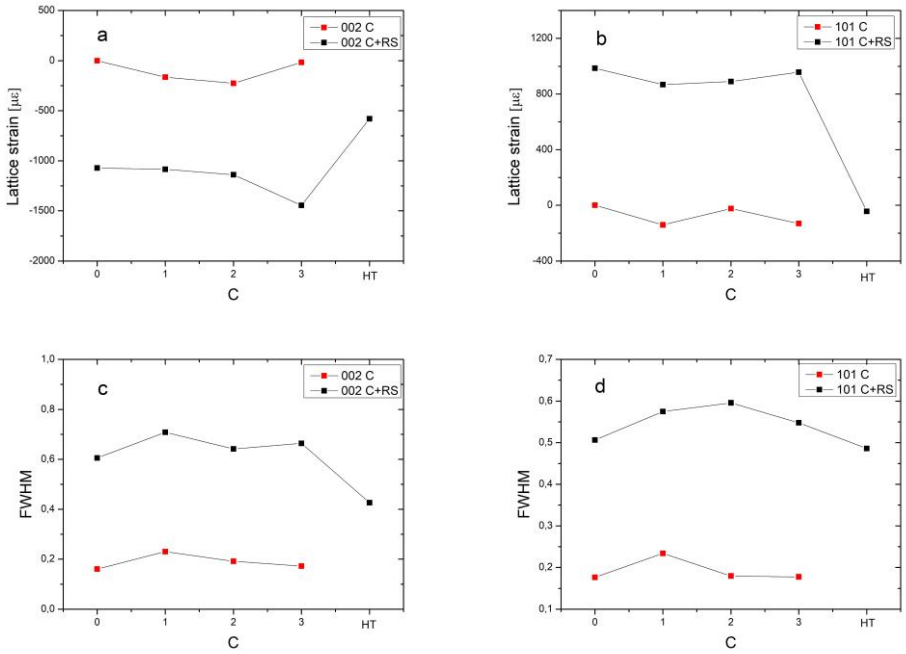

Fig.1-a, b) Calculated residual strains c, d) Determined FWHM as the function of number of passes through CONFORM ECAP (C-CONFORM ECAP, C+RS-CONFORM ECAP + rotary swaging; HT-Heat treated)

From *fig. 1-a* and *b* we can deduce that rotary swaging generated an additional residual macro-strain with tensile character in the case of reflection 002 and residual macro-strain with compression character in the case of 101 reflection. The CONFORM ECAP treatment has the effect of residual macro-strain with tensile character. On *fig. 1-c* and *d* it is seen that rotary swaging increased three times the value of FWHM parameter which may be caused by increased crystallographic defects in the material after the cold working process. In case of the samples treated only with CONFORM ECAP, after the first pass, FWHM is increased slightly but after the second and third pass FWHM was almost recovered to the initial state.
In-situ neutron diffraction during heat treatment was carried out on samples in conditions: passed 1x CONFORM ECAP machine and 1x CONFORM ECAP + rotary swaged. Heat treatment was stepwise. Temperature steps were 20 K and the holding time was 1 hour. During this time neutron diffraction data were collected. The temperature range was 100 °C – 600 °C. The measured reflection was the 002 reflection. The results are on *fig. 2-a* and *b*.

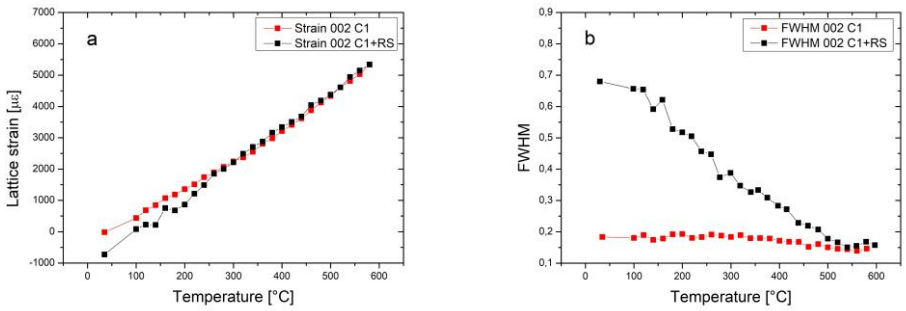

Fig.2 a) Calculated strain, b) Determined FWHM, as the function of temperature

On *fig. 2-a* it is seen that the difference in residual macro-strains between two samples vanished above 350 °C. However, in the case of rotary swaged sample the FWHM parameter is decreasing continuously until it reaches the value of FWHM parameter of the sample treated only with CONFORM ECAP method.
The correlation of the gained results with results from other experimental methods is still in progress.

Comparative study of performance of Silicon and Silicon Carbide detectors during RBS and ERDA.

Laboratory of Tandetron

Lorenzo Torrisi

Proposal ID

348

Comparative study of performance of Silicon and Silicon Carbide detectors during RBS and ERDA

L. Torrisi[1], V. Havranek[2], M. Cutroneo[2], A. Mackova[2] and A. Torrisi[2]

[1]Dipartimento di Scienze Fisiche MIFT, Università di Messina, Italy
[2]Nuclear Physics Institute, AS CR, Rez, Czech Republic

SiC are able to detect radiation at low and high energy, due to the controllable active region depth using adapt inverse bias of the Schottky barrier in presence of a thin surface metallization of contact. We have demonstrated that it is possible to use SiC diodes to detect helium ions with energy in the range of about 0.1–6.0 MeV with a sufficient energy resolution, similar to that of silicon detectors, capable to be employed for qualitative and quantitative RBS analyses. The experiment was performed using a prototype diode with a surface metalized semiconductor, 200 nm thickness in Ni_2Si alloy, with up to 80 μm active region depth, using a bias of −200 V at which this active region is reduced to about 20 μm active region. Such devices permit to distinguish ions of different energy, i.e. atomic numbers of different targets using RBS analysis and ion currents. Results demonstrated that the SiC energy resolution is comparable to that of Si, although worse. Si-barrier detector show higher energy resolution that permits to acquire significant RBS spectra using 1–6 MeV helium beam and SiC can be tailored designed to have a similar energy resolution. In this way, the surface metallization thickness must be reduced in order to reduce the ion energy loss and straggling in this passive absorber. The detection electronic line has been optimized to improve the impedance matching of the devices with the preamplifier, in order to improve the signal-to-noise ratio.

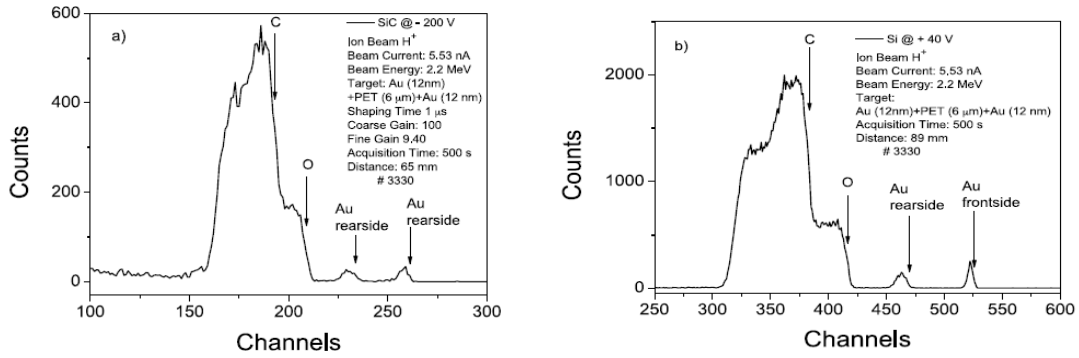

Fig.1: RBS comparison analysis obtained using 2.2 MeV proton energy, 5.5 nA current, with 500 s acquisition time, irradiating a thin polymeric (PET) film with 6 μm thickness, covered in front and back by 12 nm Au gold film acquired using SiC (a) and Si (b) detectors.

It is important to remind that SiC is superior to Si for some advantages, such as the higher energy gap that permits to be transparent to visible radiation and to be used to detect ions also in presence of high visible radiation, such as in plasmas ion emission or during ion irradiations of insulators, such as oxides and ceramics, emitting high fluorescent light intensity. SiC shows a lower reverse current, of about 10 pA at room temperature, two order magnitude lower with respect to Si, conferring higher sensitivity to the device. SiC is radiation resistant due to the higher bonding energy Si-C with respect to Si-Si, making it possible to use even in harsh conditions, such as plasmas and high temperatures, giving rise to a damage threshold due to absorbed doses much higher than that in silicon. Thus, SiC can be employed also to monitor on-line ion beams and lasers interacting with solids, to detect the radiations emitted from low and high temperature plasmas and to observe ion scattering processes from many materials. Their use can be optimized not only at low ion energy but also at high ion energy, increasing the active depth of the sensible detector region. Moreover their optimization can be performed also to detect UV, soft and hard X-rays and electrons generated by different sources, such as pulsed plasmas and particle beams.

References:

1) L. Torrisi, V. Havranek, M. Cutroneo, A. Mackova, L. Calcagno, A. Cannavò and A. Torrisi, "SiC detector for high helium energy spectroscopy", *NIM A* 903 (2018) 309–316.
2) A. Sciuto , G. D'Arrigo, S. Di Franco, M. Mazzillo , G. Franzò, L. Torrisi, and L. Calcagno, "4H-SiC Detector in High Photons and Ions Irradiation Regime", *IEEE Trans. on Electron Devices* 65(2), 2018, 599-604.
3) A. Torrisi, P.W. Wachulak, H. Fiedorowicz, and L.Torrisi, "SiC detectors for evaluation of laser-plasma dynamics employing gas-puff targets", *Nucl. Instr. and Meth. A*, 922 (2019) 250–256.

Investigation of residual strains of commercially pure Titanium grade 2 prepared by CONFORM ECAP

Neutron Physics Laboratory - Neutron diffraction

Gergely Németh

Proposal ID

349

Report regarding proposal “Investigation of residual strains of commercially pure Titanium grade 2 prepared by CONFORM ECAP”

Gergely Németh, Charles University, Czech Republic

Neutron diffraction experiments were performed on commercially pure titanium grade 2 specimens in the following 4 conditions: without mechanical treatment (initial state), after 1x, 2x and 3x passes through CONFORM ECAP machine. The samples were in cylindrical shape with diameter ~10 mm and length 80 mm. The samples were placed on the xyz stage which allowed samples to move in any direction. The sample gauge volume was ~32,5 mm^3. Three scans were performed along the same line on each sample according to diffraction vector orientation in the sample's coordinate system: a scan, where diffraction vector was parallel to - axial direction $\overrightarrow{q_A}$, radial direction $\overrightarrow{q_R}$ and hoop direction $\overrightarrow{q_H}$. The measured 2θ angles of reflection $(10\bar{1}1)$ in initial state sample between points -2 and 2 served as the strain free reference for further calculation of residual strains, because they did not show any gradient (Fig. 1. a). The calculated lattice strains in three directions (axial, radial, hoop) for each sample are shown in Fig. 1. *b*, *c* and *d*.

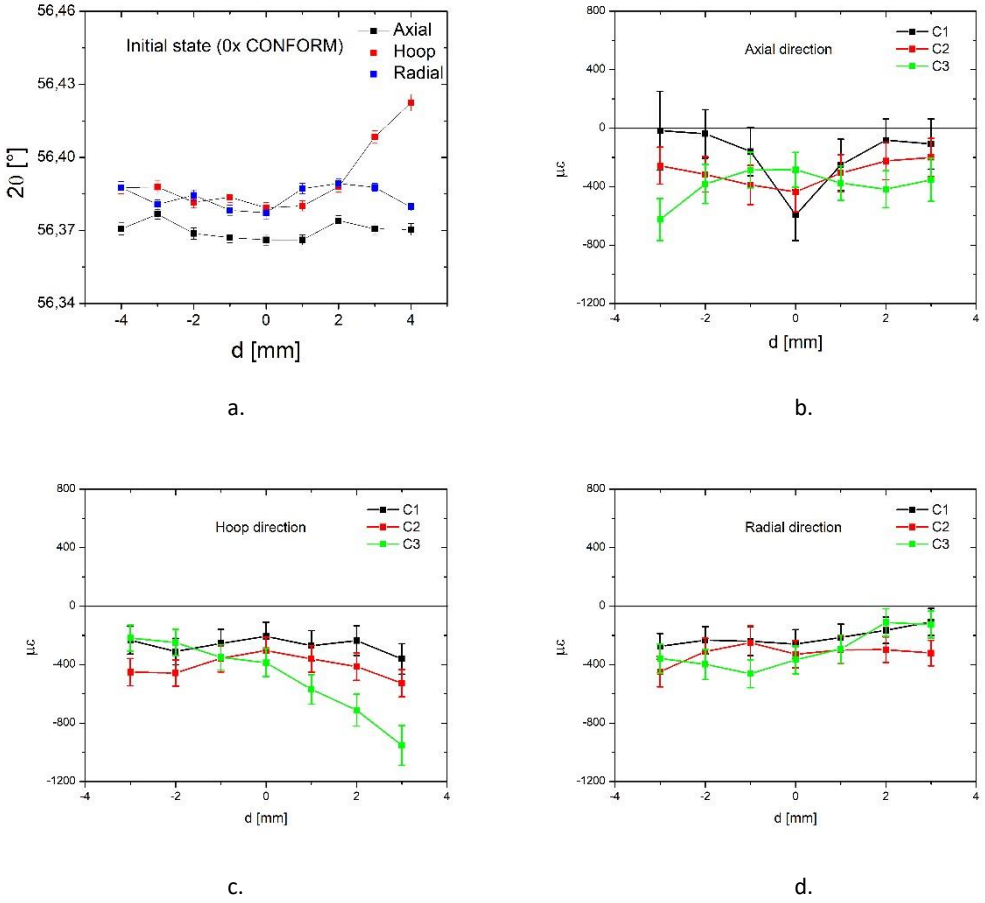

Fig.1.-Measured 2θ angles of (a) initial state sample and the lattice strain distribution relative to the centre of the samples (d=0 mm) in b. axial, c. hoop, d. radial direction after 1, 2 and 3 passes of CONFORM ECAP treatment

On the Fig. 1.b. it is seen that the sample after 1x CONFORM ECAP treatment (C1) exhibits large lattice strain gradient towards the edges in the axial direction. Between points -3 and 3 mm there is a symmetric distribution of the strains around the centre. However, the lattice strain in the hoop (c) and in the radial (d) direction shows relatively homogeneous distribution. Concerning the sample after 2x CONFORM ECAP treatment (C2), the large gradient of the lattice strain after the first pass in the axial direction was removed and the sample exhibits a symmetrical distribution for axial (b) and hoop (c) directions between points -3 and 3 mm. The lattice strain distribution in the sample after 3x CONFORM ECAP treatment (C3) does not show any symmetricity and there are relatively big differences in the values in all three directions except points between -2 and 0. In general, residual strains with compression character prevail in all samples.

The gained results indicate that further investigations are needed to clarify the reasons of the differences between the samples.

Fabrication of ion implanted integrated optical elements

Laboratory of Tandetron

István Bányász

Proposal ID

351

Report on project "Fabrication ion implanted integrated optical elements"

I. Bányász, Wigner Research Centre for Physics, Budapest, Hungary

I. Rajta, G.U.L. Nagy, Atomki, Institute for Nuclear Research, Debrecen, Hungary

V. Vosecek, V. Havránek, Nucl. Physics Inst., Řež, Czech Republic

1.
2. **Channel waveguides and Mach-Zehnder microinterferometers**

We planned to fabricate the channel waveguides and Mach-Zehnder interferometers with tapering, coupling gratings and with improved lateral confinement.

Experiments completed

The following structures have been fabricated:

1. Single channel waveguides in a KTP crystal, 5 MeV N^{3+} microbeam, fluence = $5\cdot10^{14}$ -$8\cdot10^{15}$ ions/cm^2.
2. Mach-Zehnder microinterferometres in a KTP crystal, 5 MeV N^{3+} microbeam, fluence = $5\cdot10^{14}$ -$8\cdot10^{15}$ ions/cm^2.
3. Single channel waveguides in a RTP crystal, 5 MeV N^{3+} microbeam, fluence = $5\cdot10^{14}$ -$8\cdot10^{15}$ ions/cm^2.
4. Mach-Zehnder microinterferometres in a RTP crystal, 5 MeV N^{3+} microbeam, fluence = five$\cdot10^{14}$ -$8\cdot10^{15}$ ions/cm^2.
5. Single channel waveguides in an Yb: KYW crystal, 5 MeV N^{3+} microbeam, fluence = $5\cdot10^{14}$ -$8\cdot10^{15}$ ions/cm^2.
6. Mach-Zehnder microinterferometres with grating couplers at both ends in an Yb: KYW crystal, 5 MeV N^{3+} microbeam, fluence = $5\cdot10^{14}$ -$8\cdot10^{15}$ ions/cm^2.
7. Single channel waveguides in a KTP crystal, 5 MeV N^{3+} microbeam, fluence = $5\cdot10^{14}$ -$8\cdot10^{15}$ ions/cm^2.
8. Single channel waveguides in a KTP crystal, 10.5 MeV N^{4+} microbeam, fluence = $1.25\cdot10^{14}$ - $4\cdot10^{15}$ ions/cm^2. Side-walled channel waveguides were also fabricated.
9. Mach-Zehnder microinterferometres in a KTP crystal, 10.eV N^{4+}microbeam, fluence = $6.25\cdot10^{13}$ -$4\cdot10^{15}$ ions/cm^2. Side-walled Mach-Zehnder microinterferometers were also fabricated.
10. Single channel waveguides in a RTP crystal, 10.5 MeV N^{4+} microbeam, fluence = $2.5\cdot10^{14}$ - $4\cdot10^{15}$ ions/cm^2. Side-walled channel waveguides were also fabricated.
11. Mach-Zehnder microinterferometres in a RTP crystal, 10.5 MeV N^{4+}microbeam, fluence = $1.25\cdot10^{14}$ - $2\cdot10^{15}$ ions/cm^2. Side-walled Mach-Zehnder microinterferometers were also fabricated.
12. Single channel waveguides in an Yb: KYW crystal, 10.5 MeV N^{3+} microbeam, fluence = $2\cdot10^{14}$ -$4\cdot10^{15}$ ions/cm^2. Side-walled channel waveguides and side-walled channel waveguides were also fabricated.

Tests completed

1. All the structures were measured with a confocal microscope to determine the profiles of the surface relief structures created.
2. Micro-Raman measurements, performed at the polished edges of the channel waveguides, revealed their depth profile.
3. Measurements showed that some of the as implanted single channel waveguides and Mach-Zehnder microinterferometres written in an Yb: KYW crystal had low propagation losses at a wavelength of 1450 nm.

3. **Microwells**

We tried to fabricate microwell arrays for biochemical sensors in a polymer (Zeonor) and a special glass (Gold Seal).

Experiments completed

1. **Zeonor Polymer**

Microwells were written in a Zeonor sample with 10.5 MeV N^{3+} microbeam, at fluences = $1\cdot10^{13}$ - $1\cdot10^{14}$ ions/cm^2.

2. **Gold Seal Glass**

Microwells were written in a Gold Seal sample with 10.5 MeV N^{3+} microbeam, at fluences = $1\cdot10^{14}$ - $4\cdot10^{14}$ ions/cm^2.

Tests completed

Preliminary AFM tests showed that some microwell groups in the Zeonor sample are good for use in sensors. The experiment has to be repeated with the same materials so that optimum geometrical parameters and fluences could be determined.

4. **Planar waveguides implanted with Ag ions**

Experiments completed

Planar optical waveguides were implanted in KTP and RTP crystals, using 11 MeV Ag^{3+} ions. Eight waveguides were fabricated in the two samples, with the fluences from $3\cdot10^{15}$ ions/cm^2 to $1\cdot10^{14}$ ions/cm^2.

Tests completed

Spectral ellipsometric tests of all the planar waveguides were performed. Even the raw ellipsometric spectra showed that the refractive index modulation induced in the samples by the Ag^{3+} ion implantation was rather low. Consequently, we plan to repeat this experiment with higher fluences up to $5\cdot10^{16}$ ions/cm^2.

Ion beam modification of carbon allotropes

Laboratory of Tandetron

Petr Malinsky

Proposal ID

352

Report regarding proposal “Ion beam modification of carbon allotropes”

P. Malinský, A. Macková. M. Cutroneo, V. Hnatowicz, K. Szökölová, M. Boháčová,
R. Böttger, J. Luxa, Z. Sofer

The proposal was denoted to the study of light and heavy ion irradiation of graphene oxide (GO) with the aim of GO reducing to the graphene like structure and simultaneously change its electrical properties. The GO is a carbon allotrope that is highly studied due to its excellent properties and potential in the field of nano-composites, solar cells, super-capacitors, micro- and nano-electronic [1–3]. GO is the single mono-molecular layer of graphene with various oxygen containing functionalities at edges and basal planes, due to the carbon atoms in the GO structure having a mixture of sp^2 and sp^3 hybridization. [2,4] Non-modified GO is an insulator due to the disruption in the sp^2 bonded graphitic structures and can be converted to semi- conductivity or conductivity state by changing the sp^2/sp^3 ratio. [5,6].

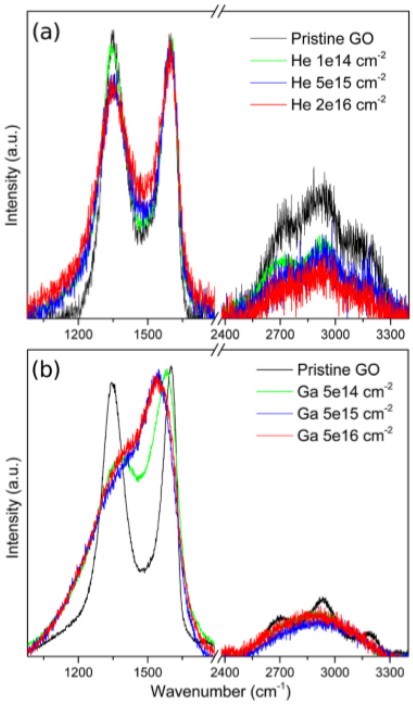

Figure 1: Raman spectra of GO film irradiated using various fluencies of 500 keV He ions (up) and Ga ions (down) compared to pristine GO film.

The GO foils were irradiated using He, H, Au and Ga ions with energies in the range from 500 keV to 5.1 MeV to the different fluencies and subsequently analyzed by ERDA, RBS, XPS, SEM and Raman spectroscopy to characterize the elemental composition, elemental depth profiles, subsurface chemical bonds and chemical composition modification as well as the surface morphology. The electrical properties of pristine and irradiated GO foils were measured by the standard two points method.

It can be concluded that the irradiation using heavy ions (Au, Ga) leads to strong changes in GO film structure and to the significant elemental composition modification, deoxygenation and dehydrogenation, which are connected to significant energy transfer from the heavy ions to the atoms in irradiated material via mostly non-elastic nuclear stopping. The irradiation using heavier ions causes the GO amorphization connected with disruption of the carbon bonds, with atom displacements, and also creation of new non-benzene carbon structures and vacancy types of defects. Contrary, irradiation using light ions (He, H), with dominant elastic electronic stopping, results in lower degree of GO deoxygenation and less pronounced structural changes when comparing with ions with higher mass. Moreover, the light ions irradiation leads to the formation of sp^2 graphene domains.

The irradiation with heavy as well as light ion species reduces the oxygen chemical bonds, generates new carbon bonds and causes the conductivity enhancement that is in accordance with observed compositional and structural modifications. The recovery of electrical conductivity is more pronounced for the light ions due the restoration of graphene like structure and can be concluded that GO irradiation using light ions provides relatively simple method of producing reduced graphene oxide with enhanced electrical conductivity.

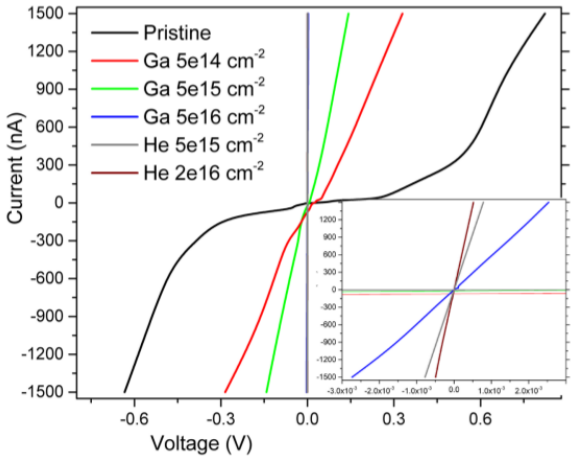

Figure 2: The I–V characteristic curves of pristine GO film and GO film irradiated with 500 keV He and Ga ions at various fluencies. The detailed I–Vcharacteristic for voltage range from $3.0x10^{-3}$ to $3.0x10^{-3}$ V is shown in inset figure

[1] P. Gulia, et all., AIP Conf. Proc. 2017, 1832, 140023.
[2] D. R. Dreyer, et all., Chem. Soc. Rev. 2010, 39, 228.
[3] V. Mazánek,et all., Nanoscale 2015, 7, 13646.
[4] O. C. Compton, Small 2010, 6, 11.
[5] S. Park, Carbon 2009, 50, 217.
[6] Ch. Punckt, et all., Appl. Phys. Lett. 2013, 102, 023114.

Residual stress measurement in rotary swaged composites

Neutron Physics Laboratory - Neutron diffraction

Lenka Kuncicka

Proposal ID

353

Final report to the proposal „Residual stress measurement in rotary swaged composites “

L. Kunčická, Regional Materials Science and Technology Centre, VŠB TU Ostrava, CZ

P. Strunz, Ch. Hervoches Nuclear Physics Institute, ASCR, Řež 130, Husinec, CZ

The aim of this project was to investigate possible presence of residual stress in composite materials rotary swaged under various processing conditions.

In order to determine residual stresses, the strains were calculated according to peak positions in three measured directions, hoop (x), radial (y), and axial (z). The peak position changes in the axial direction were rather smooth within the whole measured range for both the samples. However, the hoop and radial directions peak positions changed significantly in several locations throughout the scanned area. These changes point to the presence of residual stresses in the vicinity of the Al-Cu interfaces.

Calculations of strains according to Eq. (1) [1] showed lattice expansion through the majority of sample cross section in the axial direction, and lattice shrinkage through the majority of sample cross section in the radial and hoop directions for both.

$$\varepsilon_{hkl} = \frac{d_{hkl} - d_{0,hkl}}{d_{0,hkl}} = \frac{\Delta d_{hkl}}{d_{0,hkl}} \tag{1}$$

The final residual stress values calculated according to Eq. (2) [1] are depicted in the dependence in Fig. 1. As can be seen in the Figure, the values of the residual stress for the 10 mm sample oscillated from approx. 150 MPa to -150 MPa along its cross-section. The lowest variations (variation range of 43) were measured in the axial direction, which was perpendicular to the axis of the swaged composite. On the other hand, the step changes in the values in the radial and hoop directions (variation ranges of 65 and 76, respectively) point to residual stress at the Al/Cu interfaces.

$$\sigma_x = \frac{E_{hkl}}{(1-2\nu_{hkl})(1+\nu_{hkl})}\left[(1+\nu_{hkl})\varepsilon_x^{hkl} + \nu_{hkl}(\varepsilon_y^{hkl} + \varepsilon_z^{hkl})\right] \tag{2}$$

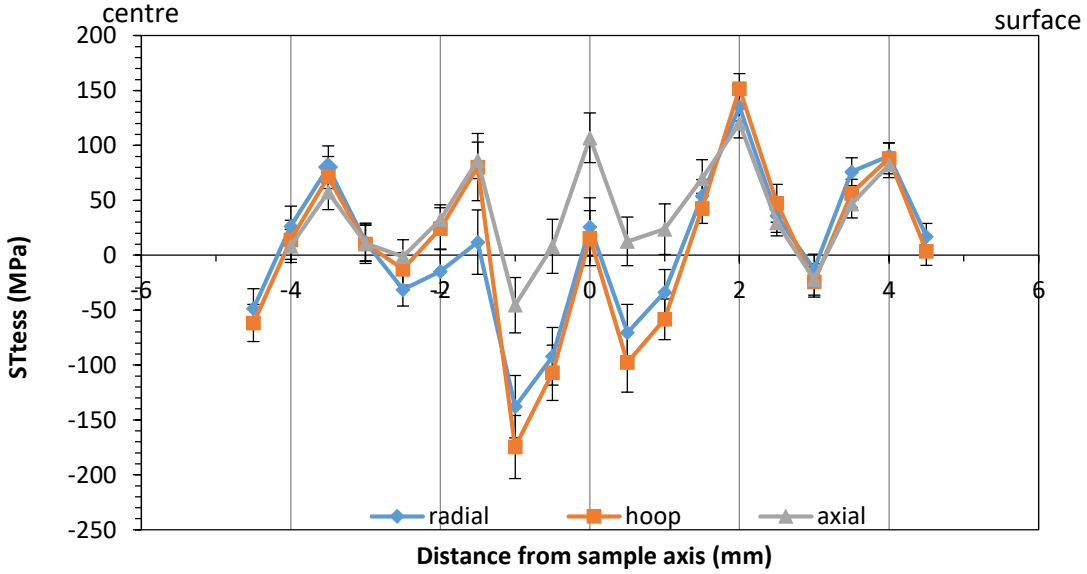

Figure 1. Residual stress within rotary swaged Al-Cu composite, 10 mm diameter.

References

[1] M.T. Hutchings, Introduction to the characterization of residual stress by neutron diffraction, Taylor & Francis, 2005.

Structural and optical properties in yttria-stabilized zirconia modified by Si-implanted ions

Laboratory of Tandetron

Romana Mikšová

Proposal ID

357

Report regarding proposal "Structural and optical properties in yttria-stabilized zirconia modified by Si-implanted ions."

R. Mikšová, A. Macková, A. Jagerová, P. Malinský, Nucl. Physics Inst., Rez, Czech Republic
Z. Sofer, Department of Inorganic Chemistry, Institute of Chemical Technology, Prague, Czech Republic
V. Holý, Department of Condensed Matter, Faculty of Mathematics and Physics, Prague, Czech Republic
CEITEC at Masaryk University, Brno, Czech Republic

In our results, we observed Zr signal increase in the appropriate depth of Si implanted in yttria-stabilized zirconia (YSZ) with the enhanced ion fluence in Figure 1a simultaneously with the shift of the damaged region closer to the surface. YSZ implanted with medium-energy heavy ions exhibits the accumulation of damage with the increasing ion implantation fluence (see Figure 1b). The multi-damage step was shown.

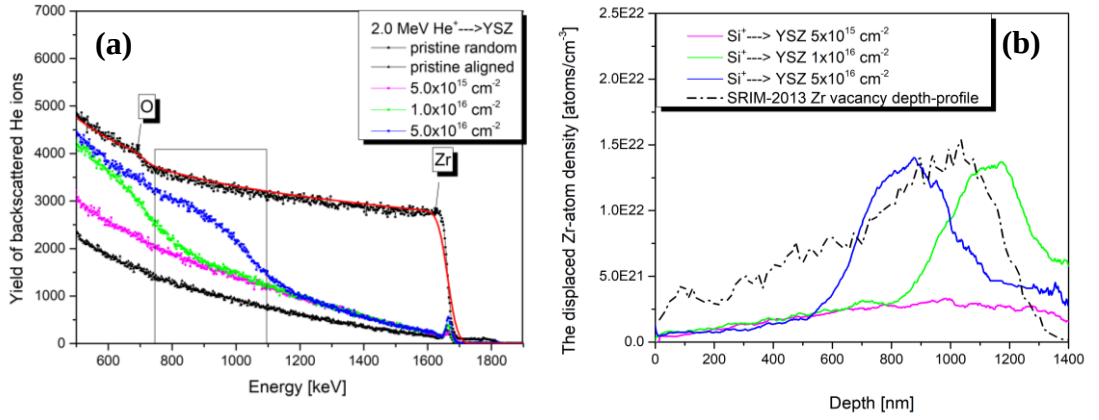

Figure 1. The RBS-C measurement of random and aligned spectra of pristine and implanted YSZ at ion fluence of 5×10^{15}-5×10^{16} cm^{-2} measured by energy 2.0 MeV (a) using He^+ ions. The depth profile of the displaced Zr-atom density in YSZ implanted by 2.0 MeV Si^+ ions at ion fluences of 5×10^{15}-5×10^{16} cm^{-2} extracted from the RBS-C spectra (b).

The XRD measurement indicates specific features as the positive vertical strain which is induced by the interstitial-type defects during ion implantation; the damaged layer is vertically expanded (Figure 2b). These facts agree with the RBS-C measurement where the axial-channel narrowing as a function of the increased ion-implantation fluence was observed. The axial-channel narrowing is a consequence of the gradually enhanced vertical expansion in YSZ (Figure 2a). The Raman spectroscopy confirms changes in the Raman spectra (peak broadening and peak shift) connected with the presence of the strain.

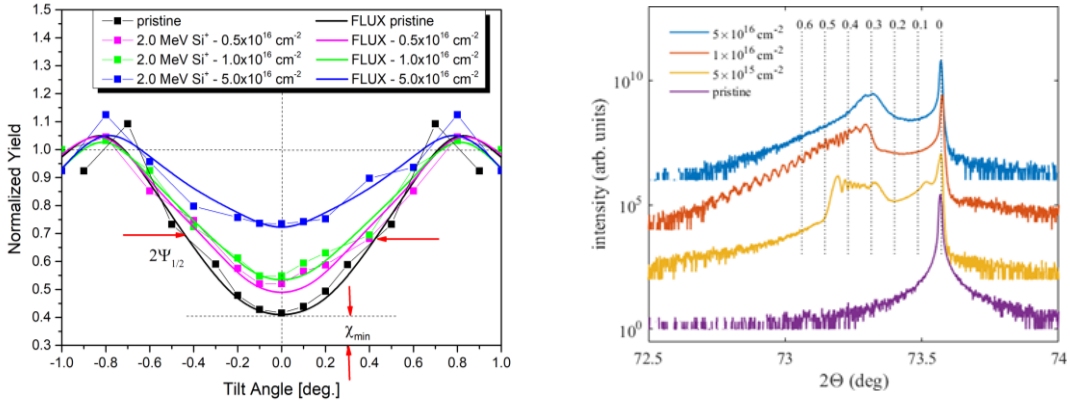

Figure 2. The angular (Zr sublattice) scans using 2.0 MeV He^+ ions penetrating (100) YSZ implanted with 2 MeV Si^+ ions at the fluences of 5×10^{15}-5×10^{16} cm^{-2}. Measured symmetric 2 Θ/Ω scans of a pristine sample and samples implanted with various doses (parameter of the curves).

The results were sent into NIMB.

Neutron scattering studies of nanostructured cemented carbides

Neutron Physics Laboratory - Neutron diffraction

Ahmet Bahadir Yildiz

Proposal ID

358

Experimental report

Proposal: Neutron scattering studies of nanostructured cemented carbides (ID: 358)

Ahmet Bahadir Yildiz, Peter Hedström: KTH Royal Institute of Technology, Stockholm

Vasyl Ryukhtin: Nuclear Physics Institute, Rez

Fine-grained cemented carbides are demanded in cutting applications requiring higher hardness. During our beamtime on the MAUD, we performed ex-situ V-SANS experiments for the investigation of WC grain growth in WC-Co-V_x system as a function of V addition.

V-SANS data were acquired at three different instrumental resolutions. To eliminate the magnetic scattering contribution, specimens were placed between two Neodymium magnets perpendicular to the neutron beam. The measured V-SANS data were corrected for electronic noise background using Cd, normalized by the transmission and scaled to absolute units dΣ/dΩ [cm^{-1}].

Fig. 1 shows the evolution of nuclear V-SANS intensities as a function of V addition. Upon V addition, the scattering intensity decreased at low-Q region, and increased at high-Q region. This development trend in scattering curves gave initial insight to the refinement in WC grain size. In order to calculate radius of gyration, R_g, we used Beaucage model [1] (solid lines in Fig. 1) and Kratky representation [2] (**Fig. 2**), i.e. dΣ/dΩ×Q^2 versus Q plots. Assuming spherical WC grains, the size of WC grains, D_{WC}, can be calculated by: $D_{WC} = 2 * \sqrt{\frac{5}{3}} R_g$

Fig. 3 shows the size evolution of WC grains together with the average grain size measured by EBSD. Consistency in the evolution trend was found in the grain size values determined by V-SANS and EBSD. Kratky plots gave significantly smaller D_{WC} than that of Beaucage model fit. Good agreement was found between D_{WC} values calculated by EBSD and V-SANS using Beaucage model and spherical grain assumption. Currently, we are working on a manuscript.

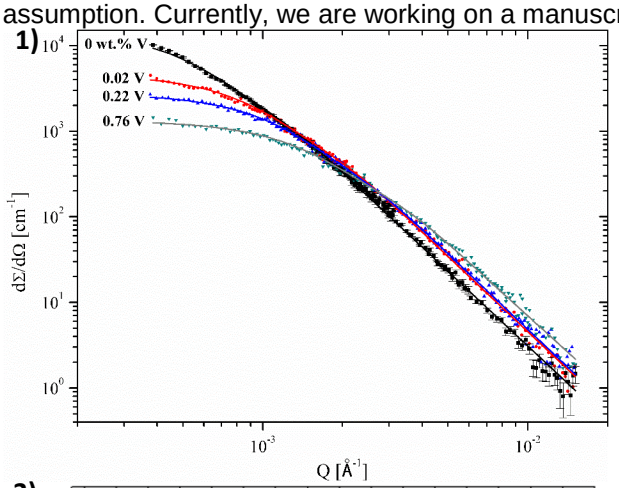

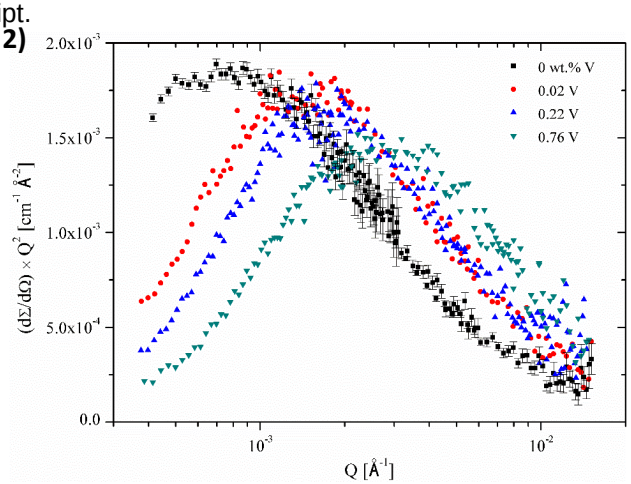

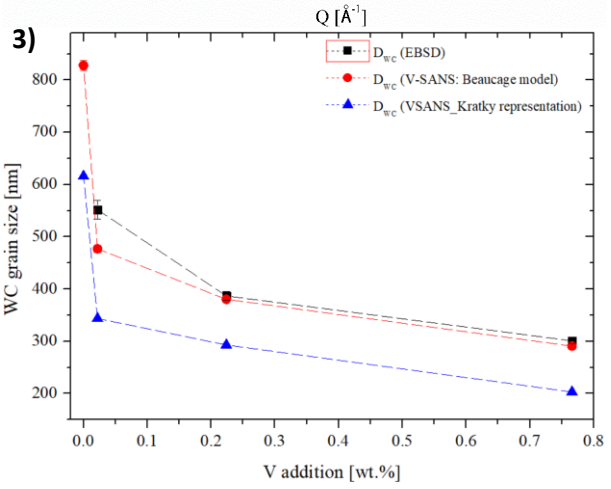

Figures The evolution of V-SANS curves log-log scale **(1)** and Kratky plots **(2)** as a function of V addition in liquid-phase sintered WC-Co-Vx (x=0 to 0.765 wt.% V) cemented carbides. The solid lines in Fig. 1 correspond to Beaucage model fit. The average WC grain size calculated for spherical WC grains plotted together with EBSD results **(3)**.

References

[1] G. Beaucage, J. Appl. Crystallogr. 28 (n.d.) 717–728.

[2] A. Deschamps, F. De Geuser, J. Appl. Crystallogr. 44 (2011) 343–352.

Optical devices by focused MeV ions

Laboratory of Tandetron

István Rajta

Proposal ID

231

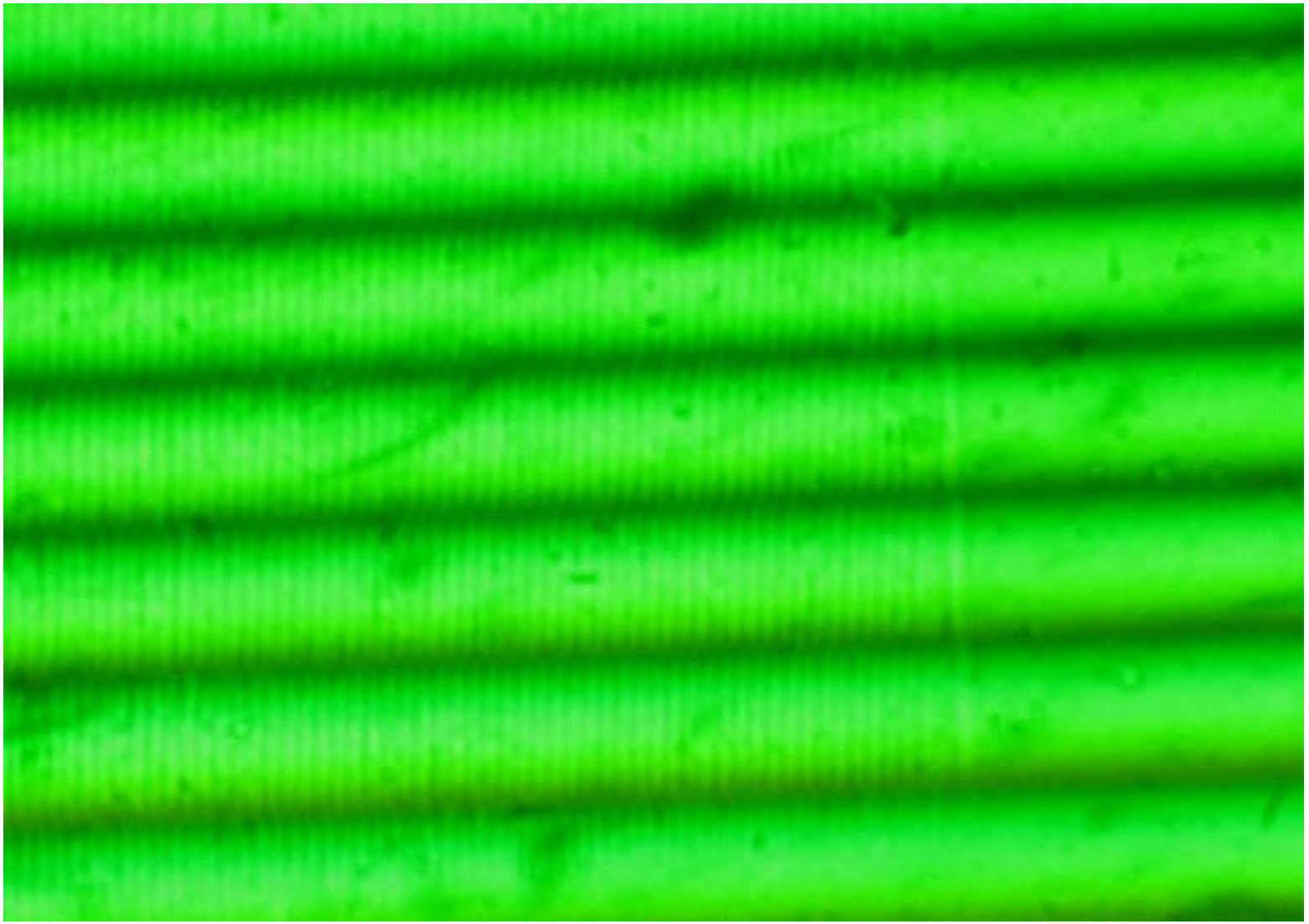

Figure 1. *Transmission interference microscopic image of a grating with $\Lambda = 8\ \mu m$, written by a 5 MeV N^{4+} microbeam at a fluence of 5×10^{15} ions/cm^2 in an Er:$LiNbO_3$ crystal.*

Simulation of alpha radiation-induced alterations in uraniferous fossil organic matter.

Laboratory of Tandetron

Vladimir Strunga

Proposal ID

360

Report regarding proposal "Simulation of alpha radiation-induced alterations in uraniferous fossil organic matter"

V. Strunga, V. Havránek, J. Mizera, Nucl. Physics Inst., Rez, Czech Republic
V. Goliáš, Inst. of Geochem., Mineral. and Min. Res., Charles University, Prague.

Polished sections of Baltic amber were prepared in two series of three samples each. Irradiation was carried on Tandetron accelerator at Nuclear Physics Institute, ASCR, Řež using a 4.8 MeV alpha-particle beam at three various doses, 5E13, 2E14, and 8E14 α/cm2, respectively. Samples were subjected to IR microspectroscopy (ATR-FTIR) afterward.

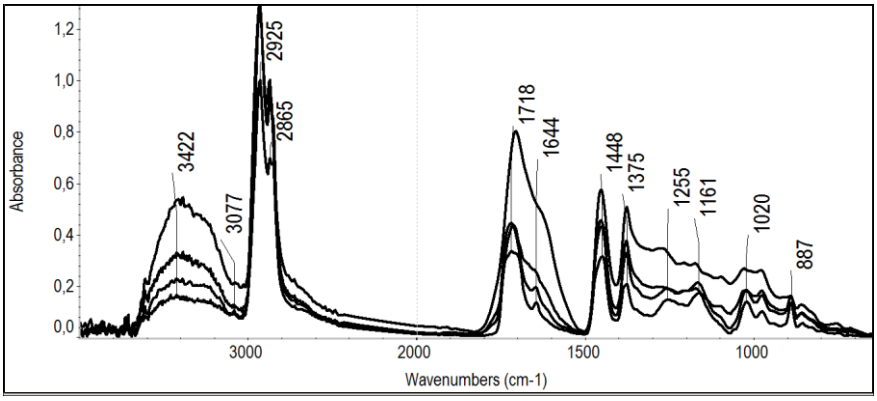

Fig. 1 Infrared spectra of analyzed ambers including non-irradiated sample (analysis by Vladimír Machovič).

Spectra exhibit broadening of O-H band at 3422 cm^{-1} as well as a decrease in double bond band intensities at 3100-3000, 1644 and 887 cm^{-1}. There is also distinguishable vanishing of the Baltic amber characteristic feature, so-called 'Baltic shoulder' assigned to the absorption of succinic acid ester bonds of polyester-like structures between 1255 and 1161 cm^{-1}.

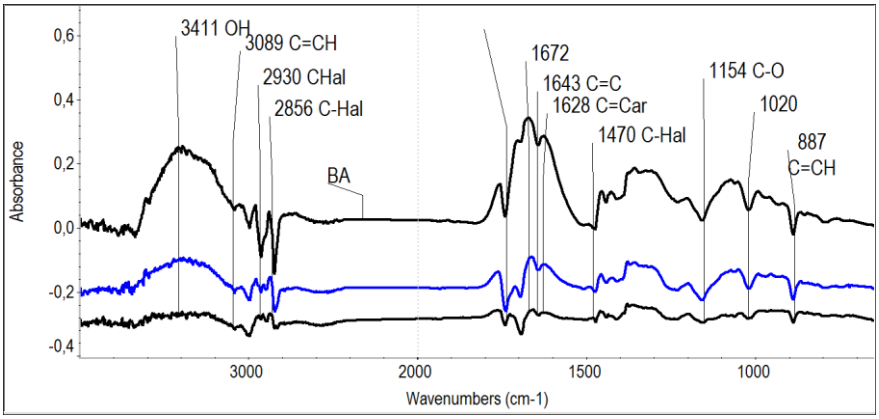

Fig. 2 Differential spectra obtained by subtraction of non-irradiated sample spectral values from irradiated ones (analysis by Vladimír Machovič).

Differential spectra reveal a considerable decrease of C-H band intensities at 2930, 2856, 1470 cm^{-1}, O-H band intensity increase at 3411 cm^{-1}, 1705 cm^{-1}, COOH band at 1672 cm^{-1}, highly conjugated C=O and aromatic C=C band at 1628 cm^{-1}.

Reference

Havelcová, M., Machovič, V., Linhartová, M. Lapčák, L., Přichystal, A., Dvořák, Z. (2016)
Vibrational spectroscopy with chromatographic methods in molecular analyses of Moravian amber samples (Czech Republic). Microchemical Journal, 128, 153-160.

Nanoscale investigation by USANS of Co-Cr alloy samples for the biomedical sector

Neutron Physics Laboratory - Neutron diffraction

Massimo Rogante

Proposal ID

364

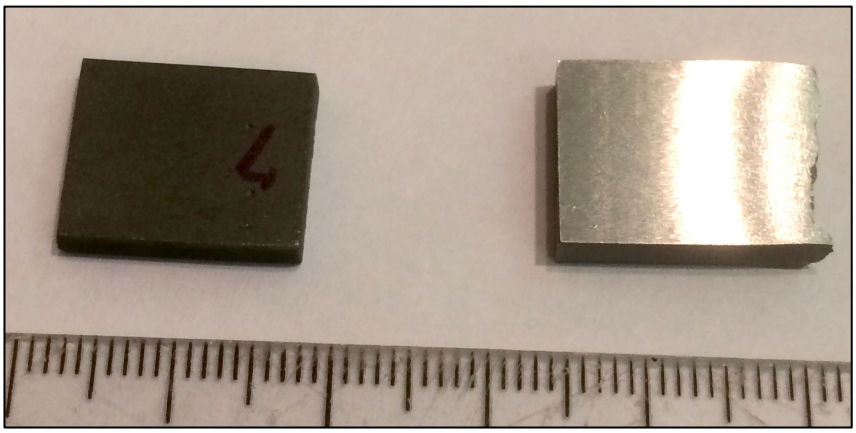

Fig. 1. Co–Cr alloy samples produced by DMLS: as-sintered state (right), after post-production thermal stress relieving treatment (left).

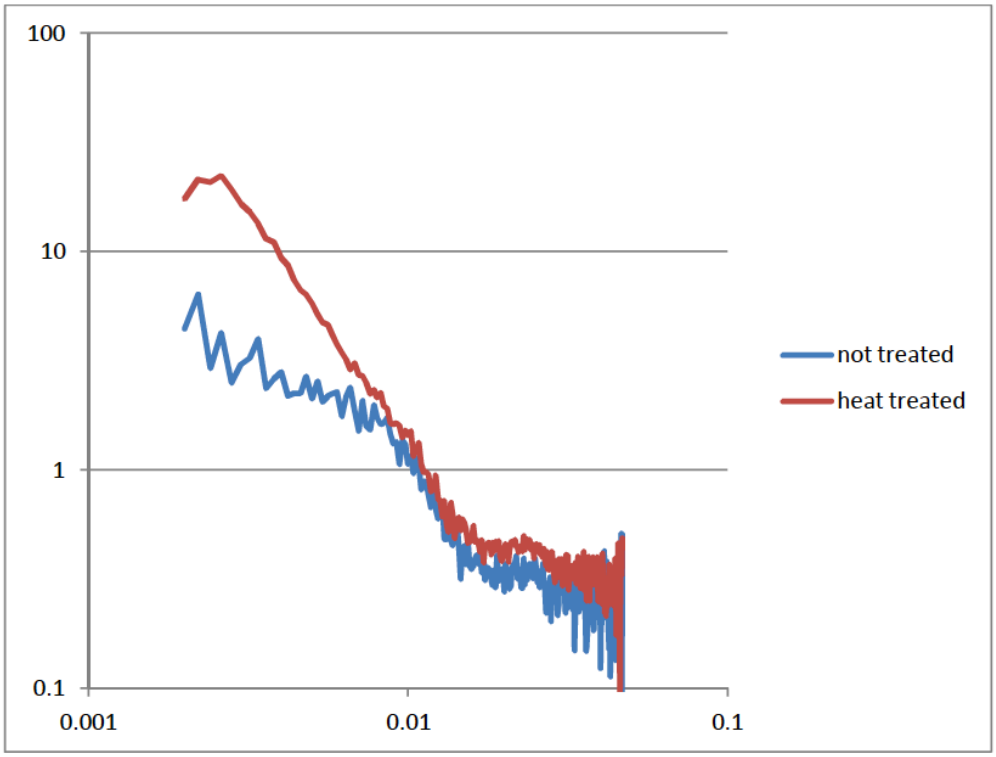

Fig. 2. Sigma (Q) curves related to a preliminary feasibility SANS analysis of the samples of Fig. 1.

References

[1] G. Barucca, E. Santecchia, G. Majni, E. Girardin, E. Bassoli, L. Denti, A. Gatto, L. Iuliano, T. Moskalewicz, P. Mengucci, Structural characterization of biomedical Co–Cr–Mo components produced by direct metal laser sintering, Materials Science and Engineering C 48 (2015), pp. 263–269.

[2] P. Mengucci, G. Barucca, A. Gatto, E. Bassoli, L. Denti, F. Fiori, E. Girardin, P. Bastianoni, B. Rutkowski, A. Czyrska-Filemonowicz, Effects of thermal treatments on microstructure and mechanical properties of a Co–Cr–Mo–W biomedical alloy produced by laser sintering, Journal of the Mechanical Behavior of Biomedical Materials, Vol. 60 (2016), pp. 106-117.

[3] E. Girardin, G. Barucca, P. Mengucci, F. Fiori, E. Bassoli, A. Gatto, L. Iuliano, B. Rutkowski, Biomedical Co-Cr-Mo components produced by Direct Metal Laser Sintering, Materials Today: Proceedings 3 (2016), pp. 889-897.

Radiation Hardness of Si Pixel Chips and Components for ALICE Inner Tracker System Upgrade Project

Laboratory of Cyclotron and Fast Neutron Generators

Filip Krizek

Proposal ID

365

Radiation Hardness of Si Pixel Chips and Components for ALICE Inner Tracker System Upgrade Project

In the CANAM 365 project, we tested radiation hardness of monolithic active pixel sensors which are going to be used in the upgraded Inner Tracking System (ITS) of the ALICE experiment. The sensors are called ALPIDEs and their radiation hardness was probed using a 30 MeV proton beam provided by the U-120M cyclotron. According to the Conceptual Design Report of the ITS project, the ALPIDE sensors must withstand 2.7 Mrad of Total ionization dose (TID) and 1.7 x 10^13 1 MeV n_eq/cm^2 of Nonionizing energy loss (NIEL) throughout the whole lifetime of the detector. Therefore in 2018, we continued in irradiations of two ALPIDE sensors which in previous years accumulated 1.8 Mrad and 1.4 Mrad TID and 1.8x10^13 and 1.4x10^13 1 MeV n_eq/cm^2 NIEL, respectively. Both ALPIDEs were irradiated on 12.1., 12.2., 28.3, 19.4, 17.5., 20.6., 16.7. and 10.10. At the end of the year, the chips accumulated 2.8 Mrad and 2.3 Mrad TID and 2.8x10^13 and 2.3x10^13 1 MeV n_eq/cm^2 NIEL, respectively. For both chips, we studied a mean charge threshold for signal detection in pixels and a mean temporal noise as a function of the accumulated TID. After retuning of the charge threshold in November 2017, both chips continue to exhibit significant annealing of their threshold levels after irradiations. The mean temporal noise, however, continues to grow and annealing shows a minor effect.

The interim results from these measurements were reported on several ITS upgrade characterization meetings, ALPIDE Qualification Task Force meetings (Work Package 5) on 24.1, 25.4. and 25.7.

The chip that got 2.8 Mrad was further brought to CERN where it was characterized using a 6 GeV/c pion beam from the CERN PS. The chip was characterized in terms of detection efficiency and fake hit rate. Important outcome from these measurements is that the highly irradiated sensor still meets requirements of the technical design report. Results from this measurement were presented at two international conferences:

[1] S. Kushpil et al. (ALICE collaboration), "Recent results from beam tests of the ALPIDE pixel chip for the upgrade of the ALICE Inner Tracker", 2018 IEEE Nuclear Science Symposium and Medical Imaging Conference, 10-17.11.2018, Sydney Australia.

[2] Valentina Raskina et al. (ALICE collaboration): "Characterization of silicon sensors for ALICE ITS upgrade", 18th Zimányi school and worshop, 3.-7.12. Budapest, Hungary.

A detailed description of the methodology of our measurements and of our irradiation setup that is being used for the tests of radiation hardness at the U-120M cyclotron facility were published in two papers:

[3] F. Křížek et al., Irradiation setup at the U-120M cyclotron facility, Nucl Instr. Meth. Phys. Res. A 894 (2018) 87-95.

[4] T. Matlocha and F. Křížek, Ultra-low intensity proton beams for radiation response related experiments at the U-120M cyclotron, Acta Polytechnica CTU Proceedings 14 (2018) 21-26.

Rb-83 for calibrations in the KATRIN continuing experiment

Laboratory of Cyclotron and Fast Neutron Generators

Drahoslav Venos

Proposal ID

366

Final report regarding proposal 366:

Rb-83 for calibration in the KATRIN, continuing experiment

D. Vénos

In the period 3.1.2018 - 20.12.2019 we have produced 83Rb in 5 irradiations at the cyclotron U-120M (the achieved activities of 340, 1500, 130, 1500 and 200 MBq) and in 1 irradiation at the cyclotron TR24 (the activity of 1600 MBq) using gas target filled with the natural krypton. For the irradiation at TR24 a newly designed gas target was used. The production rate at TR4, of 130 MBq of 83Rb per one hour irradiation time, was by a factor of 2.6 larger (mainly due to the larger current of the bombarding protons) in comparison with U-120M which has allowed us to reduce the irradiation time significantly.

From the 83Rb activities were prepared for the KATRIN project a 3 types of the 83Rb/83mKr sources of the monoenergetic electrons. The 2 sources were produced in NPI by vacuum evaporation of the 83Rb onto the amorphous graphite and Highly Oriented Pyrolytic Graphite (HOPG) substrates, respectively. Both these sources were transported to the Max Planck Institute for Physics (München). The sources were used for the test of the detector which is newly developed for KATRIN. Further, the 83Rb activity (deposited in the mass-separator tungsten furnace) was sent 2 times to Bonn University where altogether 4 83Rb/83mKr sources were prepared by the implantation of the 83Rb ions into the HOPG substrate. The 3 sources were installed at the Monitor Spectrometer which has watched the stability of the KATRIN High Voltage. One implanted source was installed at the Condensed Krypton Source (constructed at the Muenster University) which was used for the systematic measurement at the KATRIN. The main portions of the produced activity, 3 times of ~ 1.2 GBq of 83Rb, were deposited in the NPI into the zeolite beads. These 3 sources were regularly transported to KATRIN and installed into the Gaseous Krypton Source attached to the Windowless Gaseous Tritium Source (WGTS). The sources were used for the systematic studies of the WGTS plasma which has direct influence on the tritium beta spectra measured at KATRIN and subsequently on the deduced neutrino mass.

In the period 2018-2019 the KATRIN has started with the measurements of the neutrino mass gradually increasing the amount of the tritium in the WGTS. The first KATRIN limit on the neutrino mass, by factor of 2 better in comparison with the previous many years measurements, was obtained after 20 measurement days only. The result was published in the journal Physical Review Letters.

Articles in journals related to the use of Rb-83:

1) O. Dragoun, D. Vénos, ČS. Čas. Fyz. 69(2019)318, (in Czech).
2) M. Aker, K. Altenmüller, ... O. Dragoun, A. Kovalík, O. Lebeda, M. Ryšavý, D. Vénos, ... (KATRIN coll.), Phys. Rev. Lett. 123, 221802 (2019).
3) M. Aker, K. Altenmüller, ... O. Dragoun, A. Kovalík, O. Lebeda, M. Ryšavý, D. Vénos, ... (KATRIN coll.), arXiv:1909.06069v1 13 Sep 2019, submitted to Eur. Phys. J.
4) K. Altenmüller, M. Arenz, ... O. Dragoun, A. Kovalík, O. Lebeda, M. Ryšavý, D. Vénos, ... (KATRIN coll.), arXiv:1903.06452v2 18 Mar 2019.
5) A. Kovalík, A.Kh. Inoyatov, D. Vénos, M. Zbořil, O. Dragoun, D.V. Filosofov, L.L. Perevoshchikov, M. Ryšavý, Physics of Particles and Nuclei, 2019, Vol. 50 No. 6.
6) D. Vénos, J. Sentkerestiová, O. Dragoun, M. Slezák, M. Ryšavý, A. Špalek, 2018 JINST 13 T02012.
7) J. Sentkerestiová, O. Dragoun, O. Lebeda, M. Ryšavý, M. Sturm, D. Vénos, 2018 JINST 13 P04018.
8) M. Arenz, W.J. Baek, … O. Dragoun, A. Kovalík, O. Lebeda, M. Ryšavý, M. Slezák, M. Suchopár, J. Sentkerestiová, D. Vénos … (KATRIN coll.), 2018 JINST 13 P04020.
9) M. Arenz, W.J. Baek, … O. Dragoun, A. Kovalík, O. Lebeda, M. Ryšavý, M. Slezák, M. Suchopár, J. Sentkerestiová, D. Vénos … (KATRIN coll.), Eur. Phys. J. C (2018) 78:368.

Cross-section measurements of the 16O(n,tot) reaction in the neutron energy range 20-35 MeV

Laboratory of Cyclotron and Fast Neutron Generators

Mitja Majerle

Proposal ID

368

Final report regarding proposal 'Cross-section measurements of the ^{16}O(n,tot) reaction in the neutron energy range 20-35 MeV'

The series of transmission experiments with liquid oxygen was performed using Quasi-monoenergetic collimated beams of neutrons produced at U-120M cyclotron. The absolute values of the cross-section ^{nat}O(n,tot) were successfully extracted for four different energies ranging from 18 to 30 MeV. Overall uncertainties were evaluated for each measurement and regarding one sigma interval derived for normal distribution, the precision better than 3 % was achieved.

Exact results were presented at '2019 International Conference on Nuclear Data for Science and Technology' and subsequent paper named 'Total neutron cross-section extracted from transmission experiments with liquid oxygen using neutron energies from 18 to 34 MeV' is about to be published under 'EPJ Web of Conferences' in 2020.

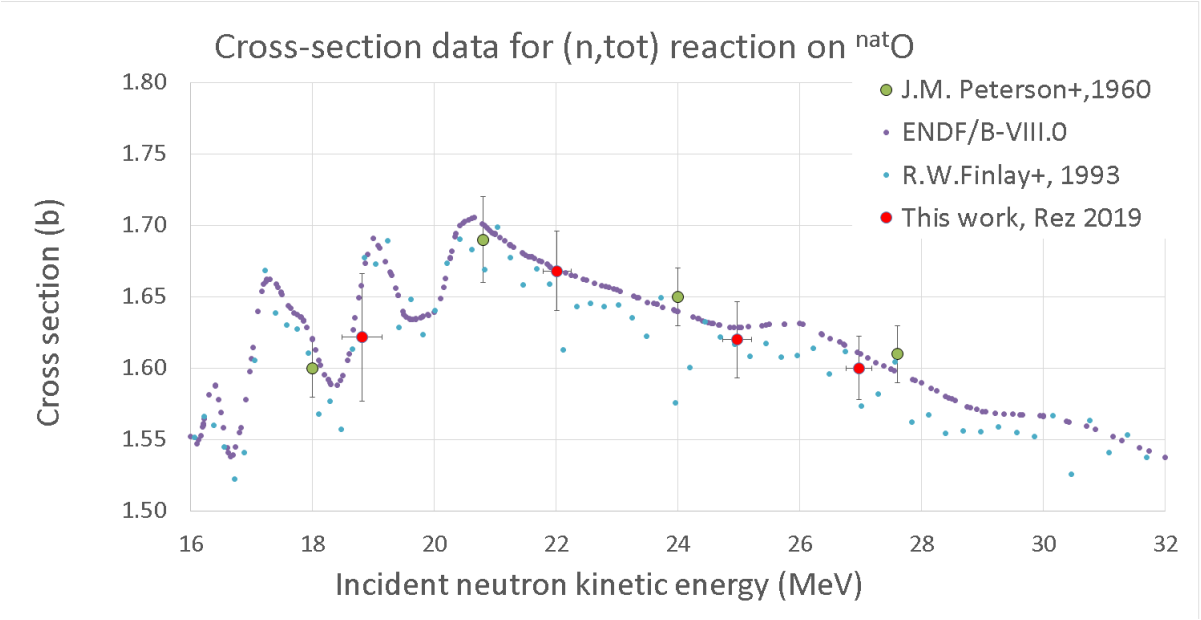

Figure 1. Present data of total neutron cross-section for ^{nat}O are shown (red points). For comparison data of Peterson [1] and Finlay [2] together with ENDF/B-VIII.0 evaluation for 16O(n, tot) reaction [3] are shown.

Present results (figure 1) should improve the correctness of data evaluations and contribute to all projects and researches where cross-section ^{nat}O(n,tot) is not a negligible factor. The Accelerator Driven Systems (ADS) and future fusion-based facilities are relevant examples.

References:

[1] J.M. Peterson, A. Bratenahl, J.P. Stoering, Phys. Rev.120, 521 (1960)

[2] R.W. Finlay et al., Neutron Total Cross Section Measurements at Intermediate Energy, in Nuclear Data for Science and Technology (1992), pp. 720–722, ISBN 978-3-642-58113-7

[3] D. Brown et al., Nuclear Data Sheets 148, 1 (2018), special Issue on Nuclear Reaction Data

Reactions of organometallic complexes relevant for the ion beam cancer therapy

Laboratory of Cyclotron and Fast Neutron Generators

Marie Davidkova

Proposal ID

370

Report regarding proposal "Reactions of organometallic complexes relevant for the ion beam cancer therapy"

J. Kočiček, D. Reimitz, Institute of Physical Chemistry of the CAS, Prague, Czech Republic
M. Davídková, Nuclear Physics Institute of the CAS, Řež, Czech Republic

An important challenge of radiation oncology is reduction of the side effects of the treatment. Such reduction can be achieved by effective targeting of tumors by radiation using the novel ion beam techniques or by lowering the dose delivered in concomitant chemo-radiotherapy. The main advantage of such treatments is in the so-called synergistic effect, which is the enhancement of the damage delivered to the tumor over the effect of the individual chemotherapy and radiotherapy treatments.
Experimental study is exploring combined effect of organometallic compounds and ionizing radiation. Performed experiments have been focused to cisdiamminedichloridoplatinum(II) (cisP or CDDP). When irradiating plasmid DNA in solution with free molecules by ^{60}Co gamma rays, no combined effect has been observed, indicating that the contribution to DNA damage caused by products of CDDP radiolysis is negligible in comparison to the damage caused by products of radiolysis of water. After binding to DNA, CDDP adducts with DNA strongly enhance the damage in a good agreement with the results of previous studies.
To reveal potential enhancement of DNA damage induction by radiation of different quality, Tris solutions containing pBR322 plasmids have been irradiated by 30 MeV protons. Different conformations of DNA plasmid corresponding to induced DNA single and double strand breaks have been analyzed using agarose gel electrophoresis. Relative proportion of relaxed form of pBR322 corresponding to single strand break yields as a function of absorbed dose is presented in Figure 1. No modifications of DNA damage induction have been detected in samples containing cisdiamminedichloridoplatinum(II) either for low (5 mM Tris) or high (200 mM Tris) radical scavenging conditions.

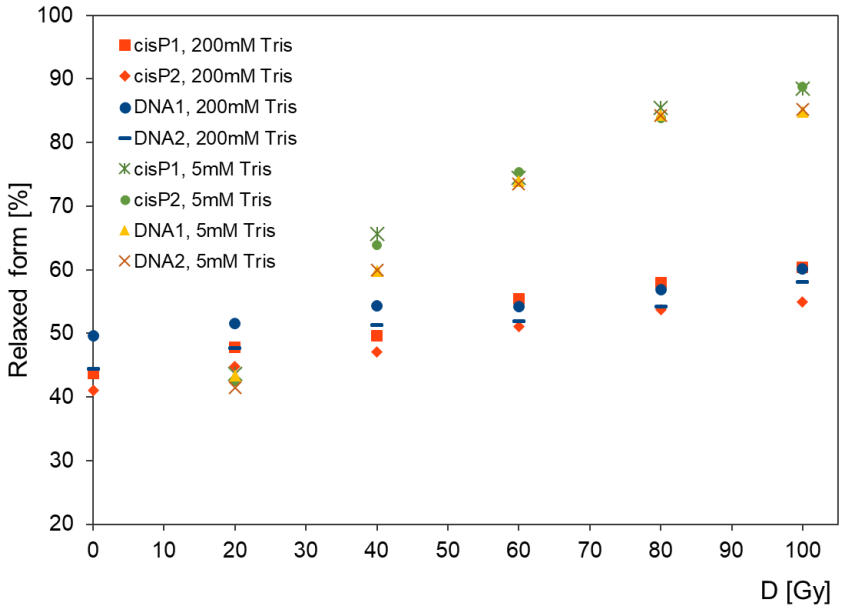

Figure 1: Proportion of relaxed form of pBR322 DNA plasmid irradiated by 30 MeV protons in presence or in absence of cisdiamminedichloridoplatinum(II) (cisP).

The work was supported by the Czech Science Foundation grant no. 16-10995Y.

Patterning and characterization of graphene oxide foil irradiated by Ion micro beam

Laboratory of Tandetron

Mariapompea Cutroneo

Proposal ID

371

Report

In the present proposal, the ion beam lithography technique has been used to write a line on graphene-oxide foil using the microbeam system and ions produced by a Tandetron accelerator. The depletion/enhancement of the GO components was precisely evaluated by irradiating progressively the foil and monitoring online its structural and compositional changes by RBS analysis (Figure 1).

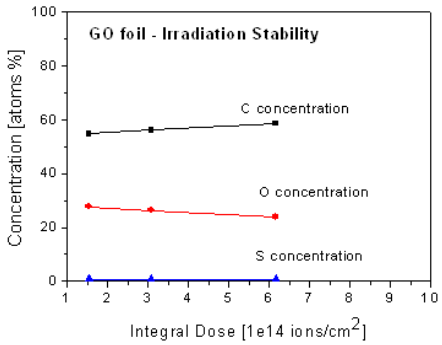

FIGURE 1. Changing of the C, O and S concentrations during the ion irradiation of the GO foils.

The agreement between RBS and SEM-EDX measurements suggests a relation between ion-irradiation fluence and oxygen reduction in GO foil and provides an essential clue that the reduction of GO can be a key factor for mobility enhancement (Figure 2).

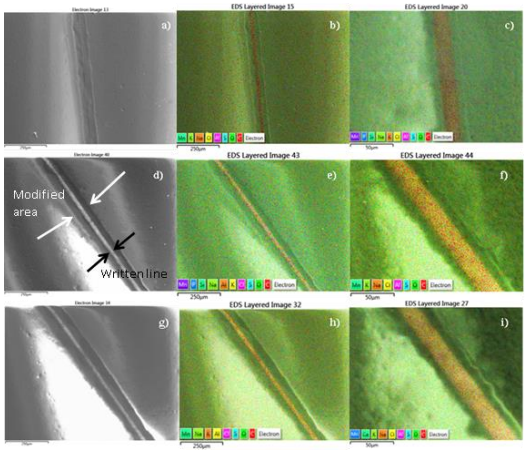

FIGURE 2. SEM images of a written line in GO foil magnified x296 and irradiated at $1.87 \cdot 10^{14}$ ions/cm^2 (a);SEM –EDX maps of the line magnified x1500 after the irradiation by$1.87 \cdot 10^{14}$ ions/cm^2 (b) and $3.75 \cdot 10^{14}$ ions/cm^2 c)

The published results reaffirm the potential of the ion- beam lithography as a promising technique for the processing of large-scale GO foil and the development of micrometric devices such as diodes and Schottky barriers as well as for other application. Further improvement of the quality along with the control of the ion-fluence irradiation to obtain the desired surface functionalisation are important challenges for the materials community but the oxidation/reduction processes need to be more fully understood to create and to tune the band gap in GO by varying the oxygen concentration.

Investigation of novel composite CoNiAl-Ti by neutron diffraction and small-angle neutron scattering

Neutron Physics Laboratory - Neutron diffraction

Pavel Strunz

Proposal ID

245

Report regarding proposal "**Investigation of novel composite CoNiAl-Ti by neutron diffraction**"

Pavel Strunz (email: strunz@ujf.cas.cz, affiliation: Ústav jaderné fyziky AV ČR, v. v. i.),
P. Beran, NPI, Oleg Heczko, IP Prague, CZ, Jaromír Kopeček, IP Prague, CZ, Tomáš Chráska, Institute of Plasma Physics, CZ, Radek Mušálek, Institute of Plasma Physics, CZ, Zdenek Pala, Institute of Plasma Physics, CZ, Josef Stráský, MFF UK Prague, CZ,

Investigation of phase composition and microstructure of composite material CoNiAl-Ti produced by Spark Plasma Sintering was proposed. The properties of the composite are expected to depend strongly on minority phase content and thus on the parameters of preparation of the material. The results complement characterization by other techniques, predominantly electron microscopy and XRD.

Measured samples of CoNiAl plus Ti prepared by SPS:

Sample	T, C	P, Mpa	time,min	CoNiAl:Ti	Ti, %
150713_2	911	5	0	1:1	50
150715_1	950	80	1	1:1	50
150714_1	950	80	5	1:1	50
150909_1	950	80	5	2:1	33.3
150915_1	950	80	1	2:1	33.3
150916_1	950	80	1	1:2	66.7
150916_2	950	80	5	1:2	66.7

An example of measured and evaluated neutron diffraction profile:

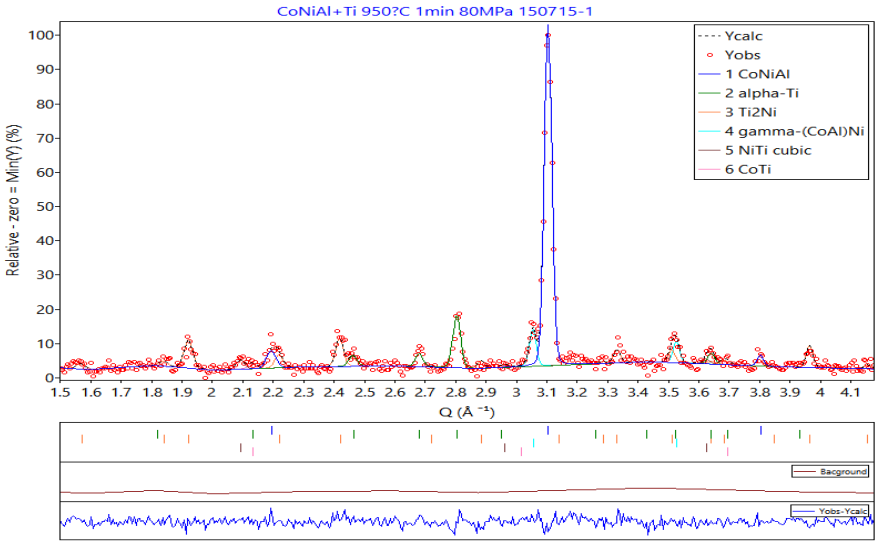

Dependence of phase content
on the mode of sample preparation

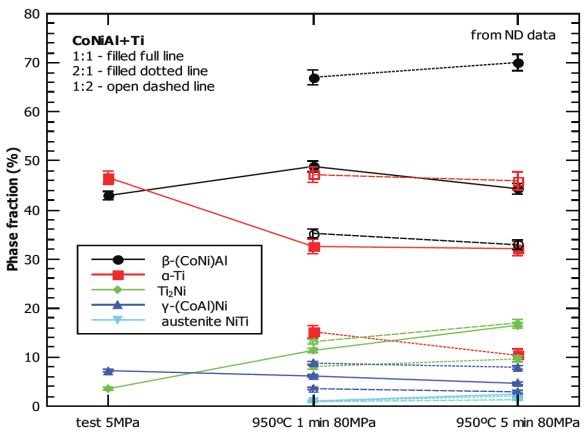

… and on the amount of Ti in the sample:

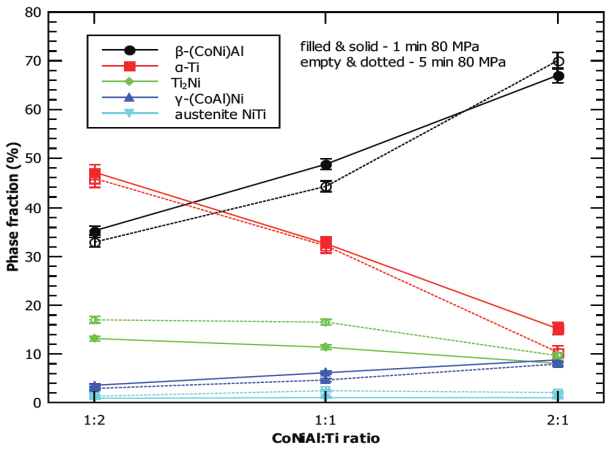

NDP measurements of boron doped diamond for calibration of Glow Discharge OES

Neutron Physics Laboratory - Nuclear analytical methods with neutrons

Andy Taylor

Proposal ID

373

Comparison of analysis of boron doped diamond layers by NDP and GD-OES: preliminary results

Zdenek Weiss[1], Andrew Taylor[1], Vincent Mortet[1] and Jiri Vacik[2]

[1]*Institute of Physics of the Czech Academy of Sciences, Prague, Czech Republic*
[2]*Nuclear Physics Institute of the Czech Academy of Sciences, Řež, Czech Republic*

Two samples of B-doped diamond layers prepared by MW-LA-PECVD and five samples prepared by MW PECVD were analyzed for boron concentration in the diamond layer by NDP (neutron depth profiling) and GD-OES (glow discharge optical emission spectroscopy). Comparison of the resulting composition obtained by NDP and GD-OES is shown in Fig. 1.

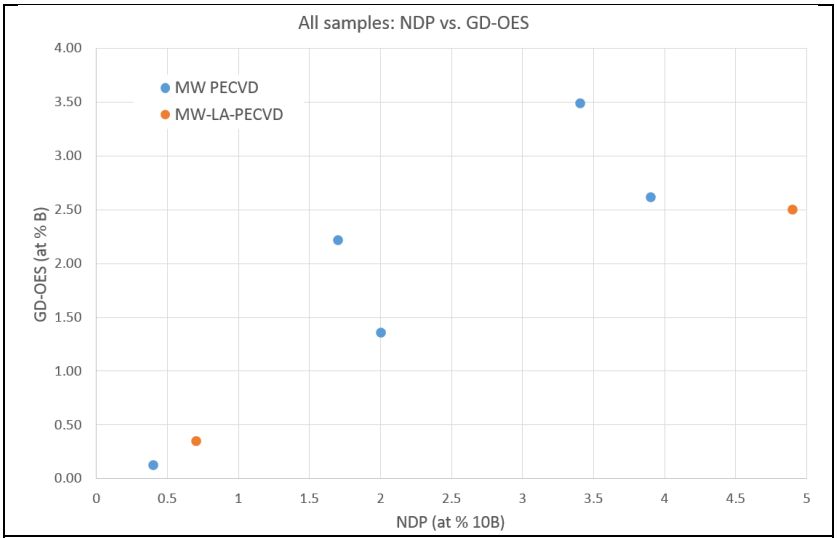

Fig. 1: Correlation between NDP and GD-OES

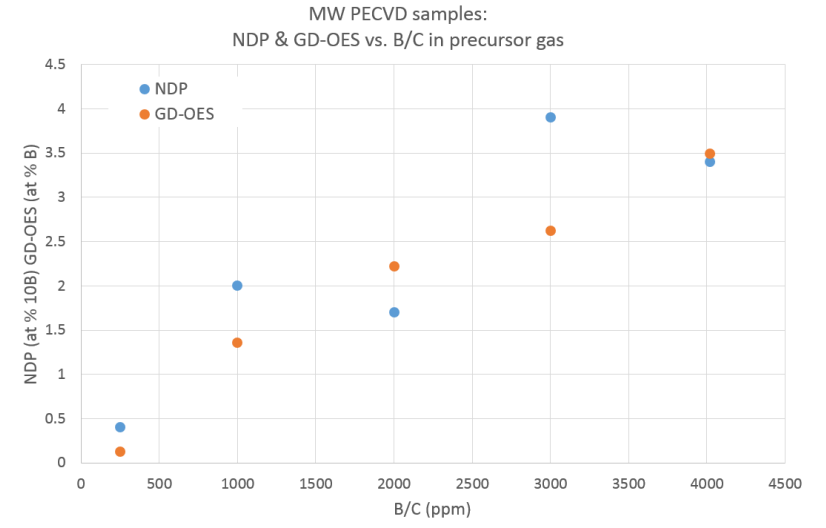

2: Correlation of at % (obtained by NDP and GD-OES) and B/C ratio in gas phase

For MW PECVD samples, the B composition was obtained by both depth profiling method and related to the boron concentration in the precursor gas (B/C), results are displayed in Fig. 2.

Both depth profiling methods give concentrations of boron of a similar magnitude, which is a good sign, as the methods are fundamentally different and thus independent. Correlation betwen B/C and the boron concentration seems to be better for GD-OES than NDP. This should be further studied to identify possible sources of the discrepatcy. This study will be complemented by another set of B composition measurments based on Raman spectroscopy. Also, the interface region beneath the C-layer in these samples will be compared with that in samples prepared at a room temperature, in which no Si-C interdiffusion is expected to occur.

Investigation of novel composite CoNiAl-Ti by small-angle neutron scattering and neutron diffraction

Neutron Physics Laboratory - Neutron diffraction

Pavel Strunz

Proposal ID

246

Report regarding proposal "**Investigation of novel composite CoNiAl-Ti by small-angle neutron scattering and neutron diffraction**"

Pavel Strunz (email: strunz@ujf.cas.cz, affiliation: Ústav jaderné fyziky AV ČR, v. v. i.),
V. Ryukhtin, Oleg Heczko, IP Prague, CZ, Jaromír Kopeček, IP Prague, CZ, Tomáš Chráska, Institute of Plasma Physics, CZ, Radek Mušálek, Institute of Plasma Physics, CZ, Zdenek Pala, Institute of Plasma Physics, CZ, Josef Stráský, MFF UK Prague, CZ,

Investigation of phase composition and microstructure of composite material CoNiAl-Ti produced by Spark Plasma Sintering was proposed. The properties of the composite are expected to depend strongly on minority phase content and thus on the parameters of preparation of the material. The results complement characterization by other techniques, predominantly electron microscopy and XRD.

Measured samples

Sample	T, C	P, Mpa	time,min	CoNiAl:Ti	Ti, %	<R>, nm	dR
150713_2	911	5	0	1:1	50	55.25	0.69
150715_1	950	80	1	1:1	50	70.39	1.2
150714_1	950	80	5	1:1	50	75.73	2.1
150909_1	950	80	5	2:1	33.3	103.9	3
150915_1	950	80	1	2:1	33.3	86.1	1.2
150916_1	950	80	1	1:2	66.7	82.17	1.1
150916_2	950	80	5	1:2	66.7	69.26	1.5

Comparison of SANS between pure CoNiAl and with Ti

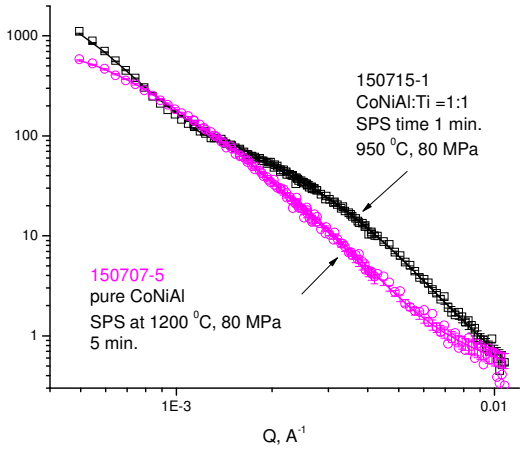

Exmple of SANS from CoNiAl+Ti samples:

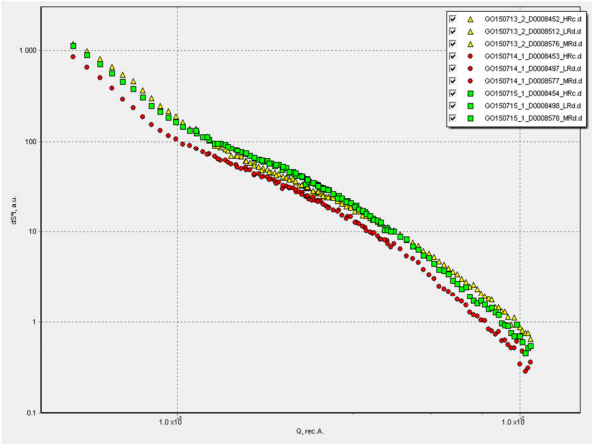

Probable cause of scattering: nanopores. Then, their volume fraction and mean size change according to the following figures:

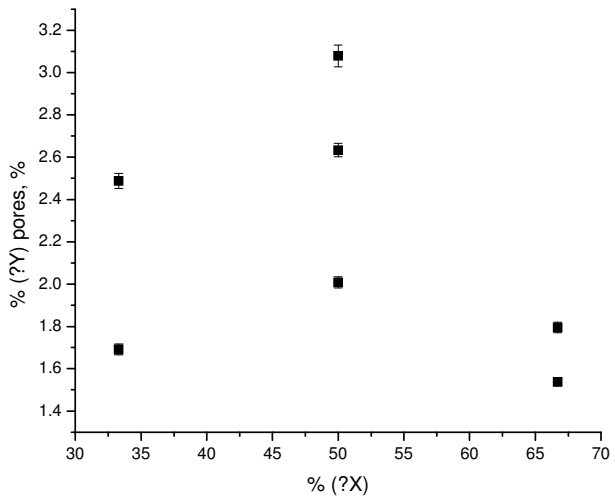

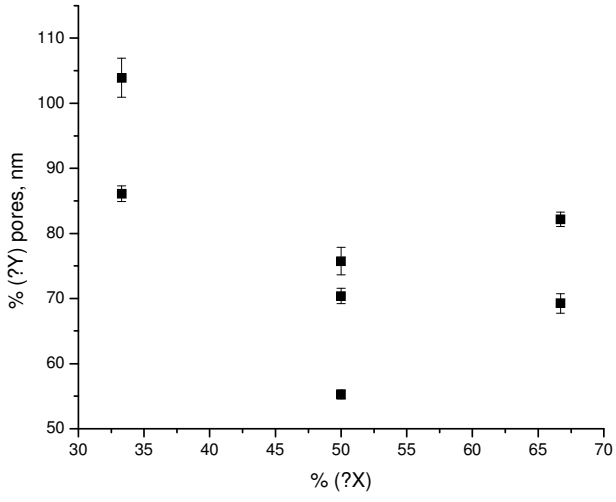

Microstructural investigations of BaTiO3-based ceramics prepared by Sparc Plasma Sintering (AdMat)

Neutron Physics Laboratory - Neutron diffraction

Vasyl Ryukhtin

Proposal ID

249

Microstructural investigations of BaTiO3-based ceramics prepared by Sparc Plasma Sintering (SPS)

Vasyl Ryukhtin, Nuclear Physics Institute NPI (ASCR), Neutron Physics Department

Pavel Ctibor, Institute of Plasma Physics, Prague Czech Republic

A set of BaTiO3-based samples were sintered by SPS at Institute of Plasma Physics (IPP) of ASCR. Spark plasma sintering enables very rapid fabrication of bulk ceramic materials. It is an emerging consolidation technique, which combines pulsed electric currents and uniaxial pressure induced compaction. Heating rates, applied pressures and pulsed current patterns are the main factors responsible for the enhancement of densification kinetics and conservation of the submicron-scale structure of the materials [1]. This material was widely studied at material engineering (ME) department of IPP ASCR as excellent material for plasma spraying (PS).

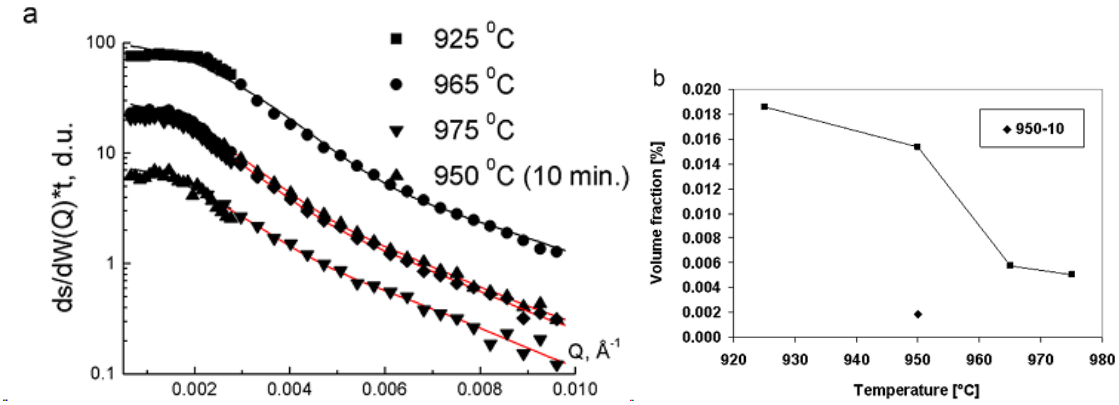

Fig. 1. SANS scattering spectra (a) and fitted volume fractions of pores (b).

The SANS curves were fitted using simple structural model of spherical particles (Fig. 1a) with help of SASprofit software. Although, for some samples scattering data in low angle region were distorted by multiple scattering a part of spectra with high angles were fitted reasonably good. However, because of the multiple scattering, a pore size distribution cannot be specified and only the volume fraction V is representative (Fig. 1b). The results include all pores between 20 nm and 3 mm. Certain trend could be seen (Fig. 1b) – the higher is the sintering temperature, the lower is the porosity. Increasing the dwell time at 950 °C led to further decrease in the porosity volume fraction. For the sample 950-10 the volume fraction is nearly 10 times smaller compare to the most porous sample 925.

Reference

[1] P. Ctibor et al, *Barium titanate nanometric polycrystalline ceramics fired by spark plasma sintering* Ceramics International 42 (2016) 15989–15993.

Texture measurements in composites subjected to severe plastic deformation

Neutron Physics Laboratory - Neutron diffraction

Lenka Kuncicka

Proposal ID

378

Final report to the proposal „Texture measurements in composites subjected to severe plastic deformation“

L. Kunčická, Regional Materials Science and Technology Centre, VŠB TU Ostrava, CZ
P. Beran, P. Strunz, Nuclear Physics Institute, ASCR, Řež 130, Husinec, CZ

The aim of this project was to investigate the influence of various conditions of plastic deformation on texture development in composites with various diameters. According to the results of the measurements.

Figure 1 depicts the inverse pole figures (PFs) of the swaged composite samples acquired in the direction perpendicular to the swaging axis by neutron diffraction. The grains of both the metal components obviously exhibited a strong tendency to form the <111> fibre (Copper texture) and the <001> fibre (Goss texture), the latter of which was primarily observed for Al. Similar texture orientations were reported to occur within FCC metals after severe plastic deformation [1], which proves a strong effect of the RS technology on grain refinement, structure restoration and structural units reorientation. The intensities of the fibres were high, however, decreased during swaging passes to 7.5 mm and 5 mm for both the composites, which corresponds to the results of structure observations performed by electron microscopy. Also, the restoration between the individual passes was more notable for composite *I* swaged at room temperature due to significant accumulation of the imposed strain (aggravated continuous restoration due to low processing temperature). By the same reason, the maximum intensities were higher for this composite than for composite *II* swaged at 250 °C.

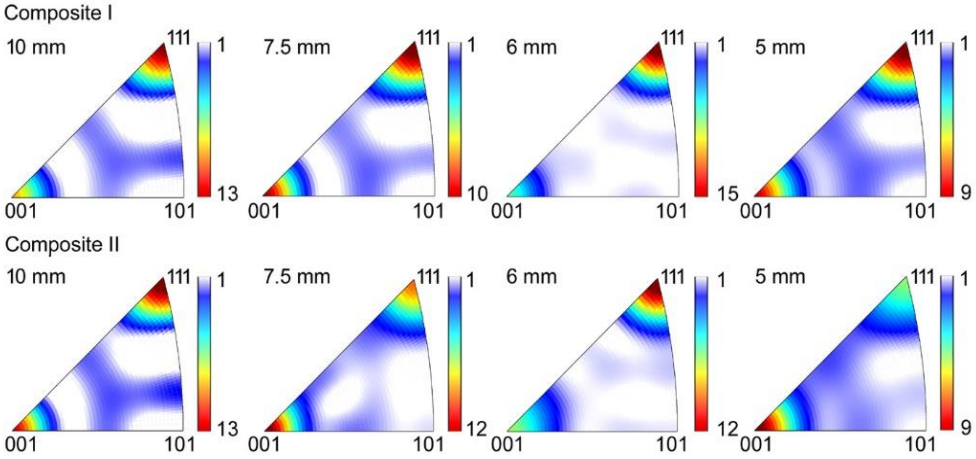

Figure 1. Texture development for both composites

References

[1] V.A. Beloshenko, V.N. Varyukhin, V.Y. Dmitrenko, Y.I. Nepochatykh, V.Z. Spuskanyuk, A.N. Cherkasov, and B.A. Shevchenko, Structure and magnetic properties of Cu-Fe fiber composites obtained using packet hydrostatic extrusion, Technical Physics, Vol. 54, pp. 1790–1794, 2009. doi:10.1134/S1063784209120123.

Structure determination of K2MgSi3O8

Neutron Physics Laboratory - Neutron diffraction

Mathieu ALLIX

Proposal ID

381

Structure determination of K2MgSi3O8

M. Allix, J. Fan, CEMHTI laboratory, Orléans, France
P. Beran, Nucl. Physics Inst., Rez, Czech Republic

$K_2MgSi_3O_8$ is a new crystalline phase which we recently synthesized by full and congruent crystallization from glass. This innovative material is the end member of a large $K_{2-x}Mg_{1-x}Si_{3+x}O_8$ solid solution studied for ionic conductivity properties.

Using laboratory X-ray powder diffraction, we managed to solve the $K_2MgSi_3O_8$ structure. It crystallizes in a hexagonal cell (5.22Å x 8.66A, $P6_3$) with one K site, 2 Mg/Si sites and 2 O sites. ^{29}Si and ^{25}Mg NMR data show that the Mg/Si distribution is not random.

To further describe the structure we used NPD to determine accurately the Mg and Si contents in both tetrahedral sites (unfortunately, Mg^{2+} and Si^{4+}, are isoelectronic so that X-ray diffraction is useless regarding this point). From Rietveld refinements, it appears that Mg and Si are not distributed in the two sites equally. The Si1/Mg1 site is occupied by 90% of Si (10% Mg) whereas the Si2/Mg2 site is occupied by 60% of Si (40% Mg).

Moreover the NPD data refinement enabled to clearly determine the oxygen positions.

We are aiming at publishing these results soon.

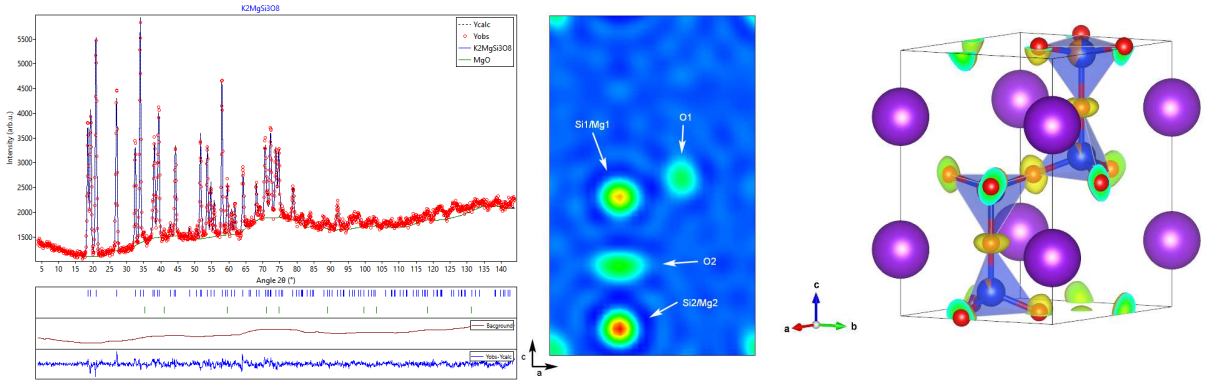

Calibration of SSNTD for light ions

Laboratory of Tandetron

Antonino Cannavó

Proposal ID

382

Report regarding proposal "Calibration of SSNTD for light ions"

A. Cannavò, V. Havránek, J. Vacík

Solid State Nuclear Track Detectors (SSNTD) of the Poly-Allyl-Diglycol Carbonate type (PADC) have been exposed to proton, helium, carbon and copper ion beams provided by the Tandetron 4130 MC accelerator. After the chemical etching of the PADC sheets, consisting in a chemical bath of 2 hours at 70° in a 6.25 N NaOH solution, the etch-tracks have been studied by optical microscopy (OM). A typical OM picture is depicted in Fig.1a showing ion-etch pits as almost dark circles (due to the normal incidence of ions on the PADC surface) on a bright background. In particular such picture has been obtained after the irradiation with 5.8 MeV Cu ions.

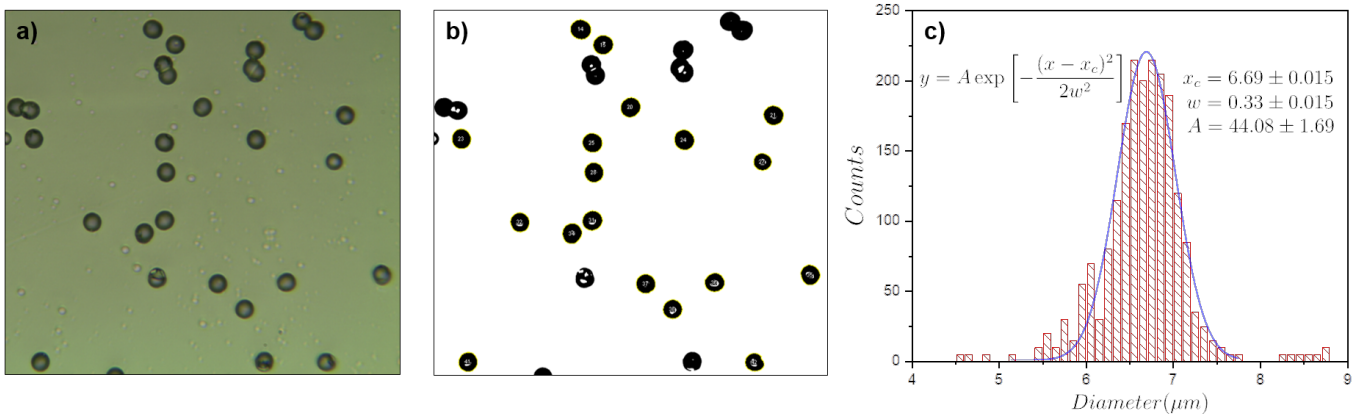

Figure 1: *A typical OM picture obtainable after the chemical etching of a PADC sheet exposed to ion beam a) and its tracks identification b); a typical result of diameter distribution of detected ion-etch pits c).*

OM pictures have been processed through a semi-automatic script developed under ImageJ software. This code identifies and classifies the tracks according to their shape and diameter. An example of its operation is illustrated in Fig.1b where it is shown how the script selects individual tracks (labeled with an increasing number) avoiding the overlapped tracks to be taken into account. The script's output, listing the geometrical characteristics of each detected etch-pits (area, minor and major axis), have been treated with a commercial data analysis software in order to get general information such as the diameter distribution (Fig.1c).

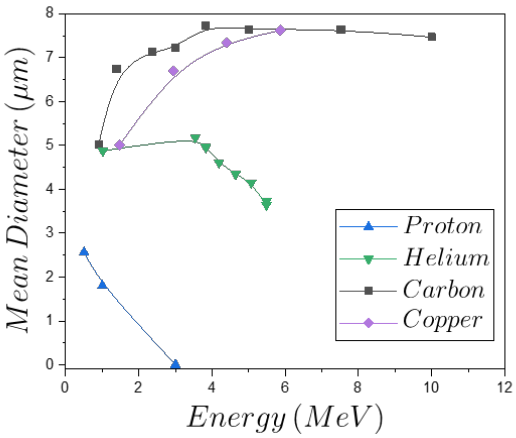

Figure 2: *Dependence of the tracks diameter on the ions energy.*

The results, summarized in the graph of Fig.2, put in evidence a strong correlation between the mean tracks' diameter and the different ions species: the heavier is the irradiating ions the larger is the diameter of the produced tracks, in agreement with previous data reported in literature, e.g., Ref.[1]. Another outcome arising from the Fig.2 is the influence of the ions energy on the tracks development. In the investigated energy ranges, except for the protons, the obtained trends seem not to be a monotonous functions of the ions energy, as also reported in Ref.[2]. This means that two different energies may have the same track diameter. Therefore, with the aim to use such materials for spectroscopic purposes, further analysis of the OM pictures are now being performed to study how the grayness of the ion-etch pits changes as proposed in Ref.[1].

Reference

[1] Malinowska A, Jaskóła M, Korman A, Szydłowski A, Malinowski K, Kuk M. Charged projectile spectrometry using solid-state nuclear track detector of the PM-355 type. Nukleonika. 2015; 60(3):591-6.
[2] El Ghazaly M. On alpha particle spectroscopy based on the over-etched track length in PADC (CR-39 detector). Radiation Effects and Defects in Solids. 2012; 167(6):421-7.

Structural and magnetic transitions in high entropy oxides

Neutron Physics Laboratory - Neutron diffraction

Martin Sahlberg

Proposal ID

383

Introduction

Stabilizing complex compositions in materials containing more than five elements can lead to unexpected improvements of the material properties. Recently, the high-entropy alloys (HEAs) or multi-principal element alloys with more than five elements in equiatomic or near equiatomic ratios have gained considerable attention. Many results indicate that the mechanical properties can be considerably enhanced, but also novel magnetic properties and superconductivity have been reporter, together with significantly lowered thermal conductivity. Recently, the high entropy concept has also been transferred into other material types e.g., oxides, carbides, nitrides etc. Furthermore, the high-entropy effect has also recently been reported for more complex structures such as the Perovskite-type structures, so called HEPs. The magnetic properties, in contrast to the phase formation and average crystallographic structure is not well known to date for such complex oxides. It is therefore of fundamental interest to understand the magnetic behaviour of HEPs, in order to further understand how elements preferably distribute and interacts locally and over longer distances. Here, the magnetic susceptibility, average magnetic structure from low temperature neutron powder diffraction of the HEP comprised of $La_{0.5}Nd_{0.5}(Ti_{1/7}Cr_{1/7}Mn_{1/7}Fe_{1/7}Co_{1/7}Ni_{1/7}Cu_{1/7})O_3$ were investigated.

Experimental details and analysis

Powder samples were synthesized with high temperature synthesis techniques where powered oxides were mixed in stoichiometric amount and subsequently heat-treated. The samples were pre characterized with XRD (Bruker D8) as well as magnetic measurements (MPMS SQUID magnetometer from Quantum Design). Neutron diffraction was performed at the MEREDIT instrument using a copper mosaic monochromator (reflection 220) giving a wavelength of 1.46 Å. Each pattern were collected in a 2θ-range of 4-144° at discrete temperatures ranging from 10 to 973 K. The diffraction patterns were analyzed with the FullProf software [5] utilizing the Rietveld method [6].

Preliminary results

The neutron diffraction experiment reveals that the HEP-sample crystallizes in the orthorhombic perovskite structure with the space group Pnma, figure 1. The unit cell parameters are refined to a = 5.5020(3) Å, b = 7.7466(4) Å and c = 5.4777(3) Å. The *A*-metals (La and Nd) are found at the 4*c* site, the *B*-metals (Ti, Cr, Mn, Fe, Co, Ni and Cu) at the 4*b* site and the oxygen occupies the 4*c* and the 8*d* sites. That the two metal sites are occupied of several metals is clearly shown in figure 1 (b).

The evolution of the magnetic structure were studied upon cooling. The small magnetic moments revealed by magnetometry can be explained by the neutron diffraction power patterns. If the magnetic space group *Pn'm'a*, with the propagation vector k = (0 0 0) is used in the refinements all magnetic intensities in the diffraction pattern can be explained.

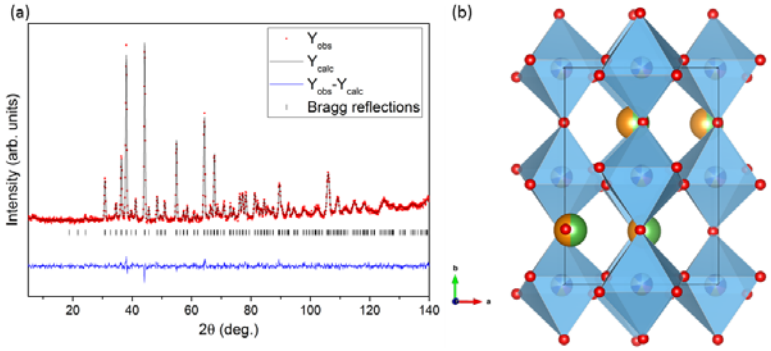

Figure 1. Room temperature diffraction pattern (a) for the HEP-sample and the corresponding structural model (b) wieved along the *c*-direction.

Measure of Li diffusion in amorphous material by NDP technique

Neutron Physics Laboratory - Nuclear analytical methods with neutrons

Giovanni Ceccio

Proposal ID

385

Report regarding proposal “Measure of Li diffusion in amorphous material by NDP technique”

G. Ceccio[a], A. Cannavò[a], P. Horak[a], A. Torrisi[a], I. Tomandl[a], V. Hnatowicz[a], H.S. Tsai[b] and J. Vacik[a]

[a]Nuclear Physics Institute, Academy of Sciences of the Czech Republic, Řež, Czeche Republic;
[b]Institute of Nuclear Engineering and Science, National Tsing Hua University, Taiwan, Republic of China

Diffusion of Li in porous carbon material has been studied using a nondestructive neutron depth profiling technique. It has been acknowledged that carbon-based materials are good candidates for electrodes in lithium-ion batteries. It is because they exhibit a high ability to effectively release Li ions during charging and discharging processes. The Li diffusion was studied in porous carbon material with several annealing cycles. The produced data were useful for the determination of relative straight porosity level and diffusion coefficient, which result to be between 5.13E-11 cm^2/s and 5.56E-11 cm^2/s, that agree with the literature but obtained with a technique that does not alter the sample during the analysis.

The results have been published in Radiation Effects and Defects in Solids, Volume 173, Issue 9-10, Pages 836-841 “Measurement of Li diffusion in porous carbon by neutron depth profiling”

SINE2020 feasibility study - Upgrading UHSS by improving cast microstructure

Neutron Physics Laboratory - Neutron diffraction

Pavel Strunz

Proposal ID

258

1.1. Experimental set-up and data analysis

The neutron diffraction measurements were carried out on the dedicated strain diffractometer SPN-100 installed at the research reactor LVR-15 in Řež. The instrument is equipped with a focusing Si(111) monochromator and a 2D position sensitive detector.

The measurements were done at a fixed position of the 2D detector with the centre of the detector positioned at an angle of 2θ = 65° and an angular range of 12 degrees, the constant neutron wavelength was 0.235 nm, providing a good resolution after diffraction on the α-Fe(110) and / or γ-Fe(111) lattices planes.

A sample gauge volume of 3mm × 3mm × 3mm was defined using fixed cadmium slits in the incident and diffracted neutron beam.

Instrument setup: Sample orientations for measurements:

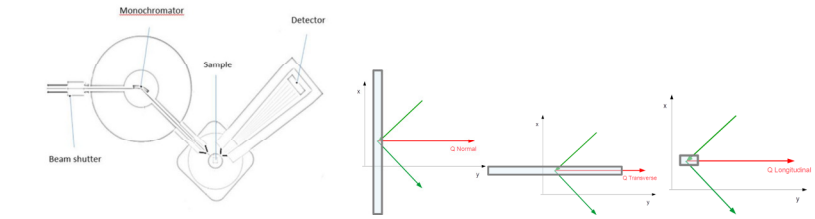

1.1. Data analysis and discussion

Measurements have been performed in the middle of the samples thickness, on a line passing across the marked dendrites line.

Examples of obtained diffraction cones and resulting diffractograms.

Forged sample		As-cast sample	
Normal		Normal	
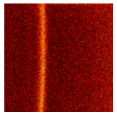	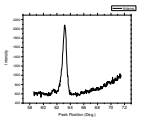	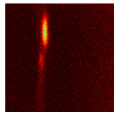	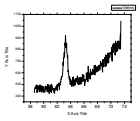
Transverse		Transverse	
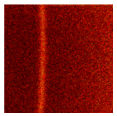	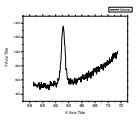	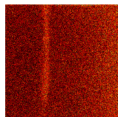	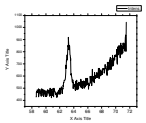
Longitudinal		Longitudinal	
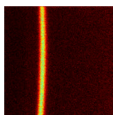	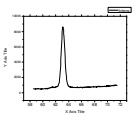	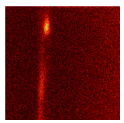	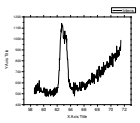

Forged sample:

Data are of good quality and could be analysed.

Since no reference sample for strain free ("d0") value were available (see below comments on the as-cast sample), only relative values based on peak position change can be calculated. With this material, no significant change in peak position, and hence residual strain is observed across the sample.

As-cast sample:

Examples of obtained diffraction cones and resulting diffractograms.

With the as-cast sample, uneven diffraction cone intensity were observed on the 2D positional sensitive detector, complicating the calculation of diffraction pattern (intensity as a function of 2Θ angle) and reliable fitting to the Bragg reflections to extract peak positions.

2. Conclusion & Prospective actions

In conclusion, for the forged sample, no variation in the bragg peak position, and hence residual strain is observed across the sample. For the as-cast sample, unfortunately, no reliable residual strain / stress values could be extracted from the measured data. This is likely due to the large grains and segregation present in the specimens. Alternative analysis methods should be explored.

Study of crystal structure of the UO2/Fe3O4 thin films

Laboratory of Tandetron

Evgenia Chitrova

Proposal ID

386

Report regarding proposal "Study of crystal structure of the UO_2/Fe_3O_4 thin films"

Evgenia Chitrova, Ladislav Havela, Faculty of Mathematics and Physics, Charles University in Prague.

Exchange interaction through interface between a ferrimagnetic (F) magnetite Fe_3O_4 and an antiferromagnetic (AF) UO_2 results in the large magnetic exchange bias (EB) effect [1] (shift of the magnetic hysteresis loop along the field axis) (Fig.1). The magnetism of thin magnetic films and multilayers depends crucially on the structure and interface characteristics. In this work, we studied the crystal structure of Mg-capped UO_2/Fe_3O_4 bilayers (their chemical composition, layers thickness, etc.) deposited on the CaF_2 substrates.

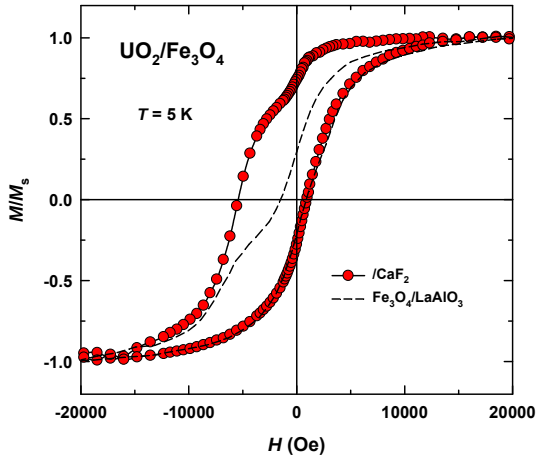

Fig. 1. The *H-M* magnetization loop at 5 K for the UO_2/Fe_3O_4 bilayer after field cooling in the 10 kOe field. The thicknesses for UO_2 and Fe_3O_4 in the bilayer are 280 and 250 Å. Data for a single layer of Fe_3O_4 (270 Å) (broken line) is shown for comparison.

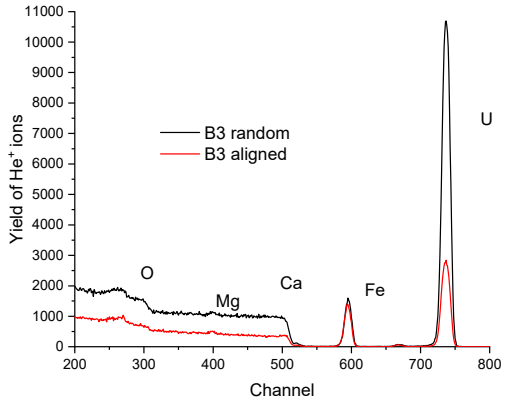

Fig. 2. Yield of back-scattered He ions for the incident beam along the [100] crystallographic direction of the UO_2 crystal (aligned) and at a random orientation (random) for the UO_2/Fe_3O_4 sample deposited on a CaF_2 substrate and capped with Mg.

Rutherford Back-Scattering Spectrometry (RBS) revealed a pronounced ion channelling in UO_2 thus showing low defect concentration in the layer. The spectra obtained showed well-separated signals from UO_2 and magnetite (Fig. 2). Nearly no channelling was observed for the Fe_3O_4 layer. This suggests that the layer is not single-crystalline and/or large concentration of defects/disorder is present in magnetite. The complimentary XRD study on the contrary revealed strong preferential orientation of Fe_3O_4 in the [111] out-of-plane direction and a presence of twins (similar to the results of Ref. 2). Presence of an impurity was found in the spectrum (does not exhibit channeling effect), which was attributed to some contamination of the Fe target by Zr. Since Zr is non-magnetic it should not influence the magnetic properties of magnetite. Thickness of magnetite found from RBS is close to that from the XRD study.

1) W. H. Meiklejohn and C. P. Bean, "New magnetic anisotropy", Phys. Rev. B, 102 1413, (1956).
2) E. A. Tereshina et al, Appl. Phys. Lett., 105 122405 (2014).

The role of water in the formation of the crystal structure of bacterial cellulose (BC)

Neutron Physics Laboratory - Neutron diffraction

Ruslan Smyslov

Proposal ID

387

Report regarding proposal “The role of water in the formation of the crystal structure of bacterial cellulose (BC)”

Ruslan Smyslov, Institute of Macromolecular Compounds of RAS, Saint Petersburg, Russia,
Aleksei Sokolov, Gennady Kopitsa, Anna Kulminskaya, Petersburg Nuclear Physics Institute named by B.P. Konstantinov of National Research Centre «Kurchatov Institute»,
Natalia Tsvigun, FSRC “Crystallography and Photonics” of RAS

Using the diffractometer MEREDIT, one registered a neutron diffraction pattern for deuterated bacterial cellulose (**dBC**). Nano-gel-film of bacterial cellulose (**BC**) was preliminary synthesized using *Komagataeibacter xylinus* strain in Research Center KI 'PNPI'. The specimens of the BC are obtained by the synthesis in the heavy water-based medium directly. The chemical gross formula of BC is $C_{12}H_{14}D_6O_{10}$.

The project is aimed to determine the availability for deuteration of hydroxyl groups in the crystalline lattice of BC during biosynthesis and self-assembly of supramolecular structure.

The Rietveld refinement was carried out using MAUD software [1] on the basis of the crystalline cell of cellulose Iα according the CIF data file 4114382 [2] from Crystallography Open Database [3]. In Figure 1, d-spacing is shown for a ND pattern of the dBC under investigation. Cellulose Iα has the triclinic crystal system with space group P1.

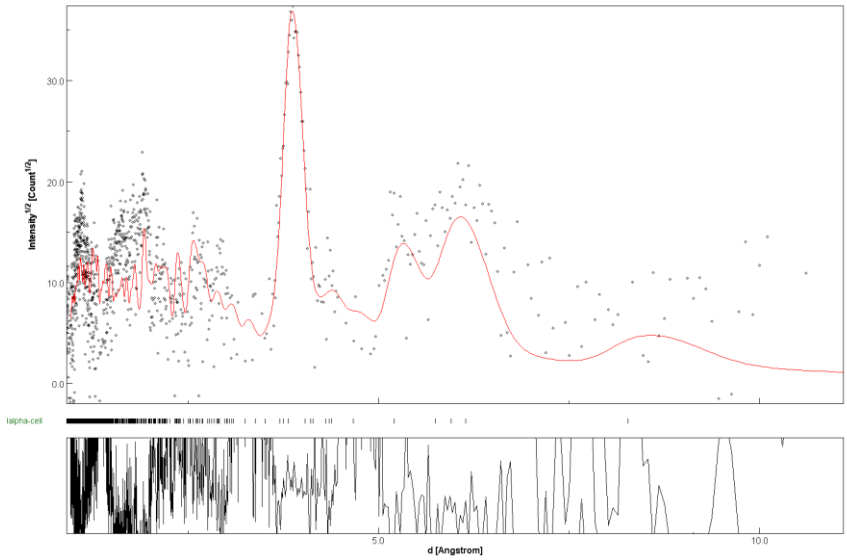

Figure 1. Neutron diffraction pattern for deuterated bacterial cellulose

Table 1. Comparison of Experimental Details

Data Collection		
diffractometer	MEREDIT	D19 [2]
Crystal Data		
chemical formula	$C_{12}H_{14}D_6O_{10}$	
cell setting, space group	triclinic, P1	triclinic, P1
a (Å)	10,270	10,400(6)
b (Å)	6,581	6,717(7)
c (Å)	5,925	5,962(6)
α (°)	81,052	80,37(5)
β (°)	118,39	118,08(5)
γ (°)	115,07	114,80(5)
V (Å^3)	318,6	333,3(6)
radiation type	neutron	neutron
λ (Å)	1,4600	1,3058

The preliminary comparing of the data obtained using the MEREDIT instruments and the D19 diffractometer [2] shows the concordance between them (Table 1). However, the cell for bacterial cellulose occurs less than for cellulose from the cell wall of the freshwater alga *Glaucocystis nostochinearum*.

References

[1] L. Lutterotti, Total pattern fitting for the combined size-strain-stress-texture determination in thin film diffraction, Nuclear Inst. and Methods in Physics Research, B, 268, 334-340, 2010.
[2] Nishiyama Y. at al. J. AM. CHEM. SOC. 2003, 125, 14300-14306 – DOI: 10.1021/ja037055w
[3] http://www.crystallography.net/cod/

RBS characterisation of ScN thin films compositions

Laboratory of Tandetron

Jan Lancok

Proposal ID

389

Joris More Chevaliet, RNDr. Anna Macková, Ph.D. **at all.**
Institute of Physics AV CR, Na Slovance 2, 182 21 Prague 8, Czech Republic, Nuclear Physics Institute of the ASCR, v. v. i., Rez 130, 250 68, Rez near Prague, Czech Republic

ScN/MgO

The ScN layers were deposited on double-side polished MgO (001) substrate in an ultra-high-vacuum (UHV) system (10-8 Pa) by DC reactive magnetron sputtering using a 99.9999% pure N2 discharge. The sample holder was electrically heated to reach the temperature of 700 °C. The working pressure of 3.5 Pa was used to sputter ScN from 99.9% pure Sc target of one inch diameter with a detectable contaminant of Ta at 0.1%. The thickness was measured using a Profilometer and confirmed by spectroscopic ellipsometry.

Experimental details

The measurements were performed by using the ion beam provided by the tandem accelerator, Tandetron MC 4130, at the Nuclear Physics Institute in Rez near Prague. A typical RBS spectrum you can see in Figure 2.

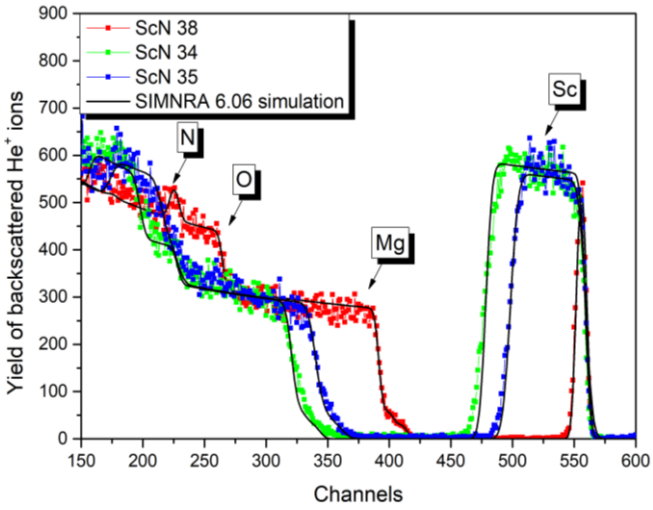

Figure 2: The RBS-C measurement of ScN/MgO measured by energy 2.0 MeV using He^+ ions.

Results

In Table 1 you can see in the second column name of the sample, third – thickness *t* from elipsomentry (in nm unit). In columns 4 and 5, there are *t* of each samples from RBS mentioned in 1e15at./cm^2 unit and nm (calculated at density 4.28(2) g/cm^3). In columns 6-10, there are concetrations of Sc, N, C Mg and O (mentioned in atomic percent) determined using the RBS method.

Table 1: Samples concentration

n.	sample	*t* (elipsometry) [nm]	*t* (RBS) [1e15at./cm^2]	*t* (RBS) [nm]	Sc [at.%]	N [at.%]	C [at.%]	Mg [at.%]	O [at.%]
1.	ScN 38	32	230	24	42.0	52.0	6.0	50	50
2.	ScN 34 700°C	248	2100	217	41.0	53.5	5.5	50	50
3.	ScN 35 700°C	190	1620	169	39.5	57.0	3.5	50	50

The received data will be used for publication concerning ScN thin films and compare with those obtained from EDX, XPS and XRF

Preferential site occupation in high entropy alloys FeCrAlV

Neutron Physics Laboratory - Neutron diffraction

Stanislav Daniš

Proposal ID

390

Report ragrding proposal “Preferential site occupation in high entropy alloys FeCrAlV”

S. Daniš and J. Pešička, Charles University Prague, Czech Republic
P. Beran, Nucl. Phys Inst, Řež, Czech Republic

The aim of proposal was to determine if the atoms within HEA FeCrAlV occupies preferably some atomic positions. The situation was unclear from x-ray diffraction pattern because of low diffraction contrast of elements within the alloy. Neutron diffraction suffers from the same properties of Fe, Al, Cr and V, but we have planned to combine x-ray and neutron diffraction patterns in order to reveal the supposed preferential occupation.

Fortunately, from the neutron experiment which gives us much more clear data, we can conclude that the position within the crystal structure are not occupied uniformly. The structure of FeCrAlV alloy is based on structure of Fe_3Al alloy. This alloy crystallizes within fcc lattice, space group Fm3m (225). Iron atoms lie in *4b* and *8c* position, atoms of Al in position *4a* (Wyckoff notation).

Because Rietveld method in Fullprof Suite Package [1] is able to bind together only occupation of two atoms on the same position, we had to test the all possible combination of atomic positions. Simulation are still ongoing but the first results revealed that Fe predominantly occupies position *8c*, Al prefers position *4b*. Chromium and vanadium lie mainly in positions *4a* and *8c*. One of the best results are depicted at Figure 1.

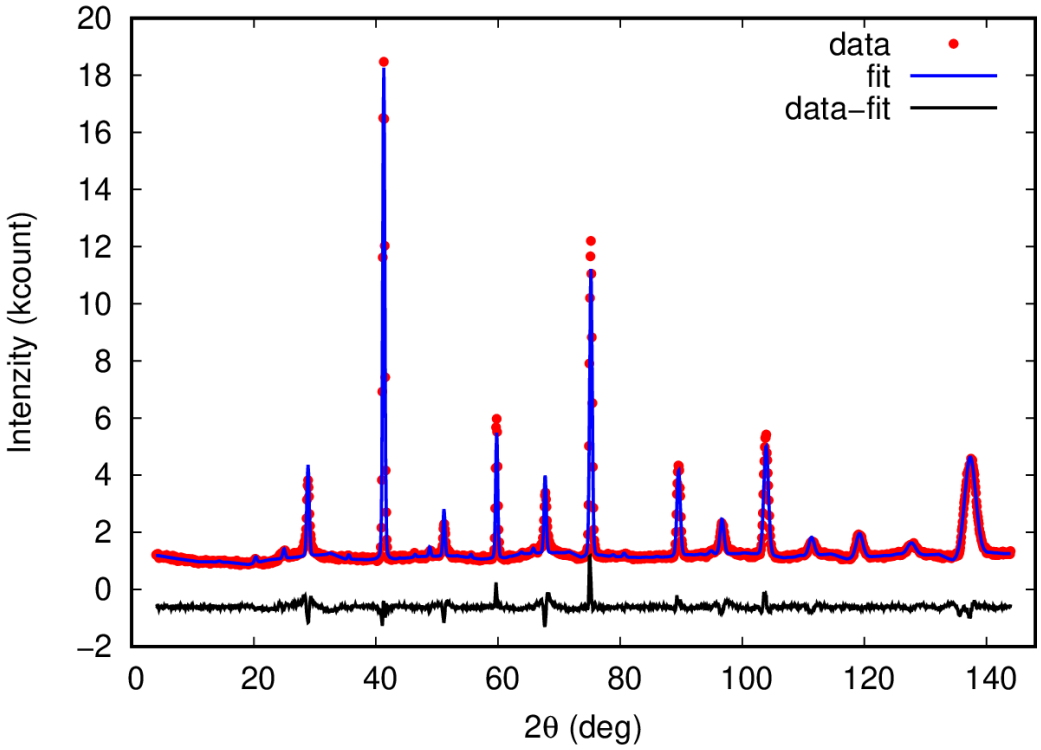

Figure 1: Result of Rietveld fitting procedure of neutron diffraction data of annealed FeCrAlV alloy.

[1] Rodriguez-Carvajal, J., Physica B.(1993), 192, 55

Boron doping in diamond

Neutron Physics Laboratory - Nuclear analytical methods with neutrons

Alexander Kromka

Proposal ID

392

Boron doping in diamond - fabrication of structured BDD electrodes for electrochemical applications

Pavla Štenclová, Tibor Ižák, Ondrej Szabó, Štěpán Potocký and Alexander Kromka

Institute of Physics, Czech Academy of Sciences, Cukrovarnická 10, 162 00 Prague 6, Czech Republic

In this study, we fabricated structured BDD electrodes for a separate as well as simultaneous detection of Cd^{2+} and Pb^{2+}. The BDD films (initially 2 µm thick) were grown in HFCVD on Si substrates by addition of boron (10000 ppm) to the H_2/CH_4 gas mixture (Figure 1a). Various structures (Figure 1b-d) were obtained by O_2 reactive ion etching (RIE) with or without gold nano-particle mask. The gold mask was created by evaporation of Au thin film (3 nm for the small mask, 12 nm for the large mask, resp.) and subsequent annealing in hydrogen MW plasma at 500 °C for 10 minutes. Residual gold after O_2 RIE was removed by wet chemical treatment (aqua regia).

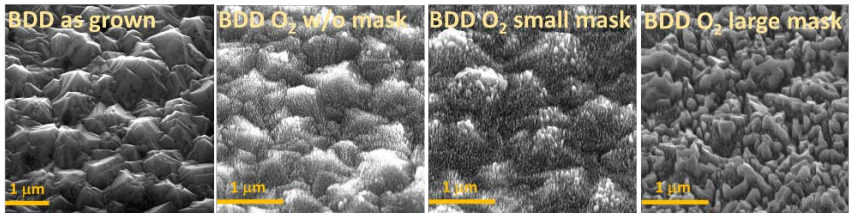

Figure 1. Representative 45° tilted angle-view SEM images of selected samples: a) as-grown BDD, b) etched without a mask and etched with c) small and d) large gold masks.

Table 1: The concentration of chemical bonds from the deconvoluted C 1s peak (XPS analysis)

Sample name	sp^2,%	sp^3,%	CH_x, %	C-O-C, %	C=O,%
BDD as grown	3	55	30	9	3
BDD w/o mask	31	49	8	8	3
BDD small mask	31	50	7	9	3
BDD large mask	33	44	10	10	3

RIE w/o or through small mask gave dense tiny nanograss on original diamond crystals, while etching through large mask resulted in irregular nano/microstructure. XPS analysis has shown, that the fabrication process significantly increased sp^2 phase RIE structured electrodes, while the oxygen content remained constant (Table 1). Neutron depth profiling (NPD) pointed out the boron atoms are evenly distributed within 1 µm depth of the electrodes. The concentrations of B atoms are given in Table 2.

Table 2: The concentration boron content (NDP).

Sample name	^{10}B content (10^{15} atoms·cm^{-2})
BDD as grown	70
BDD w/o mask	36
BDD small mask	80
BDD large mask	95

We have found that structured BDD electrodes showed a wider potential window compared to flat BDD electrodes. BDD as grown gave the best results for separate detection of Cd^{2+} or Pb^{2+}. The lowest relative standard deviation for simultaneous detection of Cd^{2+} and Pb^{2+} was found for BDD electrode etched through small Au mask. It seems, that the obtained results are independent of boron content obtained by NPD. On the other hand, electrode performance could be influenced by the relevant content of the sp^2 phase.

Damage formation and optical activation of dopants in ZnO

Laboratory of Tandetron

Romana Mikšová

Proposal ID

393

Report regarding proposal "Damage formation and optical activation of dopants in ZnO."

A.Macková, P.Malinský, A.Jagerová, R.Mikšová, Nuclear Physics Institute of the Czech Academy of Sciences, v. v. i., Rez, Czech Republic
P.Nekvindová, J.Cajzl, Department of Inorganic Chemistry, Institute of Chemical Technology, Prague, Czech Republic
R. Böttger, S. Akhmadaliev, Institute of Ion Beam Physics and Materials Research, Helmholtz Zentrum Dresden-Rossendorf, Dresden, Germany

In our results, the structural modification of ZnO in c-plane (0001), a-plane (11–20) and m-plane (10-10) ZnO – implanted with Au^+ ions using the energy of 400 keV and fluences of 5×10^{14} and 1×10^{15} cm^{-2} and subsequently annealed at 600°C in O_2 was investigated. Deep structural damage grew with increased Au-ion fluence and Au did not exhibit strong out-diffusion from the depth to the surface during the post-implantation annealing. RBS measurements during ion implantation revealed more progressive deep-damage formation in the c- and m-planes than in the a-plane ZnO. Simultaneously, the smallest Zn sub-lattice disorder deduced from RBS/C measurements was observed in the a-plane ZnO. During post-implantation annealing, a slight structure recovery (about 4%) was observed in all orientations.

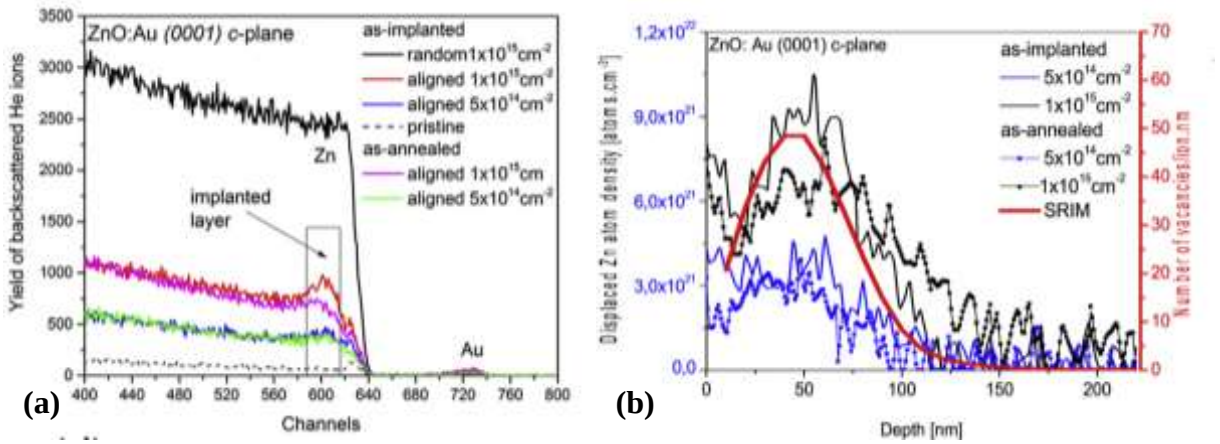

Figure 1. The RBS/channelling spectra for as-implanted and as-annealed samples: (a) c-plane ZnO. The region of interest appropriate to the ion-implanted layer is indicated in the black rectangle. The density profiles of the displaced Zn atom for various ion-implantation fluences determined from RBS/C spectra for as-implanted and as-annealed samples for the c-plane (b). SRIM-predicted Zn vacancy depth-distribution profiles are shown.

Raman spectroscopy confirmed the increasing structure disorder with the enhanced ion fluence for all as-implanted ZnO orientations and a partial reconstruction of the ZnO structure during annealing when the intensity of E_2 phonons was increased and that of longitudinal optical (LO) phonons was suppressed because of the disorder recovery. E_2(high) and E_1(LO) Raman phonon modes show a significant modification mainly in the m-plane.

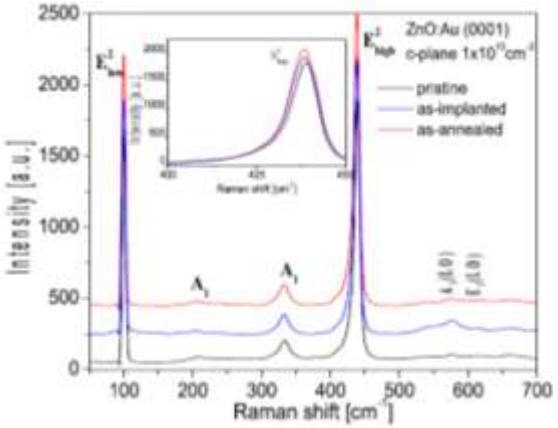

Figure 2. The Raman spectra of as-implanted (blue curves) and as-annealed (red curves) samples implanted using the ion-implantation fluence of 1×10^{15} cm−2 for c-plane ZnO.

All results from experiments on ZnO were published in Vacuum, Nuclear Instruments and Methods in Physics Research B and Journal of Alloys and Compounds.